

THE OUTER DISKS OF NEARBY GALAXIES

by

Stéphane Herbert-Fort

A Dissertation Submitted to the Faculty of the
DEPARTMENT OF ASTRONOMY
In Partial Fulfillment of the Requirements
For the Degree of
DOCTOR OF PHILOSOPHY
In the Graduate College
THE UNIVERSITY OF ARIZONA

2011

THE UNIVERSITY OF ARIZONA
GRADUATE COLLEGE

As members of the Dissertation Committee, we certify that we have read the dissertation prepared by Stéphane Herbert-Fort entitled The Outer Disks of Nearby Galaxies and recommend that it be accepted as fulfilling the dissertation requirement for the Degree of Doctor of Philosophy.

_____ Date: 19 July 2011
Dennis Zaritsky

_____ Date: 19 July 2011
Christopher Walker

_____ Date: 19 July 2011
Marcia Rieke

_____ Date: 19 July 2011
Romeel Davé

_____ Date: 19 July 2011
Desika Narayanan

Final approval and acceptance of this dissertation is contingent upon the candidate's submission of the final copies of the dissertation to the Graduate College.

I hereby certify that I have read this dissertation prepared under my direction and recommend that it be accepted as fulfilling the dissertation requirement.

_____ Date: 19 July 2011
Dissertation Director: Dennis Zaritsky

STATEMENT BY AUTHOR

This dissertation has been submitted in partial fulfillment of requirements for an advanced degree at The University of Arizona and is deposited in the University Library to be made available to borrowers under rules of the Library.

Brief quotations from this dissertation are allowable without special permission, provided that accurate acknowledgment of source is made. Requests for permission for extended quotation from or reproduction of this manuscript in whole or in part may be granted by the head of the major department or the Dean of the Graduate College when in his or her judgment the proposed use of the material is in the interests of scholarship. In all other instances, however, permission must be obtained from the author.

SIGNED: Stéphane Herbert-Fort

ACKNOWLEDGMENTS

I want to highlight a few people who have played significant roles in helping me get to a PhD: my parents Christopher Herbert and Bernadette Fort, my sister Sophie Herbert-Fort, my wife Stephanie Cortes, my undergraduate advisor Jason X. Prochaska, and my graduate advisor Dennis Zaritsky. You have all provided an incredible amount of encouragement and support over the years. I would not have made it this far without you. Thank you!!

Many thanks also go to the friends I made in college and in graduate school. I feel lucky to have landed in such smart, fun groups of people. Thanks for making the past decade+ (!) so enjoyable. I have come to love living in Tucson, in great part because of all the good times I had with many of you here. Thanks for everything.

Of course, there remain many, many others to thank, from telescope operators to institutions and international organizations, but I will cut myself off here. If you have played any part in my life as an astronomer, thank you.

DEDICATION

For my family, especially my parents, for always pushing me to succeed in school.

TABLE OF CONTENTS

LIST OF FIGURES	8
LIST OF TABLES	10
ABSTRACT	11
CHAPTER 1 INTRODUCTION	13
CHAPTER 2 SPATIALLY CORRELATED CLUSTER POPULATIONS IN THE OUTER DISK OF NGC 3184	17
2.1 Chapter Abstract	17
2.2 Chapter Introduction	17
2.3 Observations to Final Source Catalog	21
2.3.1 Observations	21
2.3.2 Data Reduction	21
2.3.3 Mosaic Creation	23
2.3.4 Source Detection	24
2.3.5 Photometry & Final Source Catalog	25
2.4 Cluster Populations Surrounding NGC 3184	27
2.5 Clustering of knots in the outer disk	32
2.6 A comparison to GALEX UV source extent	42
2.7 A comparison to the underlying neutral gas profile	42
2.8 The local environment of NGC 3184	48
2.9 Summary and Discussion	50
CHAPTER 3 STAR CLUSTER POPULATIONS IN THE OUTER DISKS OF NEARBY GALAXIES	54
3.1 Chapter Abstract	54
3.2 Chapter Introduction	55
3.3 Observations to Final Source Catalog	57
3.4 Cluster Populations Surrounding the Galaxies	62
3.5 Clustering of Knots in the Outer Disks	77
3.5.1 Self-clustering of LBT Knots	77
3.5.2 Self-clustering of GALEX Knots	88
3.5.3 Cross-correlation of LBT Knots and Neutral Gas Disks	94
3.5.4 Discussion of Correlation Results from All Datasets	103
3.6 Summary and Conclusions	107

TABLE OF CONTENTS — *Continued*

CHAPTER 4	THE SURFACE MASS DENSITY AND STRUCTURE OF THE OUTER	
	DISK OF NGC 628	111
4.1	Chapter Abstract	111
4.2	Chapter Introduction	111
4.3	Sample Selection, Observations, and Data Reduction	115
4.4	Analysis, Results & Discussion	116
4.4.1	H α detections	116
4.4.2	H α knot velocities in the disk frame and σ_z	117
4.4.3	Outer disk scale height h_z	124
4.4.4	Outer disk mass density	126
4.4.5	Star formation history constraints	128
4.4.6	Similarities between the young and old components	129
4.5	Summary and Conclusions	129
CHAPTER 5	A SEARCH FOR MOLECULAR EMISSION FROM OUTER DISK STAR-	
	FORMING COMPLEXES IN NGC 628	132
5.1	Chapter Introduction	132
5.2	SMT Observations, Data Reduction & Analysis	134
5.3	Results & Discussion	135
5.4	Conclusions	141
CHAPTER 6	CONCLUSIONS AND WAYS FORWARD	143
REFERENCES	146

LIST OF FIGURES

2.1	A portion of our deep V -band mosaic.	26
2.2	CMD of sources between $1.0 - 1.5R_{25}$ from our final catalog.	29
2.3	Background-subtracted Hess diagram showing the number of sources remaining in the outer disk.	30
2.4	The radii defined for creating the restricted three-point correlation maps.	34
2.5	Restricted three-point correlation maps from sources in our final catalog.	37
2.6	Average correlation signal from areas $r_{out} \leq 0.5$ kpc in restricted three-point correlation maps.	40
2.7	Restricted three-point correlation maps from publicly-available GALEX AIS sources.	43
2.8	The central portion of our deep LBT/LBC V -band mosaic with the 3σ $N(\text{HI})$ threshold in black contour.	45
2.9	Histograms showing the number of H I pixels per kpc^2 in circular annuli.	46
2.10	Restricted three-point cross-correlation maps of LBT-detected knots and H I pixels.	49
3.1	Comparison of GALEX and LBT imaging of a region around NGC 4736.	56
3.2	CMD of all sources (including background sources) between $1.0 - 1.5R_{25}$ from our final catalog of IC 4182.	65
3.3	Same as Figure 3.2 but for NGC 3351.	66
3.4	Same as Figure 3.2 but for NGC 4736.	66
3.5	Same as Figure 3.2 but for NGC 4826.	67
3.6	Same as Figure 3.2 but for NGC 5474.	68
3.7	Same as Figure 3.2 but for NGC 6503.	68
3.8	Background-subtracted Hess diagrams for IC 4182, made from sources between $1.0 - 1.5 R_{25}$, $1.5 - 2.0 R_{25}$, and $2.0 - 2.5 R_{25}$	70
3.9	Same as Figure 3.8 but for NGC 3351.	70
3.10	Same as Figure 3.8 but for NGC 4736.	71
3.11	Same as Figure 3.8 but for NGC 4826.	71
3.12	Same as Figure 3.8 but for NGC 5474.	72
3.13	Same as Figure 3.8 but for NGC 6503.	72
3.14	The average Hess diagram from all galaxies, with sources combined as a function of M_V , including and excluding NGC 4736, made from sources between $1.0 - 1.5 R_{25}$, $1.5 - 2.0 R_{25}$, and $2.0 - 2.5 R_{25}$	74

LIST OF FIGURES — *Continued*

3.15	Simulated Hess diagrams made from a Starburst99 $10^3 M_\odot$ cluster track and the CMD uncertainties from NGC 4736, for different cluster formation rates.	75
3.16	The radii defined for creating the restricted three-point correlation maps.	78
3.17	Restricted three-point correlation maps from sources in our (masked) final catalog of IC 4182.	79
3.18	Same as Figure 3.17 but for NGC 3351.	80
3.19	Same as Figure 3.17 but for NGC 4736.	81
3.20	Same as Figure 3.17 but for NGC 5474.	82
3.21	Probability (as a function of radius) that peaks in the three-point correlation map of IC 4182 (Figure 3.17) are caused by random excursions.	84
3.22	Same as Figure 3.21 but for NGC 3351.	85
3.23	Same as Figure 3.21 but for NGC 4736.	86
3.24	Same as Figure 3.21 but for NGC 5474.	87
3.25	Restricted three-point correlation map similar to Figure 3.17 but here using 171 GALEX sources around IC 4182.	89
3.26	Same as Figure 3.25 but from 179 GALEX sources around NGC 3351.	90
3.27	Same as Figure 3.25 but from 398 GALEX sources around NGC 4736.	90
3.28	Same as Figure 3.25 but from 174 GALEX sources around NGC 5474.	91
3.29	Restricted three-point cross-correlation maps of LBT-detected knots around IC 4182 and H I pixels with $N(\text{HI})$ above the noise level of the integrated H I map.	96
3.30	Same as Figure 3.29 but for NGC 3351.	97
3.31	Same as Figure 3.29 but for NGC 4736.	98
3.32	Same as Figure 3.29 but only for blue sources around IC 4182 and for different $N(\text{HI})$ pixel cuts.	100
3.33	Same as Figure 3.32 but for NGC 3351.	101
3.34	Same as Figure 3.32 but for NGC 4736.	102
4.1	Three of our final 1D spectra, illustrating the range of strength of the $\text{H}\alpha$ detections.	118
4.2	The locations of our 15 $\text{H}\alpha$ detections on the velocity field of the H I disk.	119
4.3	Distribution of $\text{H}\alpha$ knot vertical velocities.	123
5.1	SMT pointings and final spectra.	136

LIST OF TABLES

3.1 Sample Galaxies 59

3.2 Sources in CMDs 63

3.3 Sources in LBT-matched GALEX catalogs 93

4.1 H α detections 120

ABSTRACT

This dissertation presents three observational projects designed to characterize the outer disks of nearby galaxies (beyond the optical radius R_{25}). Until very recently, outer disks remained an elusive and poorly-understood component of disk galaxies.

We first present a Large Binocular Telescope (LBT) optical imaging survey of nearby outer disks to examine the basic properties of this component. Our LBT observations indicate that most nearby galaxies host an outer disk with star formation occurring at a very low level. We detect hundreds of outer disk star clusters and show that they typically have masses $\sim 10^2 - 10^4 M_\odot$ and ages up to a Gyr. The clusters are born in groups that can remain clustered for a Gyr or more, while the clusters slowly evaporate stars into a diffuse stellar component. The clusters appear to form from localized overdensities in the gas distribution primarily associated with spiral structure. The clusters extend to $2R_{25}$ in our sample. We find that some clusters may also reside well outside of their host galaxy's gas disk.

Our second project is a kinematic study of $H\alpha$ knots in the outer disk of the large, isolated, face-on galaxy NGC 628, using Inamori Magellan Areal Camera and Spectrograph (IMACS) observations from the Magellan telescope. This galaxy shows a kinematically cold outer disk (velocity dispersion $< 11 \text{ km s}^{-1}$) with a mass density $\Sigma = 7.5 M_\odot \text{ pc}^{-2}$. Our observations cannot exclude uniform star formation lasting a Hubble time in this outer disk and confirm that this component is an extension of the kinematically-cold inner disk.

Our third project is a search for molecular emission in the outer disk of NGC 628, using the sensitive Atacama Large Millimeter Array (ALMA) receiver on the

Submillimeter Telescope (SMT). We did not detect emission from our outer disk pointings, though we are able to provide useful estimates for future ALMA observations of outer disk knots. Our SMT observations indicate that the H_2 / H I ratio is $\sim 100\times$ lower in the outer disk than in the inner disk, which likely explains, at least in part, the trend towards smaller clusters and lower star formation rates at larger radii.

CHAPTER 1

INTRODUCTION

We have known for decades that the gas disks of most large, late-type galaxies extend far beyond the optical radii of their disks (van der Kruit & Allen , 1976). Because the stellar disks appear to have such well-defined extents, beyond which no stars are obvious in typical galaxy images, it was assumed that the outer gas disks simply did not host star formation. It was then shown that nearby outer disks should globally lie below the gas density threshold for star formation (Kennicutt , 1989), so it was not surprising that they appeared devoid of stars. Without many exciting phenomena to observe in outer disks, the field lost interest and very little study of these extreme regions was pursued.

The field got a jolt of excitement when Ferguson et al. (1998) used deep $H\alpha$ imaging to discover star formation in an extended component around three nearby galaxies. Perhaps the outer disks were not as dead as everyone assumed. The stellar complexes Ferguson et al. (1998) identified beyond the optical radii appear to trace the spiral structure in the gas, indicating that there could be small, local regions in the outer disk where the gas density was in fact high enough to form stars. Modern simulations (e.g. Bush et al. , 2008) have shown that this is indeed the case. Unfortunately, at the time it was difficult to find many other examples of outer disk star formation, both with narrowband $H\alpha$ imaging and (especially) with broadband optical imaging. Without sizable samples of outer disk star formation for statistical studies, it was difficult to characterize the nature of this elusive population. So again, the study of outer disks fell out of favor and galaxy research was focused elsewhere.

In April 2003 NASA launched the GALEX satellite (Martin et al. , 2005), a

sensitive ultraviolet observatory. With GALEX came a tremendous resurgence of interest in the observational study of outer disks (Gil de Paz et al. , 2005, 2007; Thilker et al. , 2005, 2007; Zaritsky & Christlein , 2007). This is because GALEX began producing images of nearby galaxies that clearly showed star formation occurring in large numbers of outer disks. The reason GALEX was such a powerful probe of outer disk star formation lies in the color contrast it can achieve between blue disk sources and the predominantly redder background of galaxies, in the ultraviolet. Both the sensitivity and resolution of GALEX finally made it possible to observe large numbers of outer disk ‘knots’, providing the fuel for an exciting new field of research. The GALEX observations proved that there was much more to outer disks than had been previously thought, and that many different questions, some very basic, were now up for study. What are these stellar populations like, forming in such an extreme environment? Do the knots always trace the gas? How old are they, and how long have they been forming? Does star formation occur differently than in the inner disk, where gas densities and metallicities are much higher? What percentage of disks have stellar populations beyond their optical radii? Do the knots provide signatures of disk formation and hierarchical accretion, given the long dynamical times at these radii? How much dark matter is in the disk at large radii, and how does it compare to the baryonic mass? How is the baryonic mass even arranged?

With the revival of observational interest in outer disks also came significant attention from the theoretical community (e.g. Bush et al. , 2008; Roškar et al. , 2008a,b; Kazantzidis et al. , 2009). Much progress has been made in understanding the environments in which the knots form, as well as how they might evolve over time. It appears that the UV-bright knots are often large complexes of star clusters, and that over time these clusters can populate the disk with a smooth

component of stars, via dissolution and radial migration. Much is being learned on the theoretical front, in large part because there is now much more observational data on outer disks being used to constrain the theories.

We began this project around the time GALEX was used to show that $\sim 30\%$ of nearby disk galaxies host star formation in an extended component (Zaritsky & Christlein, 2007). We wanted to expand on the GALEX observations at longer wavelengths, once we knew there was in fact a large population of clusters to look for. We wanted to push down the mass limit and push out the age limit of the GALEX observations, in order to discover more knots and be able to study individual outer disks with a statistical approach. We wanted to better characterize the outer disk stellar populations, determine their ages, how long they have been forming, from what they formed, how far they extend, how they cluster, and what their kinematics are like.

These questions drove us to take on a number of projects, described in detail in this dissertation. Chapters 2 and 3 cover our Large Binocular Telescope (LBT) optical imaging studies of a sample of nearby galaxies, the first chapter being a pilot study focusing on one galaxy, NGC 3184, and the second covering the other six galaxies observed. This dissertation is among the first to include published data from the LBT; our observations began during the Science Demonstration Time of the Large Binocular Cameras (LBC) in early 2007. Chapter 4 presents a kinematic study of the outer disk of NGC 628, using Inamori Magellan Areal Camera and Spectrograph (IMACS) observations from the Magellan telescope, where we have used $H\alpha$ knots to trace the underlying structure and total mass of this outer disk. Chapter 5 presents a search for molecular gas in the outer disk of NGC 628 using the sensitive Atacama Large Millimeter Array (ALMA) receiver on the Submillimeter Telescope (SMT), to improve constraints on the integrations

required to detect molecular emission from outer disk complexes in the future. Together, these projects provide a deeper understanding of this long-overlooked component of disk galaxies. Our research helps lay the groundwork for a full characterization of outer disks, and raises a number of interesting questions for future research.

CHAPTER 2

SPATIALLY CORRELATED CLUSTER POPULATIONS IN THE OUTER DISK OF NGC

3184

2.1 Chapter Abstract

We use deep (~ 27.5 mag V -band point-source limiting magnitude) V - and U -band LBT imaging to study the outer disk (beyond the optical radius R_{25}) of the non-interacting, face-on spiral galaxy NGC 3184 ($D = 11.1$ Mpc; $R_{25} = 11.1$ kpc) and find that this outer disk contains > 1000 objects (or marginally-resolved ‘knots’) resembling star clusters with masses $\sim 10^2 - 10^4 M_{\odot}$ and ages up to ~ 1 Gyr. We find statistically significant numbers of these cluster-like knots extending to $\sim 1.4R_{25}$, with the redder knots outnumbering bluer at the largest radii. We measure clustering among knots and find significant correlation to galactocentric radii of $1.5R_{25}$ for knot separations < 1 kpc. The effective integrated surface brightness of this outer disk cluster population ranges from $30 - 32$ mag arcsec $^{-2}$ in V . We compare the H I extent to that of the correlated knots and find that the clusters extend at least to the damped Lyman- α threshold of H I column density (2×10^{20} cm $^{-2}$; $\sim 1.62R_{25}$). The blue knots are correlated with H I spiral structure to $\sim 1.5R_{25}$, while the red knots may be correlated with the outer fringes of the H I disk to $\sim 1.7R_{25}$. These results suggest that outer disks are well-populated, common, and long-lasting features of many nearby disk galaxies.

2.2 Chapter Introduction

Ultraviolet observations with the Galaxy Evolution Explorer (GALEX; Martin et al. , 2005) indicate that $\sim 30\%$ of nearby disk galaxies host star formation in an extended component (Thilker et al. , 2007; Zaritsky & Christlein , 2007). These

stellar disks sometimes reach to more than twice the optical radius (R_{25}) and challenge our understanding of disk galaxies. Motivated by a lack of understanding and because progress here may pose additional challenges for galaxy formation models, we begin a systematic investigation of a sample of seven nearby galaxy outer disks using deep optical imaging and present first results here.

Although deep $H\alpha$ and broadband optical observations (e.g. Ferguson et al. , 1998; Martin & Kennicutt , 2001; Weiner et al. , 2001) had previously detected star formation in outer disks, the ubiquity, and therefore the significance, of this component has been largely overlooked until recently. The traditional tracer of very young star clusters and ongoing star formation, $H\alpha$ flux, is emitted by gas surrounding a cluster for a short period of time (~ 10 Myr, or about the lifetime of massive OB stars). Consequently, the number of $H\alpha$ detections is modest (Ferguson et al. , 1998; Martin & Kennicutt , 2001; Weiner et al. , 2001).

The two most prominent extended disks studied with GALEX so far, M83 and NGC 4625 (Thilker et al. , 2005; Gil de Paz et al. , 2005), have nearby companions, suggesting that gravitational interactions may be responsible for their extended outer disks. A more comprehensive GALEX study (Gil de Paz et al. , 2007) does contain isolated galaxies, but typically they are more distant (the majority of galaxies in the GALEX Atlas sample are > 20 Mpc away) and so only the brightest end of the knot luminosity function is sampled. To address these shortcomings, we select nearby, isolated galaxies, observe them sufficiently deeply to probe the knot luminosity function well and obtain numerous candidate knots, and develop a method to quantify the nature of the knot spatial distribution.

In complement to the imaging studies, Christlein & Zaritsky (2008) have shown that deep longslit spectroscopy can provide a measure of both the integrated extent and global disk-plane kinematics (i.e. rotation curves) of outer disks

in edge-on galaxies. While spectroscopy provides useful information, it is generally limited to knots emitting $H\alpha$. To expand the lookback time over which we can study disks, we image at redder colors to identify older candidate knots, but the drawback of this approach is that discrimination with background sources becomes more challenging.

Because we use optical observations to search for outer disk knots analogous to those detected by GALEX, we note the differences between the two sets of data. First, GALEX’s spatial resolution ($\sim 5''$ FWHM) is roughly six times larger than what we typically achieve. At the distance of NGC 3184, GALEX’s resolution element corresponds to a physical scale of ~ 270 pc, compared to the ~ 40 pc of our ground-based data. GALEX knots are typically blends of multiple clusters (Gilde Paz et al. , 2005), whereas (as we will show), we detect knots resembling individual star clusters. Second, GALEX observations are sensitive mainly to young clusters (< 500 Myr; Thilker et al. , 2005) whereas we are sensitive to clusters with ages up to several gigayears. Finally, our mass limit is lower by a factor of 10. Our LBT data will therefore provide larger numbers of knots to use in any statistical measure of the disk.

We present the initial results of a statistical study of nearby (< 15 Mpc) outer disks, using the 8.4m Large Binocular Telescope (LBT, Mt. Graham, Arizona; Hill et al. , 2006) and wide-field, prime-focus Large Binocular Cameras (LBC; Ragazzoni et al. , 2006; Giallongo et al. , 2008). We describe our data reduction, develop analysis tools, and apply these to deep V -band and U -band (hereafter V and U) imaging data of the nearly face-on (inclination = 17° ; Daigle et al. , 2006) spiral galaxy NGC 3184 ($D = 11.1$ Mpc, or $m - M = 30.23$ mag; Leonard et al. , 2002). NGC 3184 is similar to an L^* galaxy, with $M_V = -20.8$ and $M_* \sim 1.4 \times 10^{10} M_\odot$ (Moustakas et al. , 2009). We demonstrate how two separate statistical methods

enable us to trace outer disk cluster-like objects to large radii. Because the distance to NGC 3184 is uncertain at the $\sim 20\%$ level (~ 2 Mpc), all scales referenced to the frame of the disk are also uncertain at the $\sim 20\%$ level. This uncertainty in distance does not significantly affect our results. The detected correlation signals are independent of the physical size of the field.

We address the following questions here: 1) In a non-interacting galaxy, without an obvious population of GALEX knots, do we detect any evidence of an extended disk? 2) If so, what are the oldest clusters we detect? 3) How can we detect an older population of knots that is less distinct from the background galaxy population? 4) How does the extent of the disk compare to the fuel source (i.e. the gas).

In §2.3 we describe our observations, data reductions and source detections. In §2.4 we present color-magnitude diagrams (CMDs) of candidate outer disk sources and the range of cluster properties consistent with the candidate knots. We also present an estimate of disk knot radial extent determined from the CMDs in §2.4. In §2.5 we present a restricted three-point correlation analysis that increases contrast with the background and more effectively probes the extent of clustered outer disk objects. In §2.6 we present a similar clustering analysis using GALEX UV sources, and in §2.7 we present a comparison to the underlying neutral gas profile, using 21cm VLA data with a 3σ detection limit of $N(\text{HI}) = 6.9 \times 10^{19} \text{ cm}^{-2}$. In §2.8 we discuss the local environment of NGC 3184. We present a summary of our results and a brief discussion in §2.9.

2.3 Observations to Final Source Catalog

2.3.1 Observations

We observed NGC 3184 with LBC-Blue on the LBT during Science Demonstration Time on March 20, 2007. We obtained eight and nine dithered, 164-second exposures through the V and U filters, respectively, under non-photometric conditions and $\sim 0''.8$ seeing, and obtained single 164-second photometric exposures (in V and U) on February 2, 2008, together with three photometric Landolt standard star fields (Landolt, 1992) for flux calibration. The photometric exposures served their purpose but due to poor image quality we exclude them from the final science mosaics.

2.3.2 Data Reduction

We correct for both global changes and the two-dimensional structure in the bias using a set of Interactive Data Language (IDL¹) scripts created by our group. The LBC-Blue detector array consists of four 2k x 4k CCD chips (each with a gain of ~ 1.75 electrons/ADU, read noise of ~ 12 electrons and $\sim 0''.22$ -wide pixels), three aligned side-by-side lengthwise and one centered perpendicularly above them. We begin by correcting for bias gradients along columns (spanning the long axis) in the bias frames. The median within the overscan region along each row is subtracted from that row. The overscan-corrected bias frames of each chip are then median combined after removing 1σ outliers, where σ is calculated excluding the minimum and maximum values in the stack (15 frames/stack were used). We adopt an aggressive clipping (1σ) to ensure that deviant values, which artificially increase the calculated rms value, are excluded. The result is our final ‘master bias’ frames used to subtract any residual structure in an image after the

¹developed by Research Systems, Inc. and owned by ITT; <http://www.itvis.com/ProductServices/IDL.aspx>

overscan levels are accounted for. We bias-correct all raw frames in this manner and trim the overscan regions.

To correct for sensitivity variations on the CCDs, we combine dithered, twilight-sky flat-field images (10 in each band). We calculate the four-chip median value of each bias-corrected flat field exposure and divide each chip of the particular four by this median level to normalize the flat. Optical distortions in LBC-Blue can result in non-flat images (a $\sim 5\%$ effect across the field of view²). We correct for this effect later using the distortion maps created by SCAMP³ (Bertin , 2006) when aligning our individual images to a common field of view (see below). The normalized flats are then median combined after minimum/maximum and 1σ rejection as above, producing our ‘master flat’ for each chip. We complete our processing by dividing the bias-corrected science frames by the master flats, resulting in V images flat to $\sim 0.5\%$ and U images flat to $\sim 1\%$.

We next subtract the background level. Estimating the true background is made difficult by contaminating scattered light that varies sensitively with the telescope orientation, and by the extended galaxy that covers a large portion of the field in each exposure. To minimize the effects of these contaminants, we determine the background level in twenty 200×200 pixel regions distributed near the edges of the detector array using the IDL routine MMM⁴, which estimates the sky background in a stellar contaminated field by assuming that contaminated sky pixel values overwhelmingly display positive departures from the true value. We then adopt the minimum background value from the regions on each chip and subtract it from that particular chip. This process is done separately for each exposure.

²<http://lbc.oa-roma.inaf.it/commissioning/flatfield.html>

³Version 1.4.0; <http://terapix.iap.fr/soft/scamp>

⁴part of the Goddard IDL library, maintained by W. Landsman; <http://idlastro.gsfc.nasa.gov/>

To create combined images free of spurious signal or cosmetic defects, we create masks of bad columns and hot pixels for each chip interactively (based on obvious defects in the flats) and invert the masks to create the weightmaps used in the combining process. Next, we reject cosmic ray detections with the IDLUTILS⁵ routine REJECT_CR (written by M. Blanton), which rejects cosmic rays by finding features sharper than the point spread function (PSF) at $> 6\sigma$ above the background. The identified cosmic ray pixels are incorporated into the bad pixel masks.

2.3.3 Mosaic Creation

We produce our final mosaics using SCAMP and SWarp⁶. SCAMP solves the astrometry of the dithered exposures, and requires that we first create catalogs of detected sources in each exposure. To create the necessary catalogs for SCAMP, we use SExtractor (Bertin & Arnouts, 1996), restricting source detection to objects with five or more adjacent pixels for which the pixel values are at least 8σ above sky in V and 3σ above sky in U . We exclude pixels with values above 40,000 ADU when running SExtractor because these pixels produced false detections (~ 65000 ADU is the raw saturation level of the CCDs). We find that the above choices result in the best distortion maps from SCAMP (maps whose distortion level contours trace smoothly across the chip gaps), using three SCAMP iterations with tightening criteria for source matching. We use the SDSS fifth data release (DR5; Adelman-McCarthy et al., 2007) as the reference catalog to match sources in the NGC 3184 field. SCAMP provides the WCS solutions used for combining the frames with SWarp. We set the 'EXPOTIME_KEY' parameter in SCAMP to 'DONTUSE', so that the resulting fluxes are not altered by the image exposure

⁵http://spectro.princeton.edu/idlutils_doc.html

⁶Version 2.17.1; <http://terapix.iap.fr/soft/swarp>

times (we normalize the photometry to a fixed second^{-1} standard after combining the images with SWarp, when calibrating the science images to the standard star images). SCAMP is used to create the distortion maps that correct for the optical concentration effect mentioned earlier, so that the images are on the same $\sim 0''.22 \text{ pixel}^{-1}$ spatial scale before being combined into a mosaic.

The final step is to create the deep mosaics we use for source detection, calibration and analysis. We pass the output headers from SCAMP containing the WCS solutions of each exposure to SWarp, which we set to combine the spatially-aligned frames to their average values after accounting for the bad pixel masks. Total integration times in the deepest regions of the resulting mosaics are ~ 25 and ~ 22 minutes in V and U , respectively.

2.3.4 Source Detection

We build final V and U aperture photometry catalogs using SExtractor, with source detection and aperture placement based on the deeper V -band mosaic (both mosaics have the same $\sim 0''.8$ PSF, and similar image quality). After trying various combinations of parameters, we select sources by identifying groups of five or more pixels each with flux $> 1\sigma$ above the background (so typical ‘detections’ are actually $> 3\sigma$, because $[< 0.3173]^{\geq 5} < 0.0032$). For our parameter choices, we set the saturation level to be 55,000 counts to conservatively avoid problematic saturated areas (we are less concerned with false detections in the mosaic, particularly with the fine-tuned settings listed below), a seeing FWHM of $0''.8$, a pixel scale of $0''.22$, local background calculation, the background manually set as 0.0 because we have already subtracted it (note that the photometry uses the local background, however), a 3x3-pixel ‘all-ground’ convolution mask with FWHM=2 pixels for filtering to avoid spurious detections of noise peaks, a minimum contrast deblending parameter of 0.001, a ‘cleaning’ of the catalog

with an efficiency parameter of 1, a background mesh size of 32 pixels, and a background-filtering mask size of 3 background meshes. Using the same SExtractor parameters, we then perform matched-aperture photometry on the U image. A visual inspection of the detected sources confirms that the above parameters lead SExtractor to detect nearly all visually-discernable objects in the region of interest, beyond the optical radius R_{25} . Our catalog becomes noticeably incomplete below $\sim 0.8R_{25}$, where SExtractor has difficulty detecting unique sources over the extended, bright emission of the inner disk.

Given the distance of NGC 3184 (11.1 Mpc, or $m - M = 30.23$ mag), our $0''.8$ seeing (~ 40 pc at the distance of NGC 3184), and that all but the brightest OB stars would fall below our detection limit (~ 27.5 mag. for the bluest sources), the candidate outer disk objects are likely to be groupings of stars. Because we detect the integrated light from members of stellar groups, or knots (see Figure 2.1 for examples), any photometric algorithm that requires a uniform object shape for extraction is not optimal for this work.

2.3.5 Photometry & Final Source Catalog

We calibrate our photometry using photometric exposures of Landolt standard star fields, taken on the same night as our individual photometric exposures of NGC 3184, to flux-calibrate the observed standard star signal for a range of airmasses and colors. We then place the photometry of eight isolated stars in the photometric frame of NGC 3184 on the standard Vega system, accounting for the calculated airmass and color terms as well as the different exposure times, and finally bootstrap the photometry of the deep mosaic using these same stars.

Colors and magnitudes are measured using circular apertures. Colors quoted throughout are from fixed four-pixel-diameter apertures ($0''.9$ or ~ 48 pc at NGC 3184, just larger than the typical $0''.8$ FWHM of detected sources), while V magni-

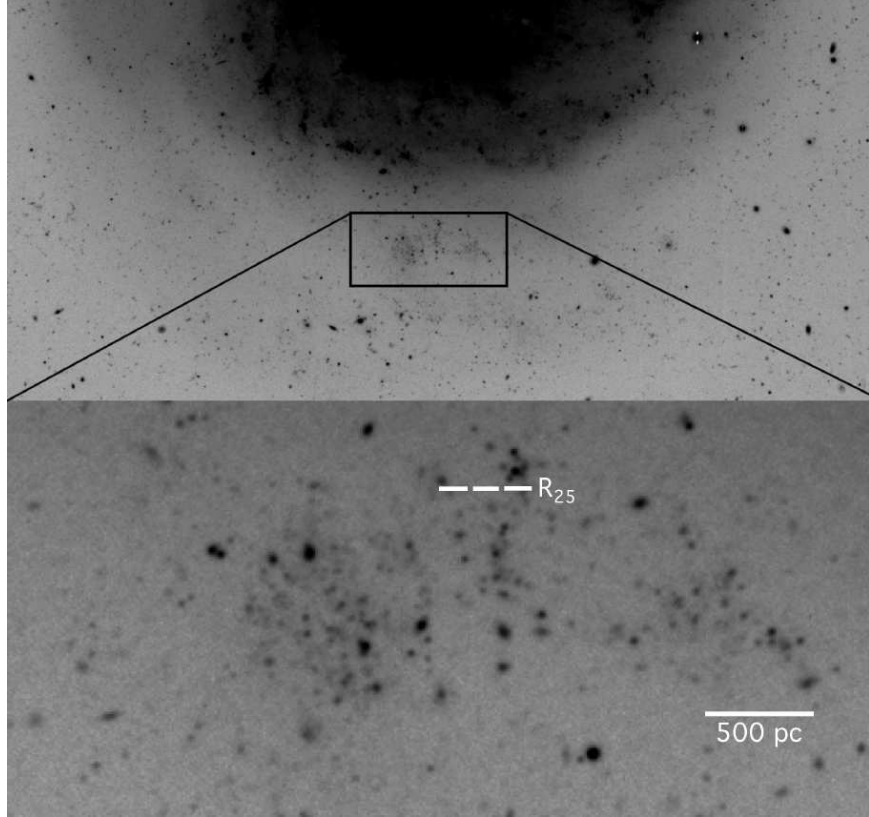


Figure 2.1 A portion of our deep V -band mosaic, with a zoom-in on a complex of faint knots near the optical radius. The optical radius (R_{25}) and a 500 pc scale bar are shown in white in the lower image. Many of the knots are marginally-resolved, non-uniform sources. The majority of sources in this zoomed-in view have colors far bluer than the typical background galaxy and are grouped in a manner to suggest that they are in fact disk objects. The physical scales of the individual knots is ~ 40 pc at the distance of NGC 3184.

tudes are from 10-pixel-diameter apertures ($2''.24$ or ~ 121 pc at NGC 3184) and aperture-corrected using stellar curves-of-growth by -0.08 mag. Aperture corrections were calculated from eight isolated, unsaturated stars measured in 15 apertures spanning $2 - 50$ pixels in diameter (or $0''.4 - 11''.2$). To the degree the knots are resolved, our aperture corrections will underestimate the total flux. We choose the 10-pixel-diameter apertures so as to include the bulk flux from the many marginally-resolved extended sources visible in the images while not including too many neighbors (see Figure 2.1; false-color composite images are available from the electronic version of the paper). We set SExtractor to mask and correct neighbors that contaminate.

In our final catalog, we only include sources whose $U - V$ color error is < 0.5 mag (magnitude errors are provided by SExtractor and propagated in the standard manner). This leaves ~ 4500 sources between $1.0 - 1.5R_{25}$, the ‘outer disk region’ we examine below (the outer limit, $1.5R_{25}$, is an arbitrary choice here).

As a check of our photometry, we compare the apparent magnitudes of ten well-isolated objects across the field with those provided by SDSS-DR5, converted from u , g , and r to either V or U using the transformations of Jester et al. (2005). We find that our results are consistent with the transformed SDSS photometry to within the transformed SDSS and LBT photometric errors.

2.4 Cluster Populations Surrounding NGC 3184

Figure 2.2 shows the CMD of all detected sources between $1.0 - 1.5R_{25}$ ($R_{25} \sim 3.45$ arcmin, or ~ 11.1 kpc). Overplotted in black are Starburst99 (Leitherer et al. , 1999; Vazquez & Leitherer , 2005) models of fixed mass, solar metallicity star clusters covering a range in their evolutionary sequence from 1 Myr to 3 Gyr. The upper and lower tracks are of $10^4 M_{\odot}$ and $10^2 M_{\odot}$ model clusters, respec-

tively, scaled down in mass/magnitude from a simulated $10^6 M_\odot$ cluster that adequately samples the Kroupa IMF. The scaled tracks are meant as a general guide only; the stochastic sampling of the IMF at low cluster masses (Cerviño & Luridiana, 2004; Fagiolini et al., 2007) is not accounted for in the following knot mass and age estimates. The uncertainties from the stochastic sampling are larger for the lower-mass and younger clusters, and a scaled-down model cluster track (from a well-sampled IMF) becomes systematically brighter and bluer than real clusters would be at a particular age (the tracks represent contributions from the highest-mass stars, which are increasingly unlikely to be found in real low-mass clusters). As a result, comparisons with the scaled model tracks can lead to underestimates of cluster masses and overestimates of their ages. Our aim here is to provide a general impression only of the cluster masses and ages consistent with the knots in our sample.

To statistically constrain the color and magnitude range of sources most likely associated with NGC 3184, we create background-subtracted Hess diagrams. A Hess diagram plots the number of sources within chosen color-magnitude bins across a CMD. The extent of the remaining signal in the background-subtracted diagrams provides an estimate of the size of the outer disk. To create these diagrams, we first produce a ‘background’ CMD from sources detected in an outer annulus between $2 - 3 R_{25}$. We also create a ‘disk+background’ CMD from the region of interest and then count the number of sources found in bins of color and magnitude (square bins of 0.2 mag were used here). We then scale the background Hess diagram to match the area on the sky represented by the disk+background Hess diagram. Finally, we subtract the scaled background Hess diagram from the disk+background Hess diagram to reveal the signal above the background.

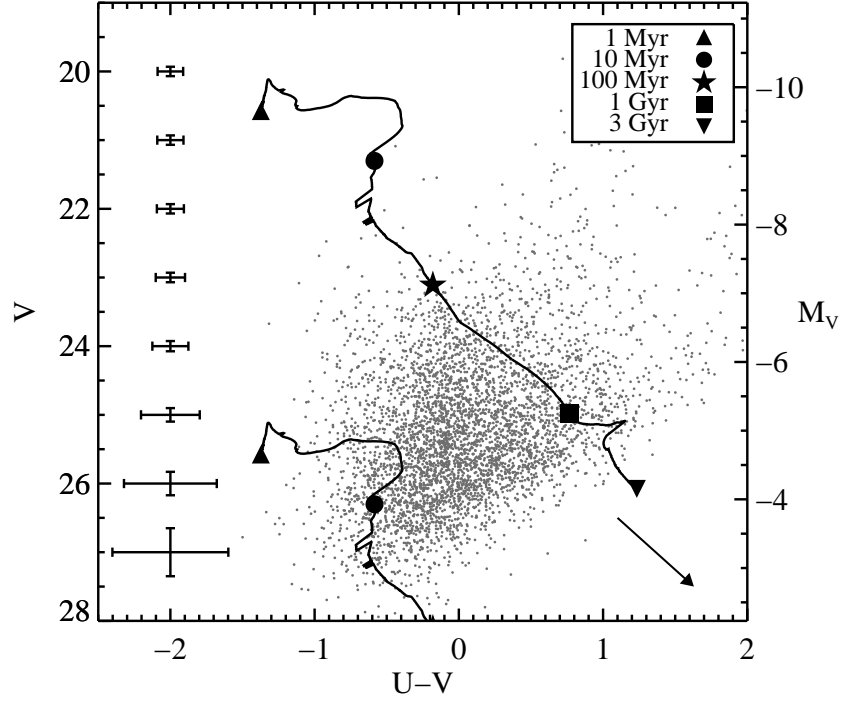


Figure 2.2 CMD of ~ 4500 sources between $1.0 - 1.5R_{25}$ from our final catalog, with median 1σ errors descending the plot at left. A reddening vector corresponding to 1 magnitude of extinction in V , calculated using results from Rieke & Lebofsky (1985), is shown at lower right. See the text for a description of the Starburst99 model tracks.

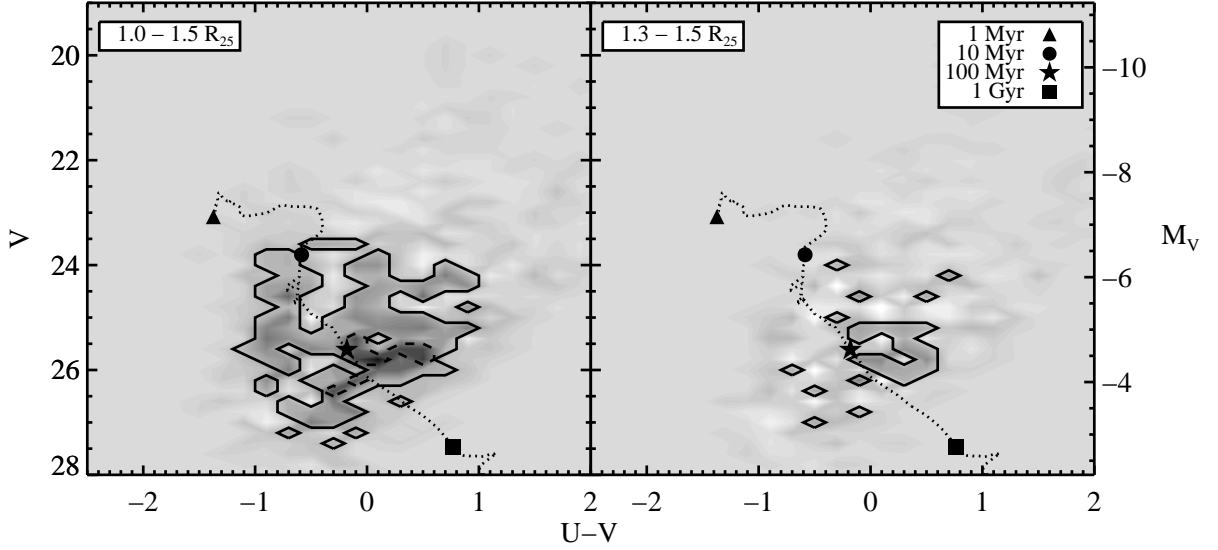


Figure 2.3 Background-subtracted Hess diagram showing the number of sources remaining between $1.0 - 1.5 R_{25}$ (left panel; dark regions are positive counts) and between $1.3 - 1.5 R_{25}$ (right panel). Solid and dashed black contours outline signal lying above the background at $> 90\%$ and $> 99.9\%$ CL, respectively. Overplotted is a $10^3 M_{\odot}$ Starburst99 model cluster, scaled down from a $10^6 M_{\odot}$ cluster as in Figure 2.2. *Left:* this ‘outer disk CMD’ shows a faint blue plume of sources near $U - V = -1$. The strongest signal arises from redder sources at faint levels ($V \sim 26$ mag.). From the original ~ 4500 sources in Figure 2.2, ~ 1100 (or $\sim 1/4$) remain after accounting for the scaled background CMD; taking the residual distribution of sources in V leads to an effective surface brightness estimate of ~ 30.3 mag arcsec $^{-2}$ for the outer disk knots. *Right:* this version only shows weak signal above 90% CL and none $> 99.9\%$ CL. In the outermost regions of the disk, it is the reddest sources that dominate by number. From the original ~ 1600 sources detected in this radial range, just ~ 200 (or $\sim 1/8$) remain; accounting for their distribution in V leads to an effective surface brightness estimate of ~ 32.1 mag arcsec $^{-2}$.

Figure 2.3 contains background-subtracted Hess diagrams of regions between $1.0 - 1.5 R_{25}$ and $1.3 - 1.5 R_{25}$ in the left and right panels, respectively. We use low-count, Poisson single-sided upper and lower limits from Gehrels (1986) to outline signal lying in excess of the background at the $> 90\%$ and $> 99.9\%$ confidence level (CL). We detect a statistically significant knot population in the outer disk of NGC 3184. The strength of the signal fades quickly with radius, and the right panel of Figure 2.3 suggests that $\sim 1.4 R_{25}$ is the limit of how far this method can probe the outer disk.

Although outer disk knots are typically thought of as being young because they were discovered in the UV, we find that the population of knots redward of $U - V = -0.2$ dominates that of bluer ones. The younger, blue population of knots is only detected near the optical radius with this method. However, we cannot distinguish between dust and age as the primary driver of color; we assume insignificant reddening of the majority of outer disk sources, but caution that the relative numbers of young vs. old knots is uncertain because of this issue.

In Figure 2.2 a $10^4 M_{\odot}$ model star cluster track for ages between 100 Myr and 1 Gyr provides an envelope for the bright end of the distribution. Above this track the number of objects falls off rapidly, implying that whatever outer disk objects are in this sample, the majority have masses $< 10^4 M_{\odot}$. Our catalog becomes incomplete for objects resembling $10^4 M_{\odot}$ clusters older than ~ 1 Gyr, and the age where this incompleteness sets in decreases quickly with decreasing cluster mass. A $100 M_{\odot}$ track suggests that at the low-mass end our final catalog is restricted to objects younger than a few tens of Myr, although this estimate is more uncertain due to the previously-discussed stochastic sampling of the IMF. Because one massive O-star forms per $200 - 300 M_{\odot}$ of stars in a cluster (Parker & Goodwin, 2007, and references therein), many outer disk clusters detected here may host

only a few O-stars, and many may contain none at all.

Although not well-constrained with the available optical data (i.e. V & U only), our estimated cluster mass range ($\sim 10^2 - 10^4 M_\odot$) matches that found in the extended disk of NGC 4625 (see Gil de Paz et al. , 2005, their Figure 4). Those authors examined GALEX FUV-selected complexes in the outer disk of NGC 4625 that also show corresponding $H\alpha$ emission, and found that the majority of detected knots (or clusters) lie between $10^3 - 10^4 M_\odot$, with the lowest-mass knots resembling $\sim 500 M_\odot$ clusters. A knot containing fifteen $20 M_\odot$ O-stars would lie just among the range of young (< 10 Myr) $\sim 10^3 M_\odot$ clusters (Figure 4, Gil de Paz et al. , 2005), similar to what we expect to find in our images of the outer disk of NGC 3184. The distinction between our data and that from GALEX is that we have superior spatial resolution and in principle can find older clusters. The strength of the GALEX data relative to ours is that the young clusters are more prominent relative to background sources.

2.5 Clustering of knots in the outer disk

Another way to estimate the outer disk extent is to consider the spatial distribution of knots most likely associated with NGC 3184. Here we present correlation functions to trace the self-clustering of knots in the outer disk. To maximize whatever correlation signal exists, we must increase the contrast between the sources of interest and the background. In the FUV and NUV bands of the GALEX images, the blue star-forming knots stand out sharply against the redder background galaxies. Zaritsky & Christlein (2007) exploited this color contrast in the GALEX data and calculated the two-point correlation function of detected sources around nearby galaxies, to quantify the ubiquity of any extended disk component. Their main result was that five of the eleven galaxies studied show

an excess of sources between $1.25 - 2R_{25}$, which statistically implies that at least a quarter of such galaxies have an extended blue knot population.

We would like to use a statistical method similar to the two-point correlation analysis of Zaritsky & Christlein (2007) to measure the extent of NGC 3184's outer disk with our LBT data. The two-point correlation approach would work well here if NGC 3184 had large numbers of blue knots in its outer disk, because they would create the sharp color and number density contrast required to isolate them from the background. Due to the lack of blue outer disk sources, and that the dominant red sources have similar $U - V$ colors to the background objects (Figures 2.2 & 2.3), the Zaritsky & Christlein (2007) approach is not effective with our optical data. Note that a particular red color cut *can* be applied to provide enough contrast for a significant two-point correlation function to be made in the inner disk, but this correlation quickly becomes insignificant beyond R_{25} .

We must find another way to accentuate the contrast between knots and the background and thereby maximize whatever two-point correlation function signal may exist in the outer disk. As evident in Figure 2.1, the knots cluster about themselves. We use this self-clustering of knots as a means to provide the necessary contrast with the background; we assume that the background sources (mostly galaxies) do not cluster on scales similar to the disk objects. We then ask, 'how far can we trace clustered knots?'

To measure the clustering of knots as a function of galactocentric distance, we calculate a 'restricted' three-point correlation, for which one of the 3 points is always defined to be the center of the galaxy. We begin by selecting sources by color and magnitude to have rough mass and age constraints. We then calculate the two-point knot-knot correlation at each radius. Specifically, for each knot we calculate the distance to neighboring knots (r_{out} - see Figure 3.16), bin

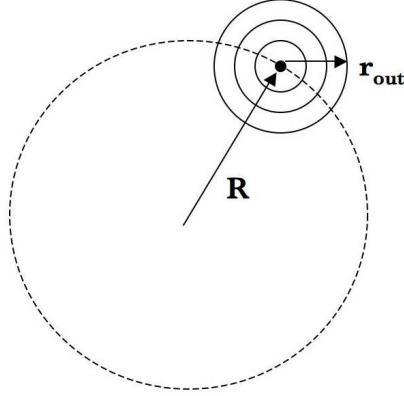


Figure 2.4 The radii defined for creating the restricted three-point correlation maps.

the distribution of distances, and obtain an estimate of the two-point knot-knot correlation function at the galactocentric radius R of this individual knot. We repeat this process for every knot and bin in R to obtain the raw version of the restricted three-point correlation map.

The raw restricted three-point correlation map must be corrected for several effects. Because we are attempting to isolate the self-clustering signal of disk-only knots as a function of radius, we must first account for contaminating correlation signal in the raw map arising from the given distribution of knots in the field at all R (both disk and background sources), as well as for contaminating signal from any spatially-correlated background galaxies. First, we normalize the two-point correlation function at each R by dividing by the number of knots at that radius, divide by the background number density of sources calculated in an annulus at large R , and subtract 1 from the result so that the ‘unclustered’ signal is zero. Second, we correct for the underlying ‘self-correlation’ of knots across the field via Monte-Carlo simulations. Self-correlation arises because the knots are correlated with the galaxy, and so will appear correlated with each other even

if the outer disk has absolutely no intrinsic clustering. To calculate and subtract this we generate 500 three-point correlation maps, similar to the original but each time randomizing the knots in angle about the galactic center. This approach preserves the source density gradient with R (which we do not wish to remove) while providing a measure of the self-correlation of a disk with no knot clustering. Subtracting the average of these 500 realizations then provides a measure of the intrinsic knot clustering. Lastly, we use the two-point correlation function at large R to subtract the underlying galaxy-galaxy correlation function (i.e. the apparent clustering of background galaxies). If there were no outer disk knots, then the correlation function along r_{out} would simply be the galaxy-galaxy correlation function and be independent of R . By subtracting the r_{out} correlation as measured at large R (beyond $2.5R_{25}$), where there presumably are no outer disk knots, we have removed the effect of contaminating galaxies. The average amplitude of the random ‘self-clustering’ correction (due to the distribution of all sources in the field) is equal to the average amplitude of the raw correlation signal at large r_{out} (> 1.5 kpc), indicating that the knots are not self-clustered on large scales. The average amplitude of the background galaxy-galaxy correction is thus also similar to the random-self-clustering-corrected signal at large r_{out} , because the signal now remaining in these regions is due only to background galaxy-galaxy clustering. At smaller r_{out} , particularly where we detect statistically-significant signal in the final map (described below), the amplitude of this galaxy-galaxy correction is negligible compared to the signal remaining from disk objects.

We use the scatter from the random realizations to set the significance level of positive excursions in the correlation map. Taking the scatter from a ‘background’ region of the random maps is insufficient, however. Due to the source distribution in the field and the different annuli area used in constructing the

maps, the scatter is not uniform. From our 500 realizations we identify excursions that have only a 5% or 1% chance of occurring at that particular R, r_{out} combination. Filled contours connecting these R, r_{out} ‘pixel’ excursion values define the two-dimensional 95% and 99% significance thresholds in the map. The resulting background of noise peaks in the map (on scales of the $R - r_{out}$ binsize) can sometimes make it difficult to confidently attribute signal to actual knots clustering in the disk. In the more obscure cases, clues from the larger structure of the disk may help.

Figure 2.5 shows the final restricted three-point correlation signal above the 95% and 99% significance thresholds (in black and grey shading, respectively) from ‘all’ sources with $-1.7 < U - V < 0.7$ and $18 < V < 27.5$ (top panel), and from the sample split into ‘blue’ and ‘red’ on either side of $U - V = -0.2$ (middle and bottom panels, respectively). If dust significantly reddens outer disk clusters, then the strength of the correlation results presented will be underestimated for young sources and overestimated for older sources.

The choice of the red extreme in our $U - V$ color cut (0.7) was motivated by two requirements: to retain the majority of knots most likely associated with NGC 3184 while excluding the maximum number of background sources (mostly galaxies). Fukugita et al. (1995) show that the $U - V$ colors of $z = 0.2$ late-type spirals are near 0.8. Because these and earlier-type galaxies dominate the background, we chose $U - V < 0.7$ as the red extreme, with the assumption that this cut retains the majority of knots likely associated with the outer disk of NGC 3184 (Figure 2.2 shows that we will retain the majority of sources between $1.0 - 1.5R_{25}$). However, because galaxies become bluer in this set of filters as z increases, we expect increasing contamination from more distant galaxies. This is exacerbated by the evolution of galaxies because galaxies are typically brighter

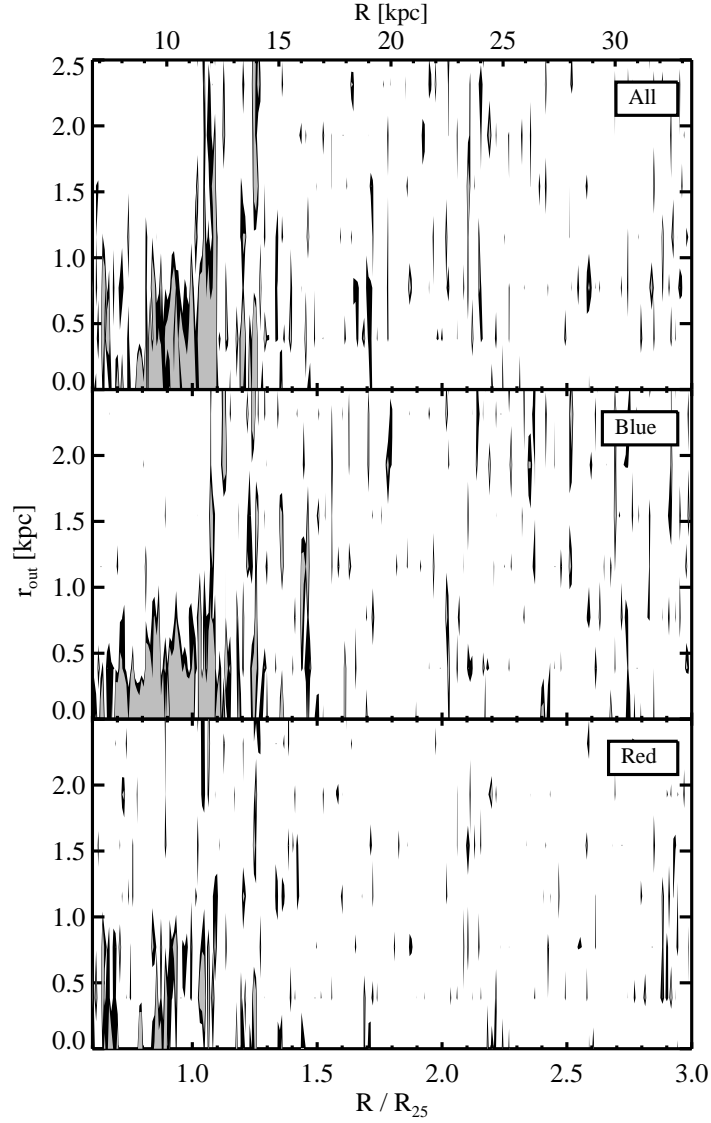


Figure 2.5 Restricted three-point correlation maps from sources in our final catalog. The top panel is from all sources with $-1.7 < U - V < 0.7$ and $18 < V < 27.5$, while the lower panels result from splitting the sample into blue and red components on either side of $U - V = -0.2$ (middle and bottom panel, respectively). Black and grey show areas where signal is detected at the $> 95\%$ and $> 99\%$ significance level, respectively, as a function of both R and r_{out} .

and bluer at higher redshift. Using standard Λ CDM cosmology, the tabulated colors from Fukugita et al. (1995) and L^* from Blanton et al. (2003), we find that for $V > 23$ L^* Scd galaxies are included for $z > 0.6$. It is therefore not feasible to select a $U - V$ color cut that effectively eliminates galaxy contamination to the limits of our photometric sensitivity. Because we do not exclude all background galaxies with our color cut, we require a method to statistically distinguish knots from the background—hence the correlation map approach. It is important to note that the red cut is the only form of color contrast we use to distinguish outer disk sources from the background.

The final restricted three-point correlation maps provide another method to estimate the extent of the outer disk (the first being the background-subtracted Hess diagrams). The blue sources cluster uniformly to just beyond the optical radius, and then break into discrete aggregates that are detectable out to $\sim 1.5R_{25}$. While the red knot correlation signal is noisier, presumably due to less color distinction with the background and a less clustered distribution, there remain regions of significant clustering signal at radii comparable to those found in the blue sources. The red map is made using $\sim 1.8\times$ more sources than the blue map. Regions of increased signal along r_{out} in the blue source map (e.g. at 0.71 , 0.85 , 0.94 , and $1.05R_{25}$) trace overdensities of knots along the spiral arms seen in the images, as do the few regions of increased signal in the red map. The regions of increased clustering signal common to both the blue and red maps near $0.9R_{25}$ and $1.05R_{25}$ can be visually attributed to large aggregates of knots seen in the images. For example, the overdensity near $1.05R_{25}$ is likely influenced by the large aggregate shown in the bottom half of Figure 2.1.

Due to the irregular signal in Figure 2.5, it is difficult to measure the radial extent of the outer disk directly from these maps. One way to better estimate

the radial extent is to average the correlation signal below a chosen r_{out} and determine the R at which the average signal falls below the local averaged significance thresholds. When this is done using the fine R binning of Figure 2.5, a correspondingly irregular average with R is produced (not shown). Rebinning the R -annuli to be $\sim 12\times$ coarser than in Figure 2.5 (to ~ 1.5 kpc per bin) results in Figure 2.6, which presents a smoother trace of average correlation signal in R for $r_{out} \leq 0.5$ kpc. Also plotted are the corresponding average 95% and 99% significance thresholds in dotted and dashed linestyle, respectively, made from averaging similarly resampled threshold maps at regions $r_{out} \leq 0.5$ kpc to match the data map averaging. There is clustering signal in both the blue and the red knots to $\sim 1.4 - 1.5 R_{25}$. Also shown in Figure 2.6 are the approximate extents of the H I gas disk from two column density thresholds (see the caption and §6 for details).

Surface brightness measurements of the disk at these radii may be quite difficult. We defer a detailed surface brightness analysis of the diffuse stellar component to an upcoming paper, where we will first account for low-level scattered light in the mosaics. Here we estimate the *effective* surface brightness (eSB) of knot aggregates that can be detected in our correlation maps. We have inserted mock aggregates at different radii to determine the projected number density of knots necessary to produce a significant signal in our restricted three-point correlation maps. The mock aggregates are simply groupings of ‘detection’ locations added to the field of real knot detection locations; once a knot is counted as a detection within a particular color-magnitude cut, the shape and color of the knot are irrelevant for the construction of the correlation maps—only the locations of the detections are important. We therefore make no assumptions of the detailed shapes or colors of the fake knots, other than they satisfy the same criteria as

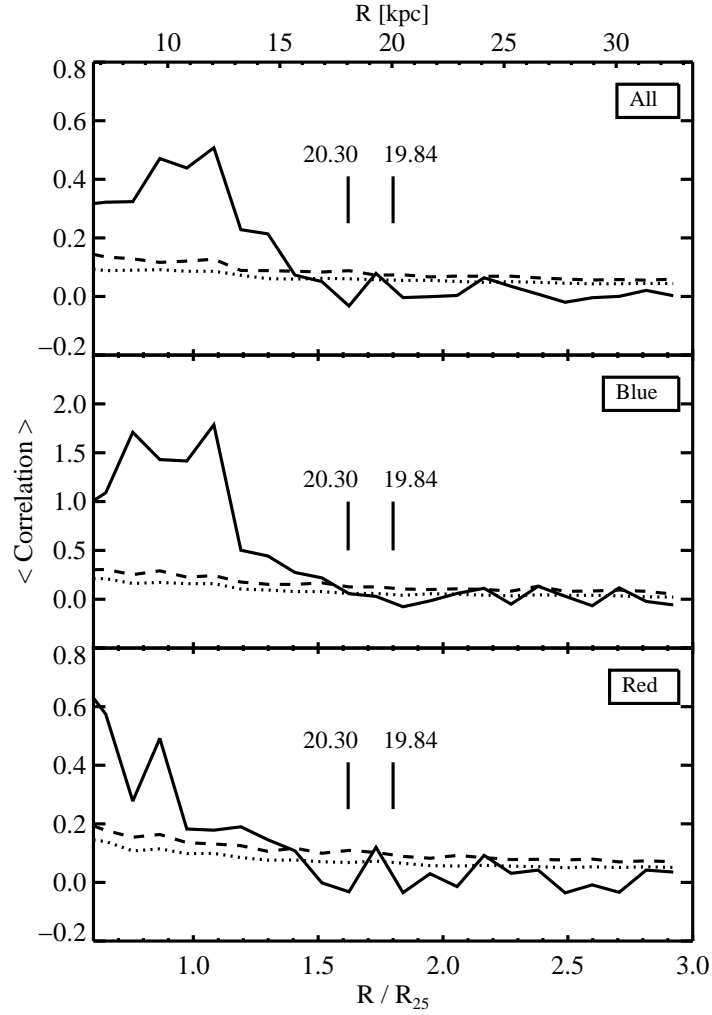


Figure 2.6 Average correlation signal from areas $r_{out} \leq 0.5$ kpc in restricted three-point correlation maps similar to those of Figure 2.5. The top, middle and bottom panels are from the same all, blue and red samples of Figure 2.5. The dotted and dashed lines mark the 95% and 99% significance thresholds, respectively. Both the blue and red sources extend globally out to $\sim 1.4 - 1.5 R_{25}$. Also marked are the approximate radial extents of H I gas for two different boundaries, $N(\text{HI}) > 2 \times 10^{20} \text{ cm}^{-2}$ and $6.9 \times 10^{19} \text{ cm}^{-2}$, corresponding to the damped Lyman- α (DLA) system threshold and the 3σ threshold of our H I map, respectively. See §6 for more details of the H I data. The significant clustering signal from the blue knots extends nearly to the DLA system threshold.

the real knots to have made it into the final sample being considered. We find that a complex of $0.08 \text{ knots arcsec}^{-2}$ (eight knots randomly distributed within a circular area of diameter $11''/2$) at $1.4R_{25}$ would be detected as significant signal (above the 99% significance threshold) in a map like those of Figure 2.5. Combining these numbers with the apparent magnitudes from our faintest detected sources (27.5 mag in V) leads us to a limiting V -band eSB of $\sim 30.2 \text{ mag arcsec}^{-2}$ for a significantly clustered aggregate at the limit of our photometric sensitivity. This eSB is similar to the outer disk eSB found from the $1 - 1.5R_{25}$ background-subtracted Hess diagram in Figure 2.3 ($\sim 30.3 \text{ mag arcsec}^{-2}$), although we caution that these estimates represent different samples of objects generated by separate methods. The eSB estimated from the outermost ~ 200 sources remaining in the $1.3 - 1.5R_{25}$ background-subtracted Hess diagram is $\sim 32.1 \text{ mag arcsec}^{-2}$. For comparison (primarily to the eSBs estimated from our background-subtracted Hess diagrams), V -band outer disk eSBs estimated from star counts in M31 (Irwin et al. , 2005) and NGC 300 (Bland-Hawthorn et al. , 2005) are $\sim 32 \text{ mag arcsec}^{-2}$. Low surface brightness isophote fitting is typically limited to $\sim 28 \text{ mag arcsec}^{-2}$ due to a range of technical challenges (Bland-Hawthorn et al. , 2005), and so going fainter typically requires a resolved population. Our eSBs are from cluster-like knots rather than individual stars, however; NGC 3184 is too distant for detecting any but the brightest individual stars from the ground. Although we have not yet carried out a surface brightness analysis of the diffuse outer disk component of NGC 3184, we can estimate the expected surface brightness at large radii using results from the literature. Using Pompei & Natali (1997) and Godwin et al. (1977), we estimate the diffuse stellar component to be $\sim 28 \text{ mag arcsec}^{-2}$ at $1.5 R_{25}$, or $\sim 2 - 4 \text{ mag}$ brighter than the eSBs found from the knots in Figure 2.3.

2.6 A comparison to GALEX UV source extent

Our three-point correlation technique can be easily applied to other datasets. Figure 2.7 shows the resulting correlation map when considering all GALEX UV sources near NGC 3184. The GALEX sources were collected from a search of the Multimission Archive at STScI⁷ which provides a catalog of detected sources and their associated photometry. Unfortunately the available GALEX data of this field is very limited, with only very shallow (~ 100 second) exposures from the All Sky Imaging Survey (AIS) publicly available. Figure 2.7 is therefore made from only the brightest knots around NGC 3184, corresponding to cluster masses of $\sim 10^4 M_\odot$ or larger. Because the majority of our cluster-like detections correspond to $M < 10^4 M_\odot$ (Figure 2.2), these GALEX data trace a different cluster population. We expect that the correlation map of Figure 2.7 would reveal structures comparable to those of Figure 2.5 with deeper GALEX data, although the resolution of the clustering in r_{out} would be lower due to the $\sim 6\times$ coarser spatial resolution. The correlation signal near $1.3 R_{25}$ on scales $1 < r_{out} < 2$ kpc comes from the distribution of knots just visible in the GALEX images near the outskirts of the disk, seemingly associated with extended spiral arms. The detections decline in the inner disk, presumably because it is more difficult to detect individual knots over the bright extended emission.

2.7 A comparison to the underlying neutral gas profile

We now compare our estimates of the stellar/cluster disk extent to the size of the underlying gaseous disk. We begin by measuring the extent of the neutral gas disk from existing 21cm Very Large Array (VLA) imaging of NGC 3184. The beamsize of the C-configuration data is $10''$ with natural weighting (each visibil-

⁷MAST; <http://galex.stsci.edu/GR4>

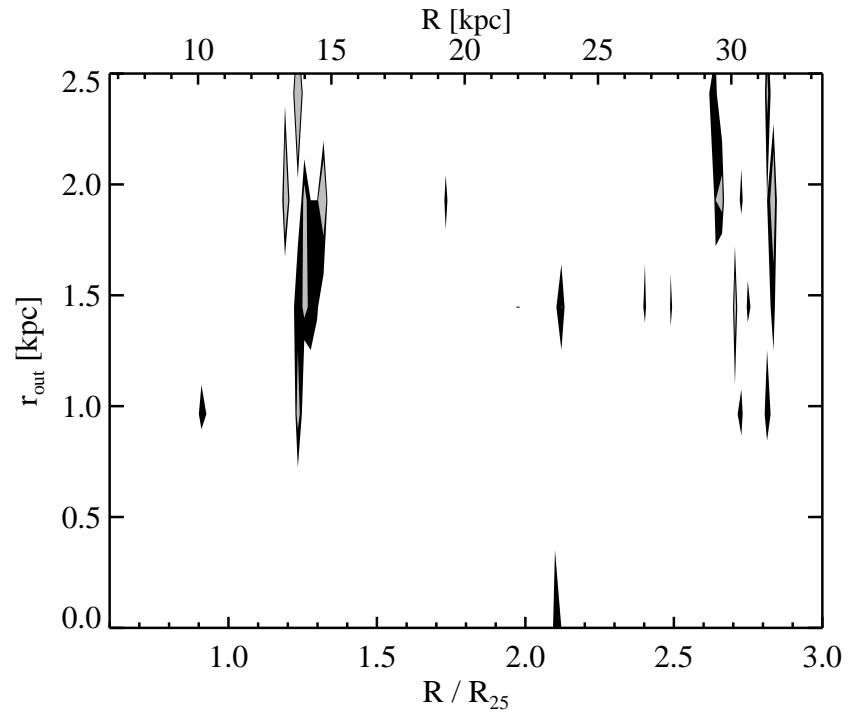


Figure 2.7 Same as Figure 2.5, but here using publicly-available GALEX AIS sources.

ity is weighted by the inverse of the noise variance, giving more weight to shorter baselines and larger spatial scales). The Astronomical Image Processing System⁸ software package was used to reduce the data. Figure 2.8 shows the 3σ $N(\text{HI})$ extent ($N(\text{HI}) = 6.9 \times 10^{19} \text{ cm}^{-2}$) overlaid on a portion of our deep LBT V -band mosaic. To quantify the H I radial extent, Figure 2.9 presents histograms showing the number of H I pixels per kpc^2 above two $N(\text{HI})$ threshold values, as a function of R in $0.025R_{25}$ -wide annuli (chosen for a smooth, well-sampled trace of the decline). We use circular annuli for convenience; the inclination of NGC 3184 is 17° (Daigle et al. , 2006), or nearly face-on. The top panel is of pixels with $N(\text{HI}) > 6.9 \times 10^{19} \text{ cm}^{-2}$ (the 3σ threshold and contour shown in Figure 2.8), and the bottom panel is of pixels with $N(\text{HI}) > 2 \times 10^{20} \text{ cm}^{-2}$. The latter value was chosen to match the damped Lyman- α (DLA) system threshold, which distinguishes between predominantly neutral and predominantly ionized gas (see Wolfe et al. , 2005, and references therein). The $N(\text{HI}) = 2 \times 10^{20} \text{ cm}^{-2}$ boundary represents the edge of the dominant reservoir of neutral gas available for star formation in the disk. We estimate the gas disk extent to be $1.62R_{25}$ and $1.80R_{25}$ for the DLA and 3σ thresholds, respectively. Comparing these extents to those of the knots found using our Hess diagrams and three-point correlation maps ($\sim 1.4 - 1.5R_{25}$; Figures 2.3 & 2.6), we see that the optical disk extends at least to just below the DLA system threshold, but that the full 3σ $N(\text{HI})$ gas disk extends to larger radii.

The degree to which the extended cluster and gas disks are related can be quantified by the cross-correlation of LBT-detected knots and detected H I signal. This cross-correlation can be used as another method to trace the extent of the optical disk, in the case where the knots do not cluster about themselves but

⁸AIPS; <http://www.aips.nrao.edu/>

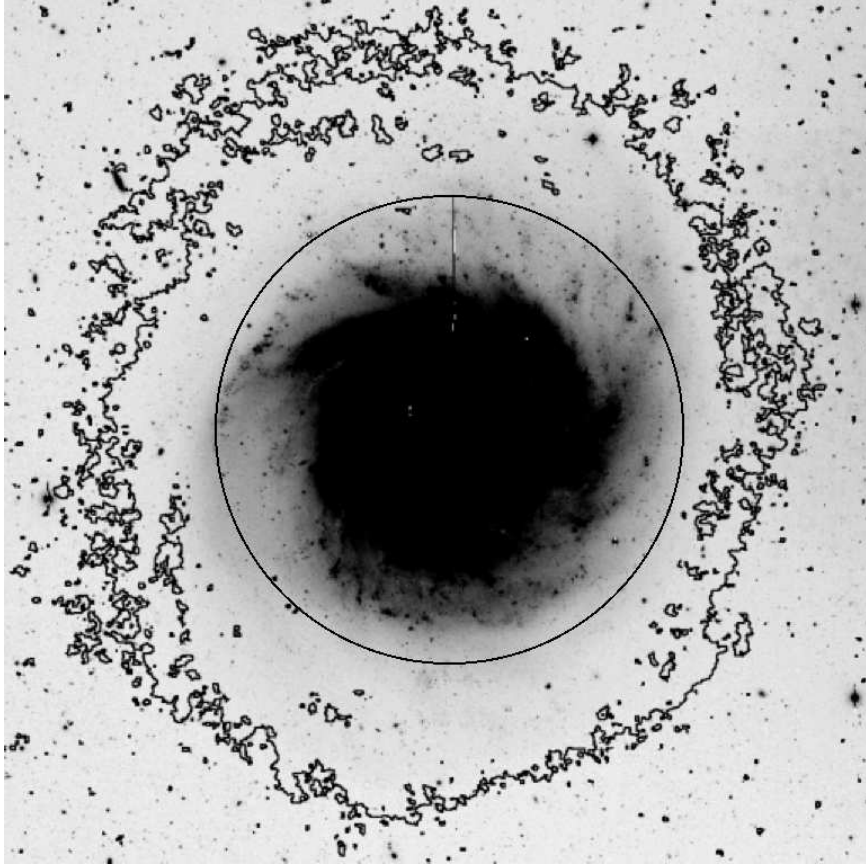


Figure 2.8 The central portion of our deep LBT/LBC V -band mosaic with the $3\sigma N(\text{HI})$ threshold in black contour. This image is $\sim 3.7R_{25}$ or $\sim 12.9'$ on a side (the black circle has a radius of R_{25}). The gas disk extends beyond our detections of the outermost regions of the optical disk, as probed by our background-subtracted Hess diagrams and restricted three-point correlation maps.

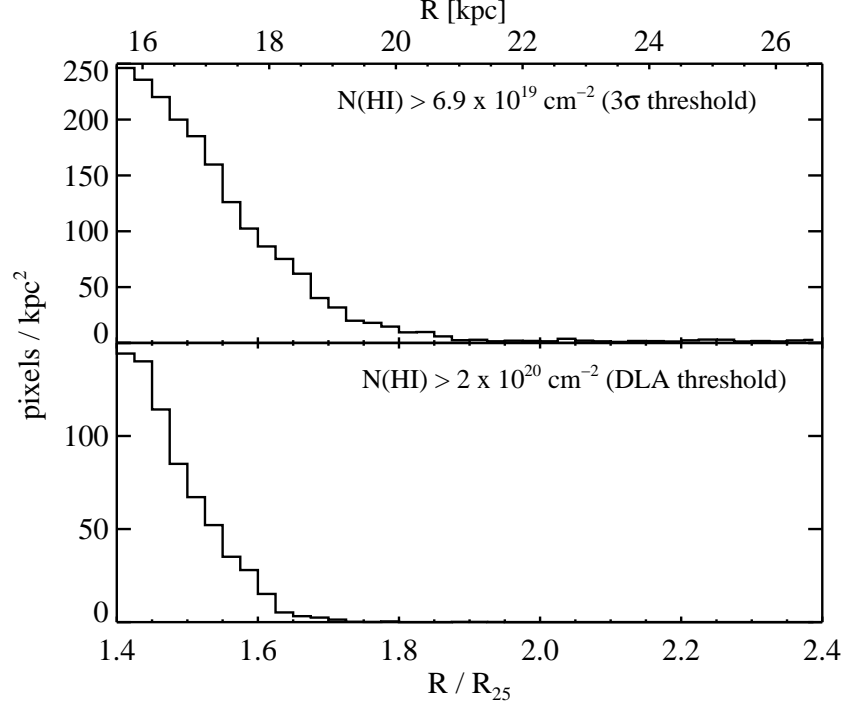


Figure 2.9 Histograms showing the number of H I pixels with $N(\text{HI}) > 6.9 \times 10^{19} \text{ cm}^{-2}$ (top) and $N(\text{HI}) > 2 \times 10^{20} \text{ cm}^{-2}$ (bottom) per kpc^2 in circular annuli of width $0.025R_{25}$. We estimate the radial extent of the H I gas above the 3σ and DLA thresholds to be $1.80R_{25}$ and $1.62R_{25}$, respectively. These extents were marked on Figure 2.6 to compare with the extent of clustered knots from the correlation map approach.

rather with the H I gas. The latter would be expected (on small r_{out} scales) if the knots formed directly from the gas in the extended disk (discussed further in §8). We construct restricted three-point cross-correlation maps in a similar manner as the knot-knot correlation maps but instead using H I pixels above the $3\sigma N(\text{HI})$ threshold ($6.9 \times 10^{19} \text{ cm}^{-2}$; Figure 2.8) as the objects surrounding a particular LBT-detected knot. We also do not subtract a background galaxy correlation signal from the maps because optical background galaxies are not correlated with the 21cm peaks in the background of the H I map. The knot-knot clustering analysis showed that the optical disk extends to at least $1.4R_{25}$, so we have restricted the lower boundary of radii considered here to $1.3R_{25}$ (H I and knot data below $1.3R_{25}$ was ignored when making these maps). The upper range of the radii considered here is $2.4R_{25}$ due to the extent of available H I data. The upper, middle and lower panels of Figure 2.10 show the knot-H I pixel cross-correlation signal from the all, blue and red samples, respectively. We remind the reader that spurious ‘significant’ signal is to be expected across the map at the 1 – 5% level, given the large number of resolution elements in the map, and so it is sometimes difficult to know if a particular signal in a map is real. Features viewed with skepticism, especially those at large R or r_{out} , or those seen in the map of one sample (blue or red) but not in the all map, should be confirmed or refuted with further observations. Here we find strong blue knot-H I pixel clustering signal at $1.45R_{25}$ extending to $r_{out} \sim 15 \text{ kpc}$, likely due to knots distributed along a tightly wound H I spiral arm seen in the H I image at $\sim 1.45R_{25}$. The red knot-H I pixel cross-correlation map shows significant extended signal near $1.73R_{25}$ between 5–10 kpc in r_{out} . This signal likely results from knots lying along another H I spiral arm near the diffuse edge of the H I pixels considered here (see Figure 2.8 and 2.9); it is however surprising that the red knots are the ones that correlate at these

distances with the H I. Assuming that the cross-correlation signal at large R in the red map is real, the results of Figure 2.10 show that we can trace knots farther out with the knot-H I cross-correlation than with the knot-knot correlation presented in §4. While correlations with the H I on these scales are unlikely to result from in situ formation of the knots, this cross-correlation technique still provides an estimate of the radial extent of knots tracing extended spiral structure in the gas.

2.8 The local environment of NGC 3184

There have been suggestions that star formation in outer disks is triggered by galactic interactions. Two of the most extended UV disks discovered by GALEX (M83 and NGC 4625, both with UV knots extending to four times their optical radii; Thilker et al. , 2005; Gil de Paz et al. , 2005) are both from interacting systems. Here we search the local environment of NGC 3184 for any possible perturbers.

Tully (1988) has shown that NGC 3184 belongs to a small association of galaxies consisting of three others (NGC 3104, NGC 3198 and NGC 3319). Although our optical and H I images show no obvious morphological signs of disturbance (perhaps some low-level lopsidedness in the gaseous component, see Figure 2.8), the $H\alpha$ velocity field of NGC 3184 from Daigle et al. (2006) does suggest kinematic anomalies, particularly towards the outer regions. Using the criteria of Bailin et al. (2008) to select candidate satellite galaxies most likely associated with a host, we query NED⁹ for extragalactic objects within 700 kpc of NGC 3184 (at the distance of NGC 3184, or within $\sim 215'$) and with $\Delta v < 750 \text{ km s}^{-1}$ and find ten candidate satellites near NGC 3184. Seven of these ten appear to be very small and faint in SDSS-DR5 images, however, and one of the remaining three is

⁹<http://nedwww.ipac.caltech.edu/>

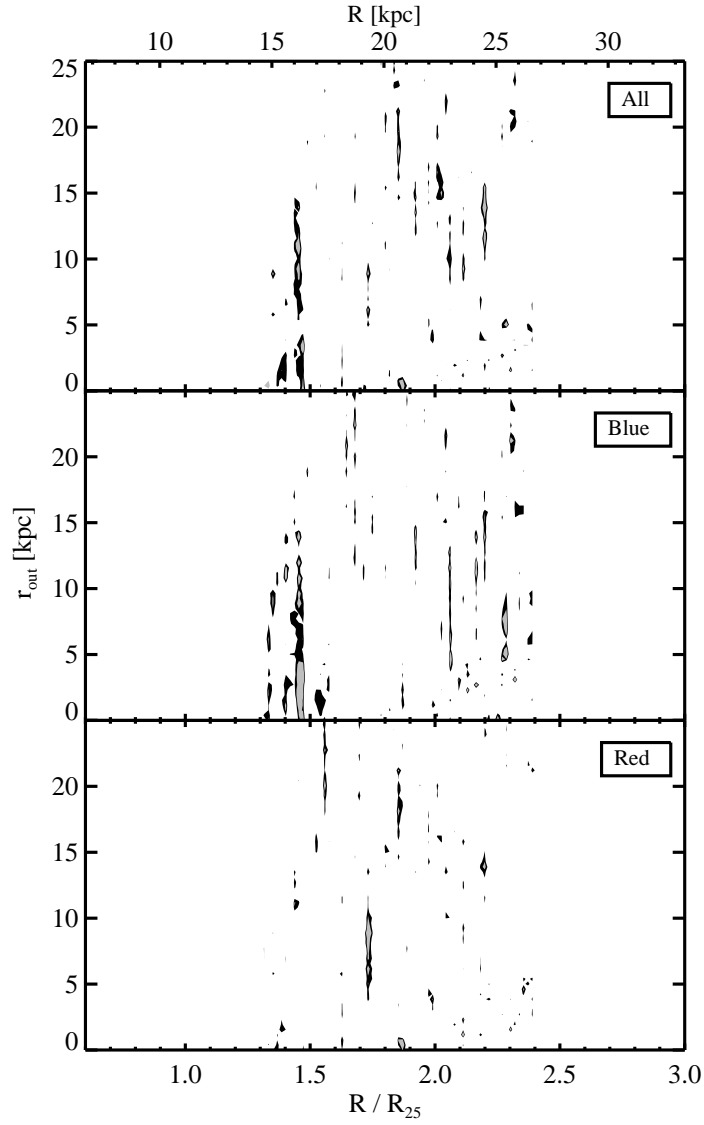


Figure 2.10 Restricted three-point cross-correlation maps of LBT-detected knots and H I pixels with $N(\text{HI}) > 6.9 \times 10^{19} \text{ cm}^{-2}$. The top panel is from all sources with $-1.7 < U - V < 0.7$ and $18 < V < 27.5$, while the lower panels result from splitting the sample into blue and red components on either side of $U - V = -0.2$ (middle and bottom panel, respectively). Only data between $1.3 - 2.4 R_{25}$ was used. Black and grey show areas where signal is detected at $> 95\%$ and $> 99\%$ significance, respectively.

NGC 3104, a member of the galaxy association mentioned above. Therefore, although NGC 3184 does not appear to be interacting or have had significant interactions recently (given the lack of obvious morphological disturbance), we cannot discount the possibility that previous minor perturbations have influenced the buildup of this stellar outer disk.

However, we add a final word of caution to the suggestion that interactions are required for triggering visible outer disks. Christlein & Zaritsky (2008) detect extended $H\alpha$ emission from a sample of nearby (edge-on) galaxies selected against nearby companions and any morphological disturbances. These results suggest that visible outer disks are a natural result of disk galaxy evolution and do not require triggering by external sources (although external disturbances may still raise the level of star formation above the nominal value).

2.9 Summary and Discussion

We present initial results from our optical extended disk imaging study using the LBC on the LBT. We will present a similar analysis of our full sample (seven galaxies) in a subsequent paper. Here we focus on the large, face-on galaxy NGC 3184. We find that the outer disk is populated by marginally-resolved cluster-like objects (or ‘knots’) with masses $\sim 10^2 - 10^4 M_\odot$ and ages up to ~ 1 Gyr. The cluster masses and ages are not well-constrained with the available optical data and are meant as illustrative estimates only. Background-subtracted Hess diagrams show statistically significant numbers of these cluster-like objects extending to $\sim 1.4R_{25}$, with the redder knots extending to the largest radii ($\sim 1.4 - 1.5R_{25}$). We construct restricted three-point correlation maps to measure the self-clustering of the detected knots and find significant correlation signal extending to $\sim 1.5R_{25}$. The effective surface brightness of the outer disk clus-

ter populations we detect ranges from $30 - 32 \text{ mag arcsec}^{-2}$ in V , depending on the method and radii used for the estimate (the restricted three-point correlation map approach or background-subtracted Hess diagrams, respectively). We also present a knot-knot correlation map from GALEX-detected objects near NGC 3184 and find significant correlation near $\sim 1.2R_{25}$, although those data are currently very limited (the publically-available GALEX imaging of this field is very shallow and does not provide a large number of knots to use in the correlation analysis). We compare the 21cm H I gas disk extent to that of the knots and find that the correlated clusters extend nearly to the DLA threshold of H I gas ($2 \times 10^{20} \text{ cm}^{-2}$; $1.62R_{25}$) and are well contained within the 3σ extent of the H I gas ($6.9 \times 10^{19} \text{ cm}^{-2}$; $1.80R_{25}$). The cross-correlation between optical knots and H I pixels above the 3σ threshold suggests that the blue knots are correlated with H I spiral structure to $\sim 1.45R_{25}$, and that the red knots may be correlated with the outer fringes of the H I disk to $\sim 1.73R_{25}$. The radii at which we detect significant cross-correlation signal correspond to where we observe obvious spiral structure in the HI map, as well as a (less-obvious) enhancement of cluster aggregates tracing the spiral pattern. We therefore expect that these structures are responsible for the positive signal. Incorporating the H I data further increases our ability to detect knots associated with the disk, to the largest radii. The cluster-like objects appear to extend to the outermost reaches of the gas disk.

Assuming that knots in NGC 3184 formed in clustered aggregates of similar scales over the past few Gyr, the fact that we see continued clumpiness in the red panel of Figure 2.5 suggests that at least some of the original aggregates survive as a group, even after hundreds of Myr. The aggregates and knots that do dissolve, perhaps via stellar evaporation caused by encounters with neighboring clusters or giant molecular clouds (albeit on longer timescales and with lower ef-

iciency than expected in the inner disk), may distribute many of their stars into the diffuse, low surface brightness component visible in the images (mainly as faint, extended spiral structure). This low surface brightness component is better seen in the V -band data, as expected by the numbers of red to blue clusters, the assumption that the larger ages of red sources means they have had more time to evaporate stars into a diffuse component, and simply because the V image is deeper than the U image.

The restricted three-point correlation results illustrate how even a galaxy like NGC 3184, which appears to lack any obvious young outer disk component in both our deep exposures and the available GALEX data (albeit limited), still hosts cluster populations in its outer reaches. This suggests that the Zaritsky & Christlein (2007) and Thilker et al. (2007) estimates of the local extended UV disk fraction ($\sim 30\%$) may lie far below the local *optical* extended disk fraction.

Whether the stellar populations in the outer disk were born in situ or scattered from smaller radii is still undetermined. Roškar et al. (2008a,b) have convincingly demonstrated that stars will, over time, be scattered to larger radii and populate an outer disk of characteristics consistent with those measured from unresolved stellar populations (e.g. Pohlen et al. , 2002). However, various features of our knot population suggest that these were born in situ. First, we find knot-knot clustering out to interknot separations of 1 kpc. A scattering model would presumably populate the outer disks in a much more stochastic manner. Scattering velocities would have to be coordinated to better than 10% to maintain coherence over 1 kpc while scattering objects 10 kpc from their birthsite. Second, we find correlation between the knots and the H I. The H I is clearly in a stable rotating disk and could not be scattered from smaller radii. The correlations between the two suggest a causal relationship.

A recent simulation by Bush et al. (2008) presents an in situ formation picture for the knots, showing how local overdensities of gas in an outer disk can lead to star formation closely resembling the UV knots observed by GALEX. Furthermore, Christlein & Zaritsky (2008) detect very regular outer disk rotation curves (i.e. flat, low velocity dispersion) from deep $H\alpha$ spectroscopy of many nearby edge-on disks, suggesting that outer disks are merely less-populated extensions of their inner counterparts (and therefore that in situ cluster formation should be expected). Given the successes of the Roškar et al. (2008a,b) studies, as well as that of Bush et al. (2008), we expect both radial migration and in situ formation to significantly influence the populations of outer disks. We encourage the modelers to identify key signatures of each mechanism that can be used to further discriminate between these possibilities. With the identification of large populations of knots, correlation statistics appears to be a promising avenue for such efforts.

CHAPTER 3

STAR CLUSTER POPULATIONS IN THE OUTER DISKS OF NEARBY GALAXIES

3.1 Chapter Abstract

We present a Large Binocular Telescope (LBT) imaging study that characterizes the star cluster component of nearby galaxy outer disks (beyond the optical radius R_{25}). We expand on the pilot project of Herbert-Fort et al. (2009), who studied the outer disk of NGC 3184, and present deep (~ 27.5 mag V -band point-source limiting magnitude) U - and V -band imaging of six galaxies: IC 4182, NGC 3351, NGC 4736, NGC 4826, NGC 5474, and NGC 6503. The outer disk of each galaxy is populated with marginally-resolved ‘knots’ that resemble star clusters with masses $\sim 10^3 M_\odot$ and ages up to ~ 1 Gyr (the oldest we can detect given our U and V imaging). The knot component of these outer disks contributes an effective surface brightness of up to ~ 29 mag/sq. arcsec in V (typically ~ 31 mag/sq. arcsec). We find a statistically significant excess in the number of these knots to at least $2R_{25}$ in our combined sample and place a lower limit on the mean outer disk cluster formation rate of one $10^3 M_\odot$ cluster every ~ 2.5 Myr, or $\sim 0.004 M_\odot \text{ pc}^{-2} \text{ Gyr}^{-1}$. We measure the self-clustering of knots as a function of galactic radius and find significant signal, with the most distant self-clustering detection at $3.3R_{25}$ in IC 4182. Our LBT data, in combination with public GALEX and H I data, suggest that clusters reside outside of the current extent of the H I. Finally, we examine the cross-correlation between LBT knots and H I and detect knots correlated with H I structures to $\sim 2R_{25}$. Confirming the results of Herbert-Fort et al. (2009), we find that outer disks are well-populated, common, and long-lasting features of many nearby disk galaxies.

3.2 Chapter Introduction

The outer disks of nearby galaxies have received much recent attention, both theoretical (e.g. Bush et al. , 2008; Roškar et al. , 2008a,b; Kazantzidis et al. , 2009) and observational (e.g. Thilker et al. , 2007; Gil de Paz et al. , 2007; Zaritsky & Christlein , 2007; Christlein & Zaritsky , 2008; Herbert-Fort et al. , 2009; Trujillo et al. , 2009; Herrmann et al. , 2009; Werk et al. , 2010). The GALEX mission (Martin et al. , 2005; Thilker et al. , 2007) was largely responsible for this revival of interest in outer disks, providing a much ‘cleaner’ view of star formation at the edges of galaxies. GALEX UV imaging provides the stark color contrast required to differentiate young, blue clusters from the sea of redder background objects. Because this contrast is much lower in broadband optical imaging, previous studies of outer disks often relied on narrowband $H\alpha$ imaging to robustly detect outer disk clusters (e.g. Ferguson et al. , 1998; Werk et al. , 2010). The limitation of such an approach is that clusters with $H\alpha$ are all young, less than ~ 10 Myr old, so the number of outer disk cluster detections is small. GALEX detects clusters that are up to ~ 500 Myr old and so provides much larger samples of outer disk knots around galaxies.

As useful as GALEX was for detecting outer disk clusters, this paper focuses instead on broadband optical imaging of outer disks for several reasons. First, the spatial resolution of GALEX imaging ($\sim 5''$ FWHM) is roughly six times larger than what we typically achieve from the ground using optical telescopes. GALEX knots are typically blends of multiple clusters (Gil de Paz et al. , 2005), whereas we detect knots resembling individual star clusters in our optical images. Second, the cluster mass limit we reach is $10\times$ lower than that of GALEX. Third, optical imaging probes older clusters, extending the baseline over which the phenomenon can be studied and again increasing the sample size. The gen-

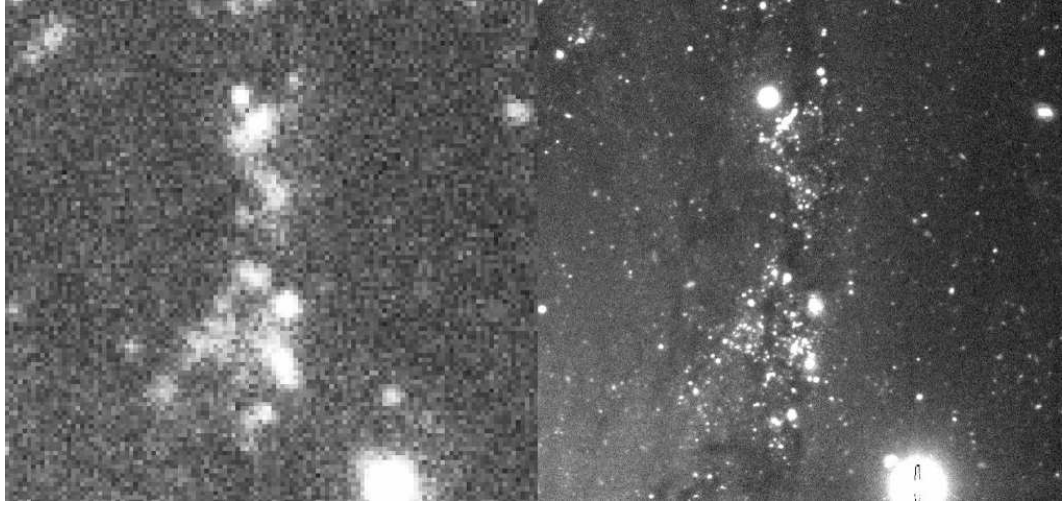


Figure 3.1 Comparison of GALEX (left) and LBT imaging (right) of a region around NGC 4736.

eral superiority of the data can be seen in Figure 3.1. Therefore, if we can overcome the increased difficulty in differentiating between sources and background, high-quality ground-based data will provide a much larger number of knots, and potentially a larger sample of galaxies with such data, for any statistical analysis of outer disk properties.

Herbert-Fort et al. (2009) focused on the outer disk of NGC 3184. We statistically differentiated clusters from the background in two ways: (1) using color-magnitude diagrams (CMDs) to make background-subtracted Hess diagrams as a function of galactic radius, and (2) using the self-clustering of knots to enhance the contrast relative to the background. We now apply these methods to our larger sample of galaxies.

We present the results of a statistical study of nearby (< 15 Mpc) outer disks, using the 8.4m Large Binocular Telescope (LBT, Mt. Graham, Arizona; Hill et al. , 2006) and wide-field, prime-focus Large Binocular Cameras (LBC; Ragazzoni et al. , 2006; Giallongo et al. , 2008). We describe our data reduction, develop analy-

sis tools, and apply these to deep V -band and U -band (hereafter V and U) imaging data of six galaxies (detailed in the following section). We demonstrate how two separate statistical methods enable us to trace outer disk cluster-like objects to large radii. In §3.3 we describe our observations, data reductions and source detections. In §3.4 we present CMDs of candidate outer disk sources, quantify the range of cluster properties consistent with the observed candidate knots, and present an estimate of disk knot radial extents. In §3.5 we present results from our restricted three-point correlation analysis of LBT knots, a similar analysis of GALEX knots, and a cross-correlation analysis of LBT knots and the underlying H I disks. We first present our results from these three analyses and then discuss them together on a galaxy-by-galaxy basis. We summarize our results and our conclusions in §3.6.

3.3 Observations to Final Source Catalog

We present new observations of six galaxies (IC 4182, NGC 3351, NGC 4736, NGC 4826, NGC 5474, NGC 6503) with LBC-Blue on the LBT on the dates listed in Table 3.1. We chose these systems to provide a representative sample of nearby disk galaxies; they span a range of physical disk sizes (see Table 3.1), all are less than ~ 15 Mpc away, and most are seen at low inclination ($< 50^\circ$). The small distances and low inclinations allow us to measure the clustering of sources in the disk as a function of galactic radius. Our final galaxy mosaics are made from combining individual 164-second dithered exposures through the $U - Bessel$ and $V - Bessel$ filters (hereafter U and V), except for NGC 5474, for which we combine 33-second dithered exposures in U to avoid saturation from a bright star in the field. The typical seeing during our observations was $0''.8$ and never exceeded $\sim 1''.3$. IC 4182, NGC 4736, and NGC 5474 were observed under photometric conditions. Single

photometric exposures were obtained for NGC 3351, NGC 4826, and NGC 6503 on 2/8/08 (*U* & *V*), 4/20/07 (*U* & *V*), and 4/22/07 (*U*) & 4/7/08 (*V*), respectively, for photometric calibration. We observed six photometric Landolt standard star fields (Landolt, 1992) for flux calibration.

We follow the image processing described in Herbert-Fort et al. (2009). We use a set of Interactive Data Language (IDL¹) scripts created by our group to create ‘master bias’ frames that correct for global changes and the two-dimensional structure in the bias level across the CCDs. We correct for sensitivity variations on the CCDs by combining dithered, twilight-sky flat-field images that are normalized by the four-chip median value of each bias-corrected flat field exposure. We then median-combine the normalized flats to create ‘master flat’ frames and finally divide the bias-corrected science frames by the master flats to complete the processing of the individual science exposures.

Next, we sample the background of each exposure in twenty regions around the edges of the detector array. The background is estimated using the IDL routine MMM², which uses an iterative process to determine the mode of the sky values after rejecting outlying pixels (caused by stars, saturation, cosmic rays, hot pixels and bad columns). This is done for each four-chip exposure and the minimum estimated sky from the various regions is subtracted from each corresponding chip. We then create a weightmap for every four-chip exposure to mask bad columns (detected by eye in the master flats), hot pixels and cosmic rays (detected using the IDL routine REJECT_CR, which finds features sharper than the PSF) when creating the mosaic images.

To combine the individual frames into final exposures we first use SExtractor

¹Developed by Research Systems, Inc. and owned by ITT; <http://www.ittvis.com/ProductServices/IDL.aspx>

²Part of the Goddard IDL library, maintained by W. Landsman; <http://idlastro.gsfc.nasa.gov/>

Table 3.1. Sample Galaxies

Name	i	PA	D	R25	U_{date}	U_{exp}	V_{date}	V_{exp}	V_{lim}	V_{apcorr}	$\sigma_{V_{apcorr}}$	Ref.
IC 4182	23	90	4.7	4.1	5/11/07	1640	5/11/07	1640	27	-0.11	0.05	1
NGC 3351	40	13	10.1	10.8	3/21/07	1640	3/21/07	1640	27	-0.15	0.05	4,5,6,7
NGC 4736	8	122	4.7	7.6	2/21/07	1640	2/21/07	1476	27.5	-0.13	0.03	2,3
NGC 4826	61	115	7.5	10.2	2/10/08	1476	4/24/07	1476	26	-0.69	0.04	1,8,9
NGC 5474	26	132	7.2	5.0	5/10/07	328	5/10/07	1804	26	-0.26	0.01	1,10
NGC 6503	74	121	5.3	4.5	4/23/07	1312	4/11,23/07	3280	26	-0.46	0.01	1,11,12

Units: inclination and position angle in degrees, distance in Mpc, R25 in kpc, U_{exp} and V_{exp} in seconds, V_{lim} , V_{apcorr} and $\sigma_{V_{apcorr}}$ in (Vega) magnitudes.

References. — 1: Karachentsev et al. (2004); 2: Karachentsev (2005); 3: Trujillo et al. (2009); 4: Graham et al. (1997); 5: Rubin et al. (1975); 6: Buta (1988); 7: Swartz et al. (2006); 8: Tonry et al. (2001); 9: Nilson et al. (1973); 10: Rownd et al. (1994); 11: Makarova (1999); 12: Begeman et al. (1987)

(Bertin & Arnouts , 1996) to create a source catalog for every exposure so that SCAMP³ (Bertin , 2006) can correct for optical distortions in LBC-Blue by solving the astrometry of the dithered exposures and creating smooth distortion maps for use by SWarp⁴. Where the SDSS fifth data release (DR5; Adelman-McCarthy et al. , 2007) did not cover the science field we use the USNO-B catalog (Monet et al. , 2003) as the reference. We use SWarp to mean-combine the spatially-aligned frames after accounting for the bad pixel maps. Our final mosaic images are on a $\sim 0''.22 \text{ pixel}^{-1}$ spatial scale and have their photometry normalized to a fixed counts $\text{arcsec}^{-2} \text{ second}^{-1}$ standard. The mosaics are flat to 0.5 – 1% and have total integration times of ~ 25 minutes in the deepest areas (see Table 3.1).

We build aperture photometry catalogs using SExtractor, with source detection and aperture placement based on the deeper *V*-band mosaic. We select sources by identifying groups of five or more pixels each with flux $> 1\sigma$ above the background (so typical ‘detections’ are actually $> 3\sigma$, because $[< 0.3173]^{[\geq 5]} < 0.0032$). Because we detect the integrated light from members of stellar groups, the ‘knots’, any photometric algorithm that requires a uniform object shape for extraction is not optimal for this work. See Herbert-Fort et al. (2009) for all of the chosen SExtractor parameters. We detect nearly all visually-discernable objects beyond the optical radius R_{25} , though our catalog becomes noticeably incomplete inside $\sim 0.8R_{25}$. SExtractor has difficulty detecting sources over the bright, extended emission of the inner disk.

We use processed photometric exposures of Landolt standard star fields, taken on the same night as our individual photometric exposures of the galaxies, to calibrate our photometry. We account for an airmass and a color term when flux-calibrating the processed photometric exposures on the standard Vega system.

³Version 1.4.0; <http://terapix.iap.fr/soft/scamp>

⁴Version 2.17.1; <http://terapix.iap.fr/soft/swarp>

Finally, we bootstrap the photometry of the photometric exposures to the deep mosaics using ~ 10 stars common to both.

Colors and magnitudes are measured using circular apertures. Colors quoted throughout are from fixed four-pixel-diameter apertures ($0''.9$, just larger than the typical $0''.8$ FWHM of detected sources), while V magnitudes are from 10-pixel-diameter apertures ($2''.24$) and aperture-corrected using stellar curves-of-growth by the values listed in Table 3.1. Aperture corrections were calculated from ~ 8 isolated, unsaturated stars measured in 15 apertures spanning $2 - 50$ pixels in diameter (or $0''.4 - 1''.2$). We set SExtractor to mask and correct neighbors that contaminate.

The night of April 24, 2007 was very windy and resulted in poorer seeing than usual ($\sim 1''.3$) during our V exposures of NGC 4826. As a result, the $U - V$ colors of NGC 4826 sources appear to be artificially blue by ~ 0.5 mag. This color offset was estimated by eye from the CMDs presented in the next section, though this value also agrees with the large aperture correction in V listed in Table 3.1, once you account for the ‘typical’ $V_{apcorr} \sim 0.15$ mag in good seeing and recognize that the V apertures (for which the aperture corrections are relevant) are larger than those used to measure $U - V$ (not aperture-corrected), so the color correction could be even larger. This color-offset effect is also just noticeable in the color-magnitude diagrams of NGC 5474 and NGC 6503 presented in the following section (these galaxies show the next highest V_{apcorr} values). In general however our measurement error is larger than this offset; our photometry is still consistent with that from SDSS and USNO-B (see below). Furthermore, this effect will not significantly affect our results, because these systems have the lowest number of outer disk sources detected and because NGC 4826 (the galaxy showing the strongest effect) and NGC 6503 are later dropped from the analysis

because of their high inclinations ($i = 61^\circ$ and 74° , respectively).

To finish building our final catalog, we only retain sources whose random $U - V$ color error is < 0.5 mag (magnitude errors are provided by SExtractor and propagated in the standard manner). We also manually mask regions around bright stars (those showing diffraction spikes and scattered light halos) because our detection algorithm has trouble detecting sources in their vicinity, and leads to artificially low counts and artificial signal in our correlation maps. Only NGC 5474 had no masking applied because our very shallow U mosaic prevents us from detecting large numbers of sources. Table 3.2 lists the number of sources retained between $1.0 - 1.5R_{25}$, $1.5 - 2.0R_{25}$, and $2.0 - 2.5R_{25}$ in our final catalogs (the outer limit, $2.5R_{25}$, is somewhat arbitrary, loosely based on previous outer disk studies, e.g. Zaritsky & Christlein 2007). Table 3.2 also lists the total area considered in each annulus after masking (to make comparisons between annuli meaningful). We check our photometry by comparing the U and V apparent magnitudes of ten well-isolated objects across the fields with those provided by SDSS-DR5 (when available, otherwise USNO-B), converted from u , g , and r to either U or V using the transformations of Jester et al. (2005). Aside from the systematic offset in our V magnitudes from NGC 4826, our results are consistent with the transformed SDSS photometry to within the transformed SDSS and LBT photometric errors.

3.4 Cluster Populations Surrounding the Galaxies

In Figures 3.2 - 3.7 we present the CMDs of sources between $1.0 - 1.5R_{25}$ from the six galaxies we observed. We have added Starburst99 (Leitherer et al. , 1999; Vazquez & Leitherer , 2005) tracks showing models of fixed mass, solar metallicity star clusters for ages 1 Myr to 3 Gyr. The upper and lower tracks represent

Table 3.2. Sources in CMDs

Name	annulus	area	N_{CMD}	N_{Hess}	frac.	μ_{eff}
IC 4182	1.0 – 1.5	30.95	1950	248	13	29.62
IC 4182	1.5 – 2.0	41.66	2244	-48	N/A	30.44
IC 4182	2.0 – 2.5	43.91	2408	-7	N/A	29.98
NGC 3351	1.0 – 1.5	40.22	2037	448	22	> 32.44
NGC 3351	1.5 – 2.0	38.22	1593	83	5	> 34.91
NGC 3351	2.0 – 2.5	37.52	1554	72	5	> 31.12
NGC 4736	1.0 – 1.5	85.38	8517	2774	33	29.46
NGC 4736	1.5 – 2.0	104.88	7570	516	7	30.43
NGC 4736	2.0 – 2.4	83.93	6135	489	8	> 30.99
NGC 4826	1.0 – 1.5	40.42	1445	-33	N/A	30.00
NGC 4826	1.5 – 2.0	52.90	1964	30	2	33.11
NGC 4826	2.0 – 2.5	72.15	2670	33	1	31.34
NGC 5474	1.0 – 1.5	19.96	699	427	61	28.85
NGC 5474	1.5 – 2.0	27.95	433	52	12	> 33.57
NGC 5474	2.0 – 2.5	35.93	465	-25	N/A	32.14
NGC 6503	1.0 – 1.5	8.69	622	369	59	28.36
NGC 6503	1.5 – 2.0	9.94	554	265	48	28.94
NGC 6503	2.0 – 2.5	13.63	511	114	22	29.75

Units: annulus in R_{25} , unmasked area used in sq. arcmin, frac. as a percentage, and μ_{eff} in mag arcsec⁻². frac. is N/A when N_{Hess} is negative (no excess of disk sources over the background). μ_{eff} is a lower limit when the total flux in the Hess diagram is negative (typically when oversubtraction of bright sources outweighs positive flux contribution from fainter sources).

$10^4 M_{\odot}$ and $10^2 M_{\odot}$ clusters, scaled down from a simulated $10^6 M_{\odot}$ cluster that adequately samples the Kroupa IMF. Because we ignore the stochastic sampling of the IMF at low cluster masses (Cerviño & Luridiana , 2004; Fagiolini et al. , 2007) comparisons with the scaled model tracks can lead to underestimates of cluster masses and overestimates of their ages. These tracks are only meant to provide a general impression of the cluster masses and ages consistent with the sources in our sample.

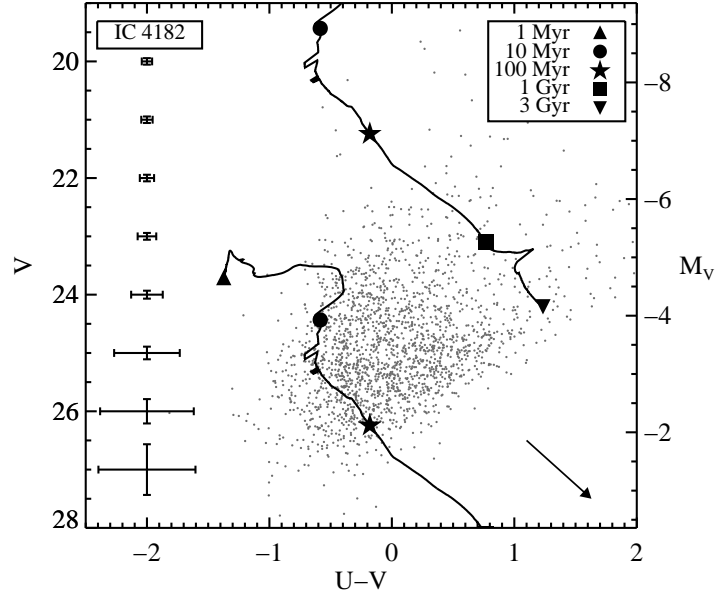


Figure 3.2 CMD of *all* sources (including background sources) between $1.0 - 1.5R_{25}$ from our final catalog of IC 4182 (after masking areas around bright stars; see text), with median 1σ errors as a function of apparent magnitude shown on the left. A reddening vector corresponding to 1 magnitude of extinction in V , calculated using results from Rieke & Lebofsky (1985), is shown at lower right. The work of Alberts et al. (2011) suggests low extinction in outer disks ($E(B - V) < 0.3$, or smaller than the arrow shown). See the text for a description of the Starburst99 model tracks.

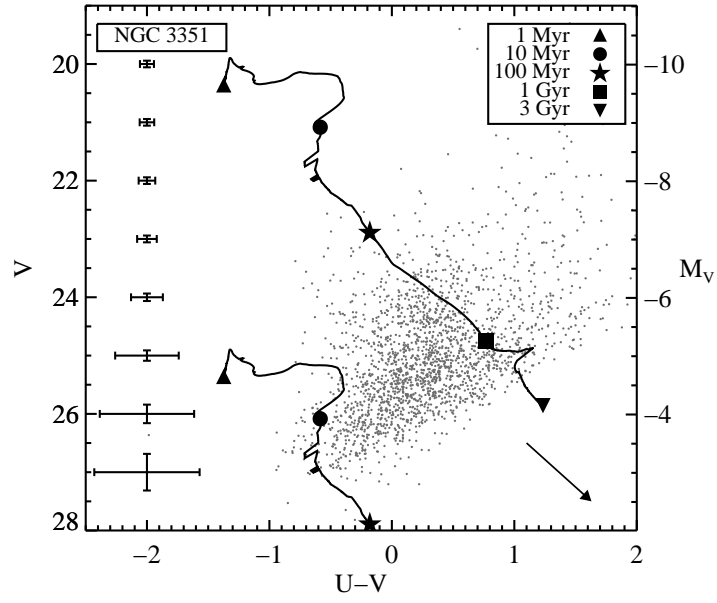


Figure 3.3 Same as Figure 3.2 but for NGC 3351.

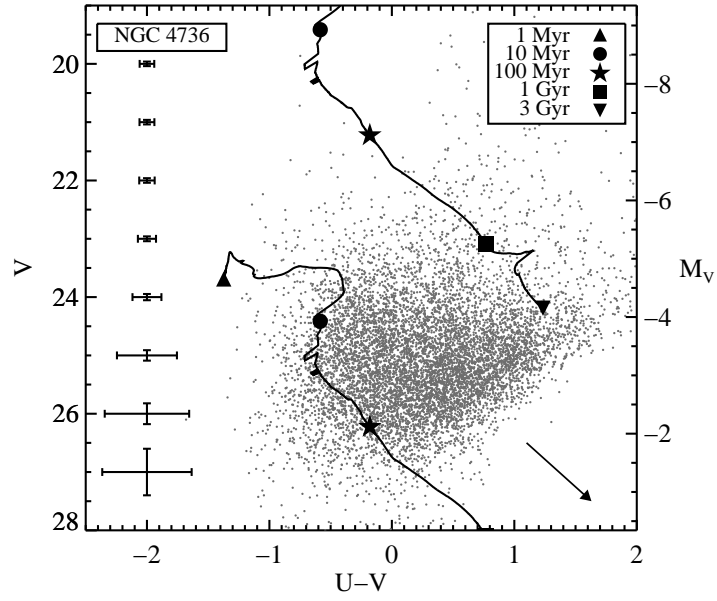


Figure 3.4 Same as Figure 3.2 but for NGC 4736 (M94).

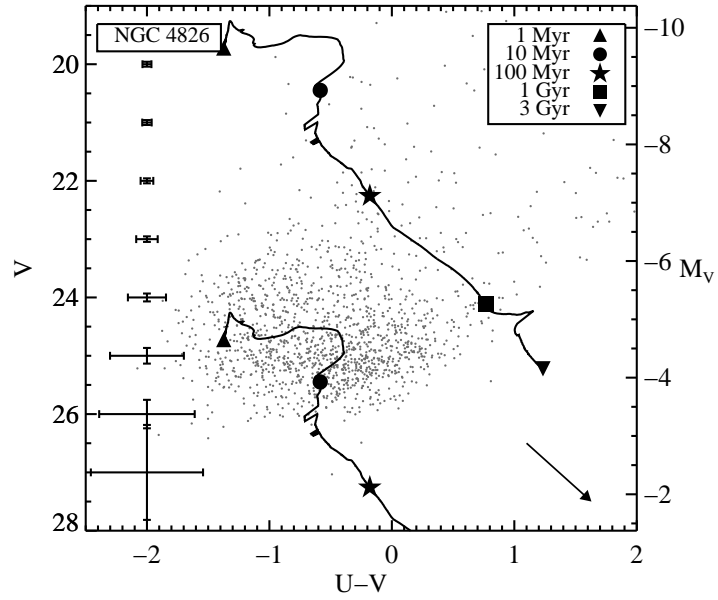


Figure 3.5 Same as Figure 3.2 but for NGC 4826. The V images suffered from poor seeing and resulted in $U - V$ colors being artificially blue by ~ 0.5 mag.

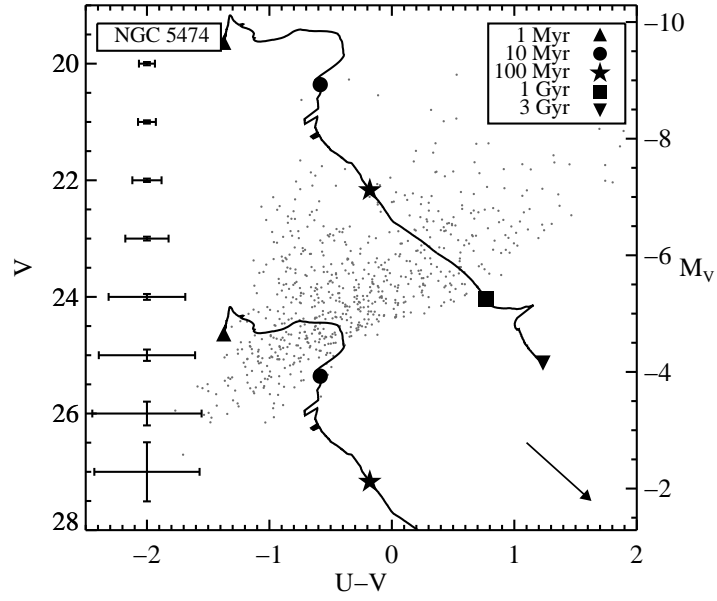


Figure 3.6 Same as Figure 3.2 but for NGC 5474. The U mosaic of NGC 5474 is the shallowest of the sample ($U_{exp} = 328$ seconds).

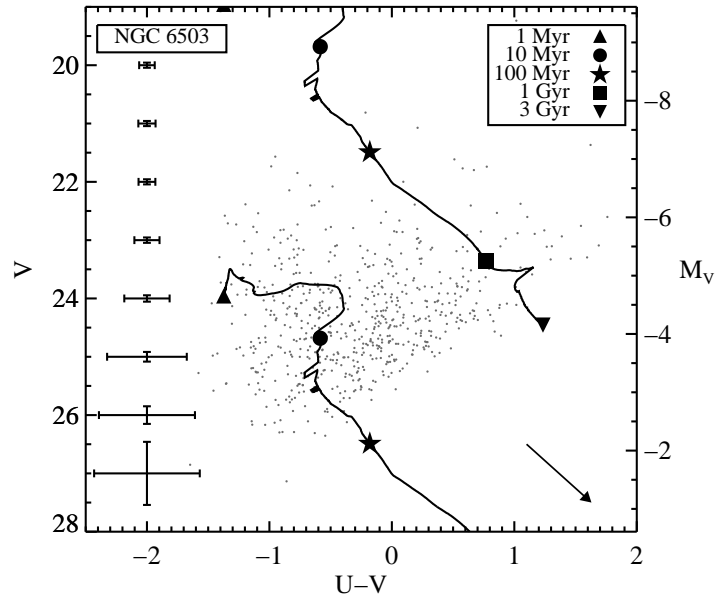


Figure 3.7 Same as Figure 3.2 but for NGC 6503.

We create background-subtracted Hess diagrams (Figures 3.8 - 3.13) in the same manner as Herbert-Fort et al. (2009), to statistically constrain the color and magnitude range of sources most likely associated with the galaxies. A Hess diagram plots the number of sources within chosen color-magnitude bins across a CMD (we use square bins of 0.2 mag here). We create both a ‘background’ Hess diagram from a region far outside of the galaxy and a ‘disk+background’ Hess diagram from the region of interest (say $1.0 - 1.5 R_{25}$), scale the counts in the ‘background’ Hess diagram by the relative areas of the two regions and subtract it from the ‘disk+background’ Hess diagram. The three-panel plots show the number of sources remaining between $1.0 - 1.5 R_{25}$ (left; dark regions are positive counts), $1.5 - 2.0 R_{25}$ (middle), and $2.0 - 2.5 R_{25}$ (right). Solid and dotted black contours outline signal lying above and below the background at a $> 90\%$ confidence level (CL), respectively, calculated using the low-count, Poisson single-sided upper and lower limits from Gehrels (1986); the dotted contours show any oversubtraction. Although the solid contours only surround Hess diagram pixels whose individual value is above the background at the 90% CL, groups of these pixels are considered true ‘detections’ of statistical excess at the $\gg 90\%$ CL. Overplotted is a $10^3 M_{\odot}$ Starburst99 model cluster, scaled down from a $10^6 M_{\odot}$ cluster as in Figure 3.2. See Table 3.2 for source counts and other details of the Hess diagrams, including our estimates of the effective surface brightness of the outer disk cluster components.

All six galaxies show excesses in their background-subtracted Hess diagrams between $1.0 - 1.5 R_{25}$, roughly tracing the $10^3 M_{\odot}$ cluster track. All galaxies except NGC 5474 show suggestive excess between $1.5 - 2.0 R_{25}$, though the noise is noticeably higher and it is difficult to form a strong opinion. We are skeptical of apparent excess between $2.0 - 2.5 R_{25}$ because those diagrams are so strongly

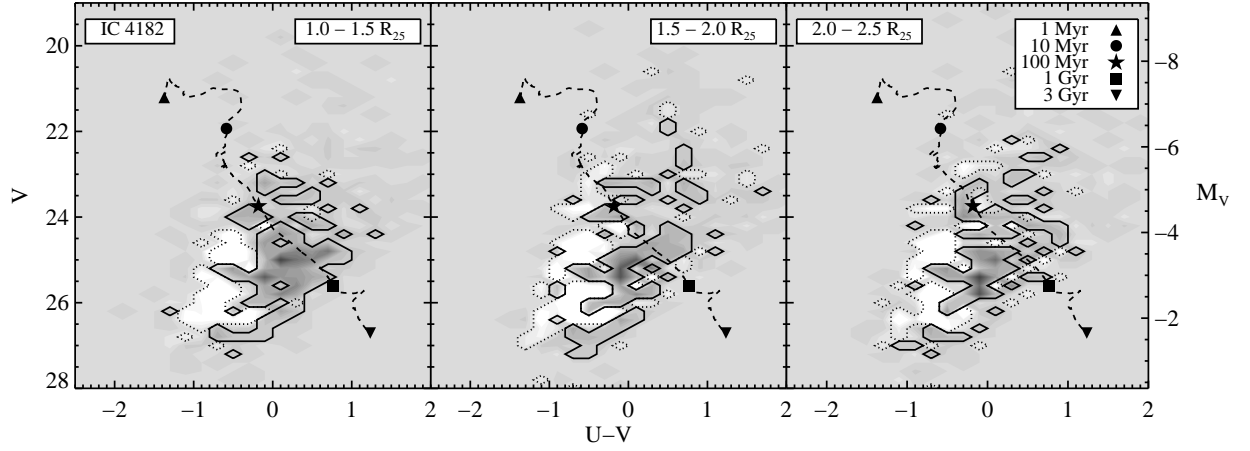


Figure 3.8 Background-subtracted Hess diagrams for IC 4182, made from sources between $1.0 - 1.5 R_{25}$ (left), $1.5 - 2.0 R_{25}$ (middle), and $2.0 - 2.5 R_{25}$ (right). Dark regions are positive counts. Solid and dotted black contours outline signal lying above and below the background at a $> 90\%$ confidence level (CL), respectively; the dotted contours show any oversubtraction. Overplotted is a $10^3 M_{\odot}$ Starburst99 model cluster, scaled down from a $10^6 M_{\odot}$ cluster.

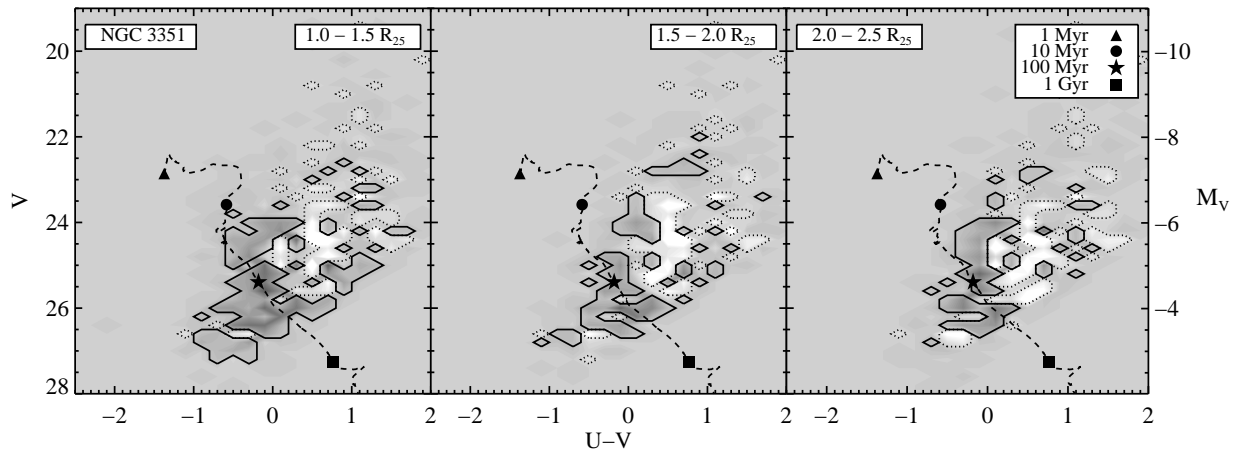


Figure 3.9 Same as Figure 3.8 but for NGC 3351.

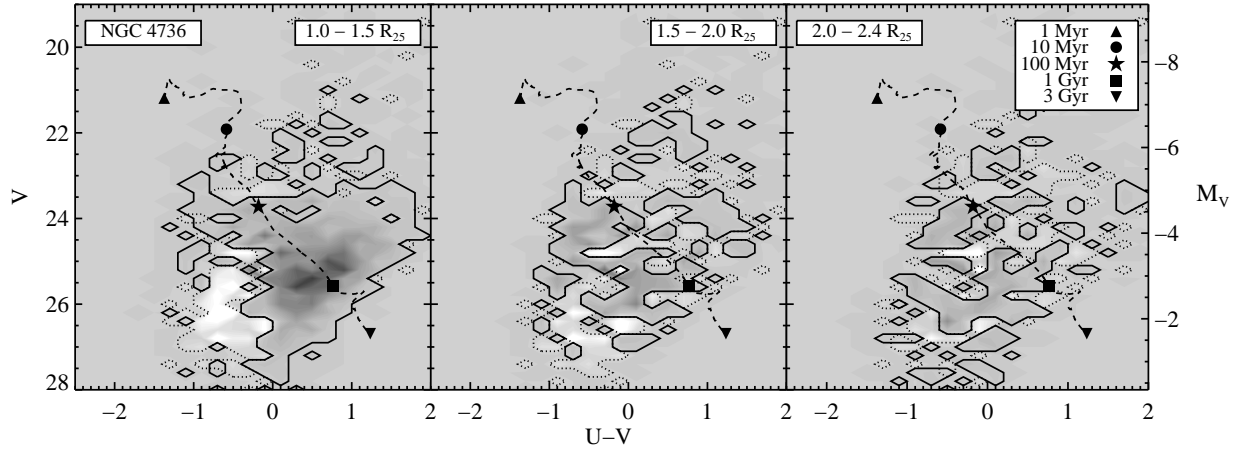


Figure 3.10 Same as Figure 3.8 but for NGC 4736.

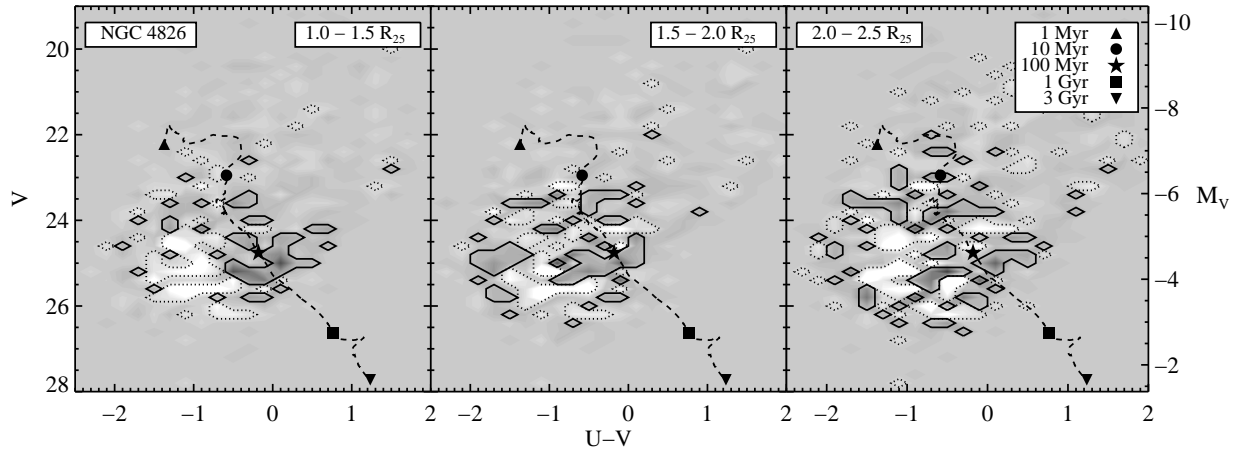


Figure 3.11 Same as Figure 3.8 but for NGC 4826.

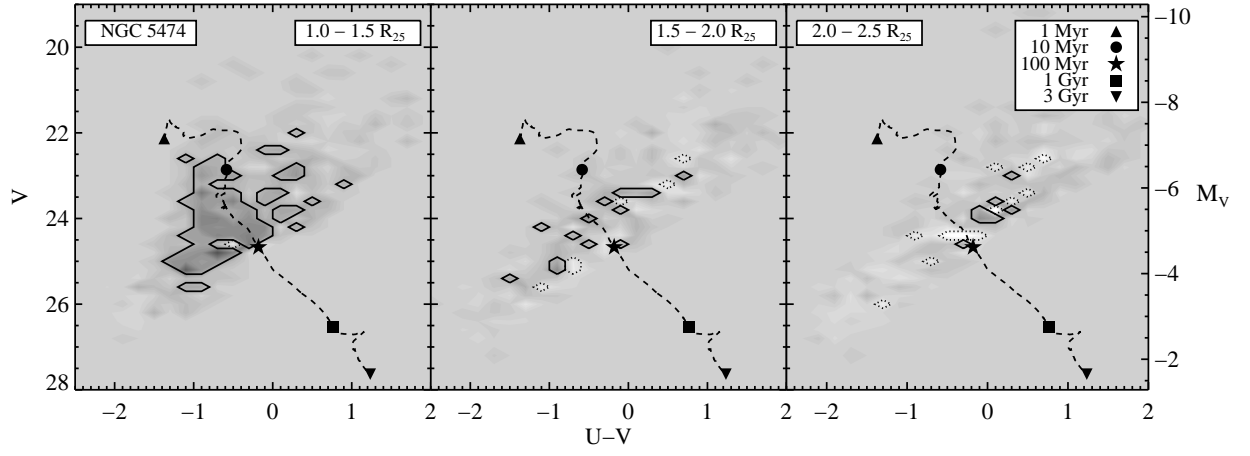


Figure 3.12 Same as Figure 3.8 but for NGC 5474.

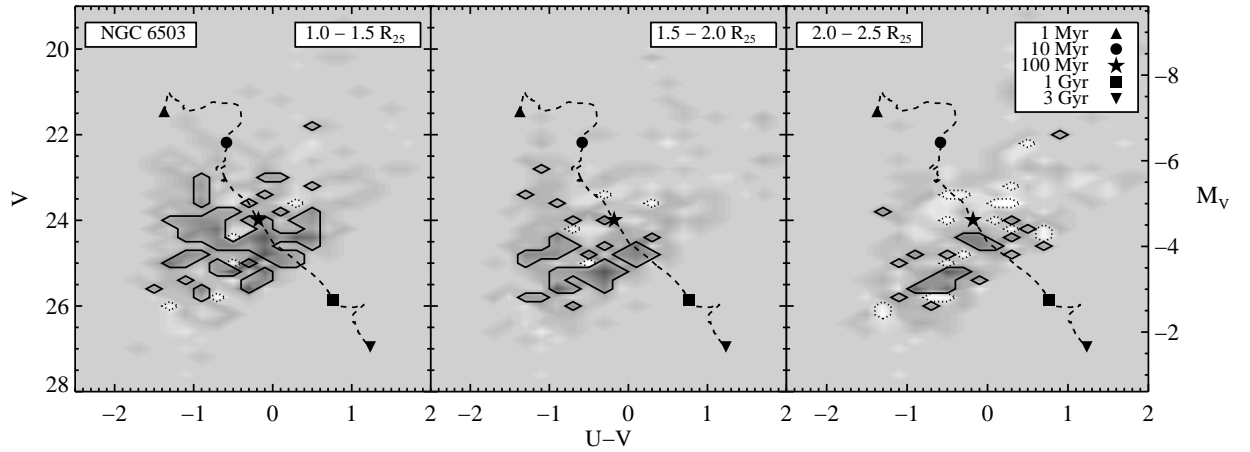


Figure 3.13 Same as Figure 3.8 but for NGC 6503.

peppered with oversubtraction (though perhaps some of the excess around NGC 4736 and NGC 6503 is real).

Figure 3.14 shows the average Hess diagrams of our galaxies, with sources combined at constant M_V , including excluding NGC 4736. NGC 4736 is the nearest and largest galaxy in our sample, and has a disproportionate number of detected sources. It was also more difficult to create a ‘background’ Hess diagram to subtract from the ‘disk+background’ diagram because of the lack of much background field in the mosaics of that galaxy. Therefore, because we are likely subtracting a small amount of this galaxy’s own signal, excesses seen around NGC 4736 are likely underestimates and oversubtractions are exaggerated. The average Hess diagrams show convincing excess out to at least $2.0 R_{25}$.

The majority of detected sources associated with the disk resemble star clusters of $10^3 M_\odot$. We therefore simulate a population of $10^3 M_\odot$ clusters forming at a constant rate for more than a Gyr and plot them in a figure similar to Figure 3.14, accounting for the uncertainties shown in the CMDs. Figure 3.15 shows the result of simulating these populations for four different cluster formation rates (see caption), using the CMD uncertainties from NGC 4736 (Figure 3.4), the galaxy with the most sources. This simulation assumes no cluster dissolution; if clusters are quickly lost then the formation rates could be much higher.

Comparing Figure 3.14 to Figure 3.15 shows that the data exclude cluster formation rates higher than one every $\sim 10^6$ years for clusters of mass $\geq 10^3 M_\odot$ (presuming no cluster dissolution), since no blue excess is detected for $M_V \lesssim -7$ mag. This rate is roughly what we calculate from the number of outer disk knots in the $1.0 - 1.5 R_{25}$ Hess diagrams (~ 400), the maximum age of a $10^3 M_\odot$ cluster in our diagrams (~ 1 Gyr), and a uniform rate of formation over the last Gyr; one cluster every ~ 2.5 Myr or $\sim 0.004 M_\odot \text{ pc}^{-2} \text{ Gyr}^{-1}$ (assuming $R_{25} = 5$ kpc).

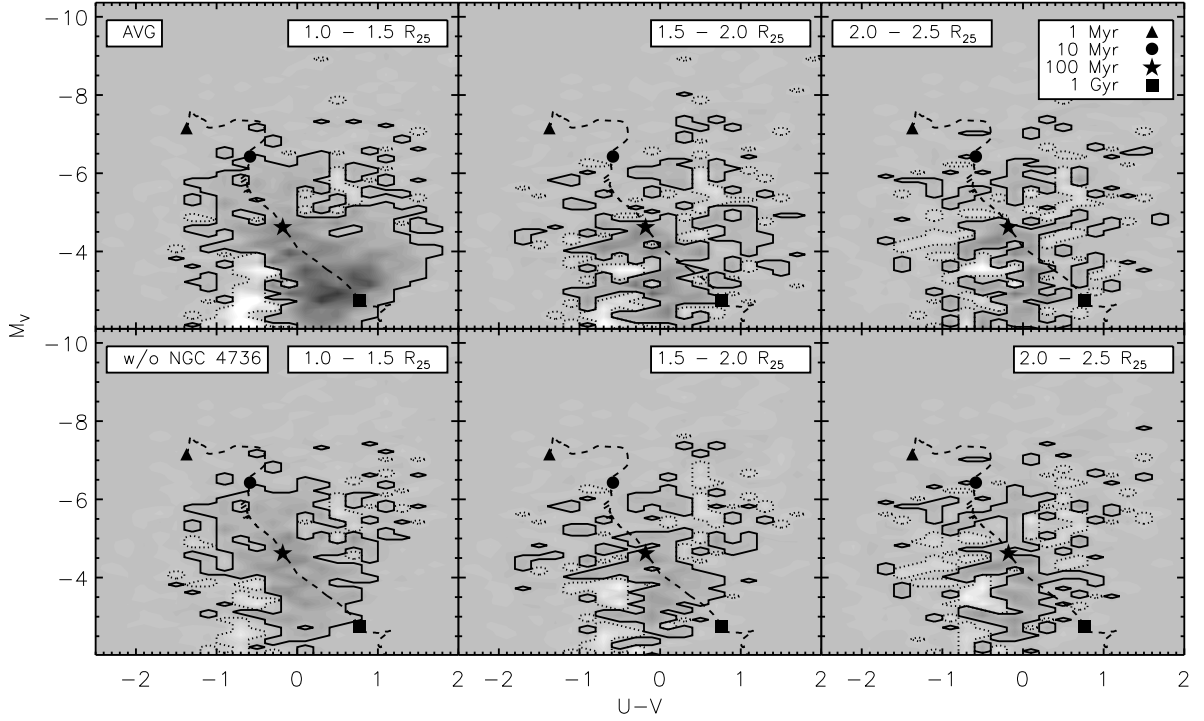


Figure 3.14 The average Hess diagram from all galaxies, with sources combined as a function of M_V , including and excluding NGC 4736 (top and bottom panels, respectively). The three radial ranges are the same as in the individual Hess diagrams ($1.0 - 1.5 R_{25}$, $1.5 - 2.0 R_{25}$, and $2.0 - 2.5 R_{25}$). Dark regions are positive counts. Solid and dotted black contours outline signal lying above and below the background at a $> 90\%$ confidence level (CL), respectively; the dotted contours show any oversubtraction. Overplotted is a $10^3 M_\odot$ Starburst99 model cluster, scaled down from a $10^6 M_\odot$ cluster. There is an excess out to at least $2 R_{25}$.

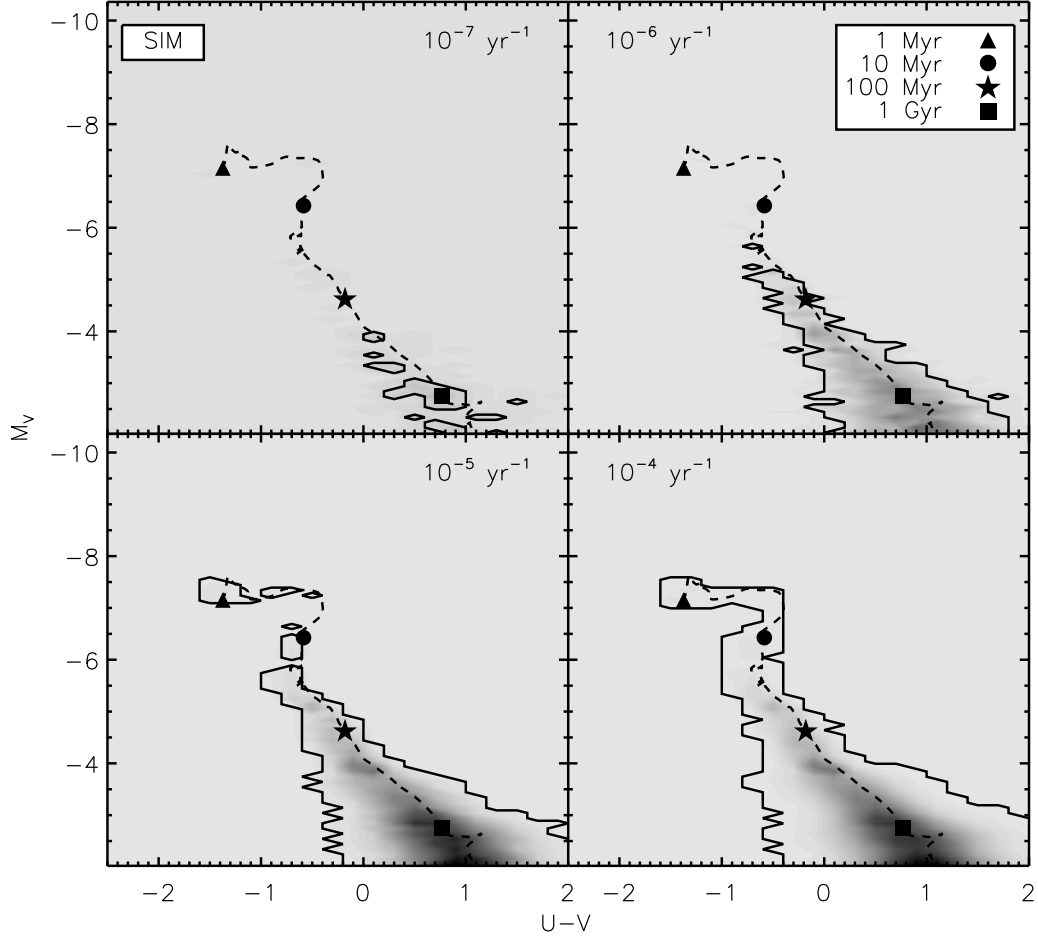


Figure 3.15 Simulated Hess diagrams made from a Starburst99 $10^3 M_{\odot}$ cluster track and the CMD uncertainties from NGC 4736 (Figure 3.4), for different cluster formation rates (top left: one every 10×10^6 yr; top right: one every 10^6 yr; bottom left: one every 10^5 yr; bottom right: one every 10^4). No background is considered when making the simulated diagrams.

Alternative estimates of the cluster formation rate exist. Ferguson et al. (1998) used deep $H\alpha$ imaging to measure the outer disk star formation rate densities of NGC 628, NGC 1058 and NGC 6946 to be between $\sim 0.01 - 0.05 M_{\odot} \text{ pc}^{-2} \text{ Gyr}^{-1}$. There are at least three potential explanations for our significantly ($10\times$) lower formation rate, all of which probably contribute to the difference: 1) the rate is highly stochastic and they happened to catch these galaxies in an elevated phase, 2) clusters disassociate and are therefore missing in our sample, and 3) the $H\alpha$ technique is sensitive to significantly lower mass clusters and therefore the majority of the mass is locked up in these lower mass clusters. Regarding the first possibility, we know from a comparative study of GALEX knots (Zaritsky & Christlein, 2007) that only a fraction of galaxies ($\sim 25\%$) show significant overdensities of bright blue knots. If all galaxies have an outer disk population, as we seem to find on the basis of optical imaging and spectroscopy (Christlein & Zaritsky, 2008), then the formation rate must be highly variable (with a duty cycle of about 25% for GALEX-detectable knots). Regarding the second option, we know that in certain environments where we have clusters spanning a range of ages, and can therefore do the study, that a small fraction of all star clusters survive (Chandar et al., 2006). Depending on the driver for cluster dissolution (mass loss vs. tidal stresses) the rate of cluster dissolution may be lower in the outer disks, but unlikely to be negligible. Davidge et al. (2011) observe star clusters in the outer disk of M33 to dissipate on time scales of 100 Myr. The clusters we detect that are 100 Myr old and older are likely the remnant cores of much larger clusters. Because outer disk clusters are typically of lower mass than their inner disk counterparts, it is possible that the outer disk clusters we detect are biased towards higher initial mass and so towards less common clusters, which could explain the large difference in cluster formation rates from our optical sam-

ple and those detected in $H\alpha$. Finally, regarding the third option, Davidge et al. (2011) calculates that most of the outer disk clusters in M33 form at lower masses ($50 - 250 M_{\odot}$) and so it may be the case that many of the $H\alpha$ -detected clusters are similar (simply because more of them are of lower mass, $< 10^3 M_{\odot}$). Though many of the young, low-mass ($\sim 100 M_{\odot}$) clusters may exist in our sample, overall we are biased towards the more massive, less common clusters that still lie above our detection limits. We should therefore expect to find a lower outer disk cluster formation rate from our LBT data than was found from $H\alpha$ observations.

If the outer disks in our sample have star formation rates of $4 \times 10^{-4} M_{\odot} \text{yr}^{-1}$, as suggested by our analysis (one $10^3 M_{\odot}$ cluster every 2.5 Myr), then they should have birthed $\sim 4 \times 10^6 M_{\odot}$ of stars over their lifetime (taken as 10^{10} yr). Many of these stars may no longer reside in the outer disk, however. Stellar evaporation from clusters and radial migration (Roškar et al. , 2008a) can transport stars far from their birth sites, including back into the inner disk.

3.5 Clustering of Knots in the Outer Disks

3.5.1 Self-clustering of LBT Knots

Following Herbert-Fort et al. (2009), we present restricted three-point correlation maps to trace the self-clustering of knots in the outer disks (see Figure 3.16 for a description of the radii used). This self-clustering provides an enhanced contrast relative to the background (which is angularly clustered differently). Instead of measuring the azimuthally-averaged two-point correlation function (e.g. Zaritsky & Christlein , 2007), here we use the self-clustering of knots to highlight regions with clusters and remove signal from large-scale background fluctuations. This technique only measures the extent of *clustered* knots; disk-bound stars and unclustered knots will evade detection. Null detections do not indicate a lack of

all knots.

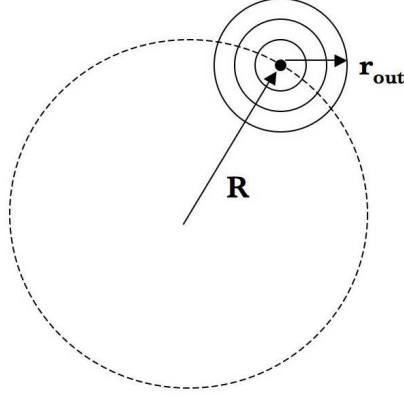


Figure 3.16 The radii defined for creating the restricted three-point correlation maps.

The restricted three-point correlation maps of our four low-inclination galaxies ($i < 50^\circ$) are presented in Figures 3.17 - 3.20. The high inclinations of NGC 4826 and NGC 6503 prevent us from making meaningful maps because deprojection introduces too much uncertainty. The top panels are constructed using all detections with $-1.7 < U - V < 0.7$ and $19 < V < 27.5$, while the lower panels result from splitting the samples into blue and red components on either side of $U - V = -0.2$ (middle and bottom panels, respectively). Black and gray show areas where signal is detected at the $> 95\%$ and $> 99\%$ significance level, respectively, as a function of both galactic radius R and intercluster radius r_{out} (Figure 3.16). The dotted lines show the radial extent of H I for $N(\text{HI}) > 2 \times 10^{20} \text{ cm}^{-2}$ (left, at $r_{out} = 0 \text{ kpc}$) and for $N(\text{HI})$ above the noise level of the integrated H I map (right, at $r_{out} = 0 \text{ kpc}$). The dotted lines are slanted to distinguish the $[R, r_{out}]$ regions that can and cannot be associated with the H I disk (to the left and right of either dotted line, respectively). The H I data and analysis are described later in the paper.

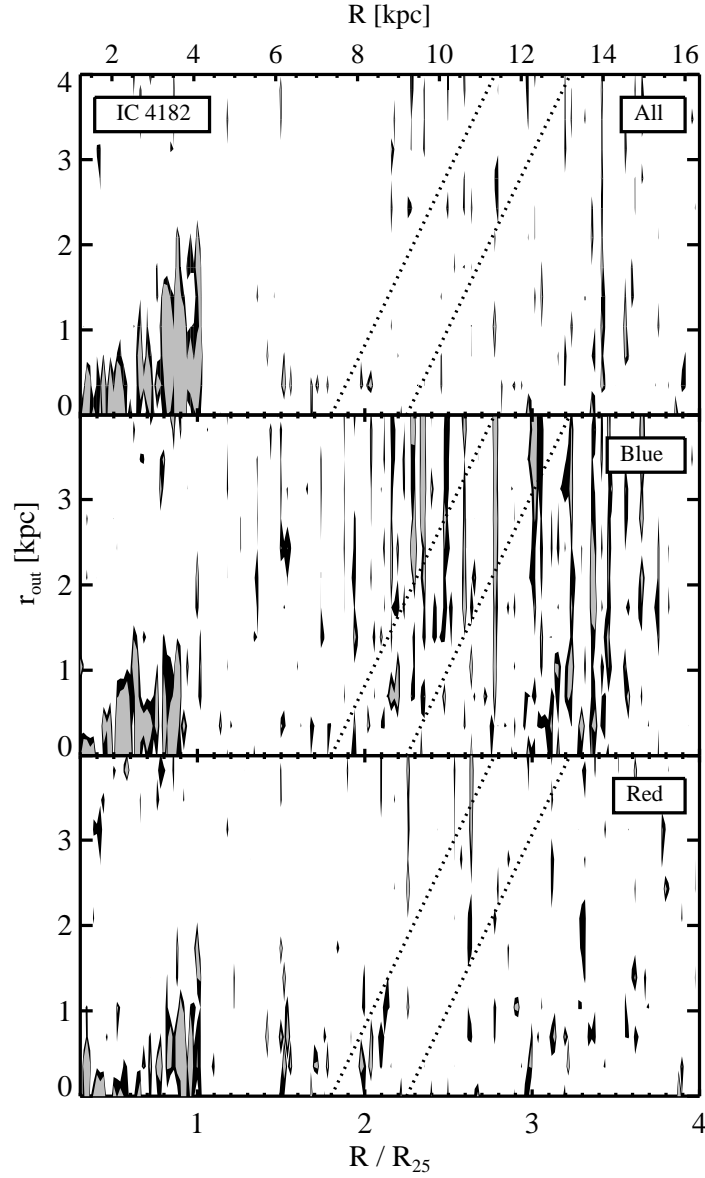


Figure 3.17 Restricted three-point correlation maps from sources in our (masked) final catalog of IC 4182. Black and gray show areas where signal is detected at the $> 95\%$ and $> 99\%$ significance level, respectively, as a function of both galactic radius R and intercluster radius r_{out} (Figure 3.16). The dotted lines show the radial extent of H I for $N(\text{HI}) > 2 \times 10^{20} \text{ cm}^{-2}$ (left, at $r_{out} = 0 \text{ kpc}$) and for $N(\text{HI})$ above the noise level of the integrated H I map (right, at $r_{out} = 0 \text{ kpc}$). The dotted lines are slanted to distinguish the $[R, r_{out}]$ regions that can and cannot be associated with the H I disk (to the left and right of either dotted line, respectively).

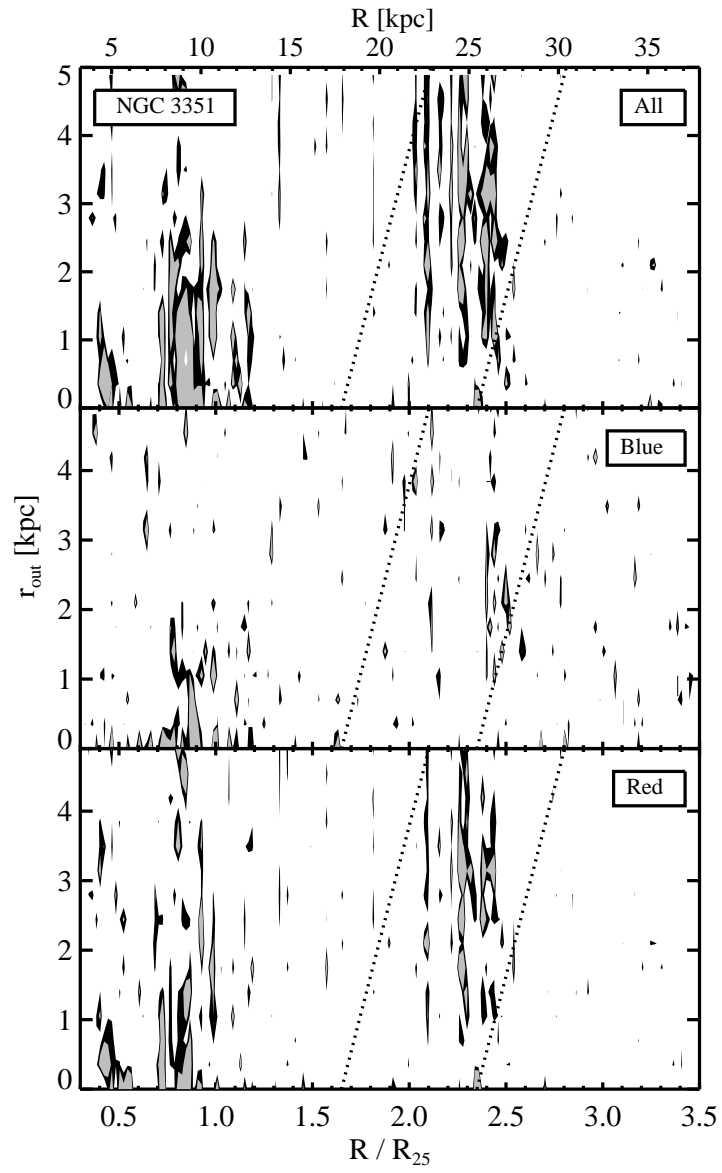


Figure 3.18 Same as Figure 3.17 but for NGC 3351.

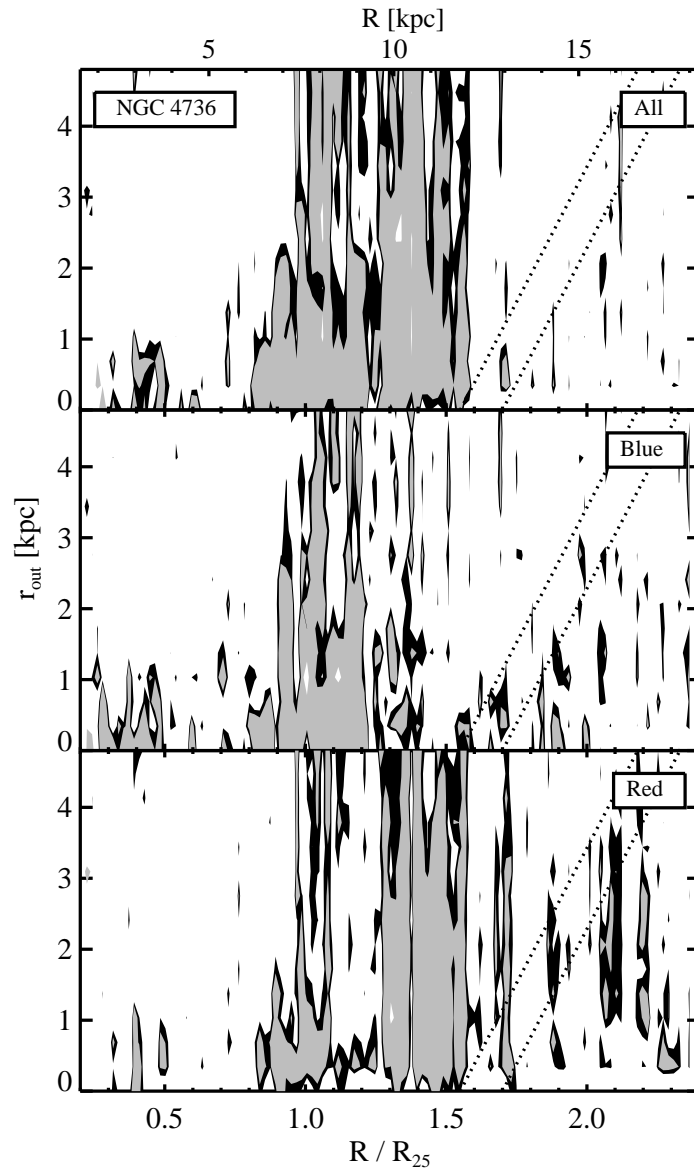


Figure 3.19 Same as Figure 3.17 but for NGC 4736.

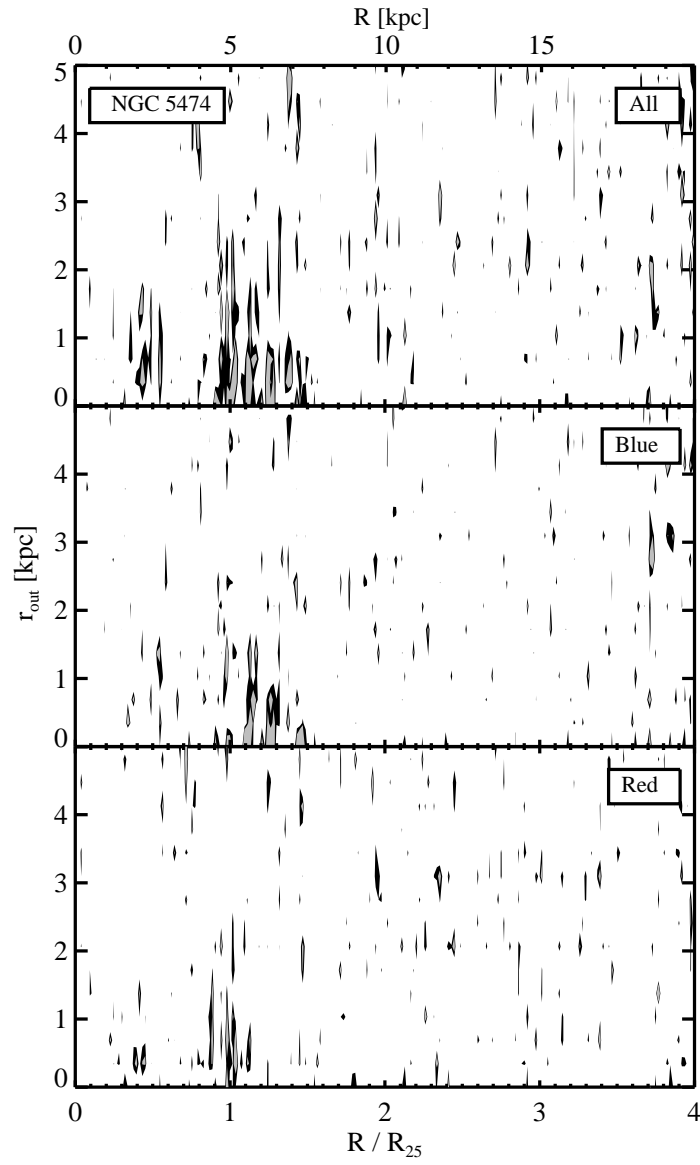


Figure 3.20 Same as Figure 3.17 but for NGC 5474.

Measuring the correlated knot extents directly from the three-point correlation maps is difficult because of the irregular nature of the signal. Rather than judge the significance of correlation peaks by eye, in Figures 3.21 - 3.24 we present the binomial probabilities that peaks in the three-point correlation maps are caused by random excursions. The probabilities are calculated as a function of radius, from signal extending to the max r_{out} plotted in the correlation maps (~ 5 kpc). We have rebinned pixels in the R direction to be of the same physical size as those in r_{out} direction, so that each new pixel is physically independent of its neighbors. The black and gray lines correspond to the black and gray signal in the correlation maps. The dotted lines indicate the same H I extents as in the correlation maps. Black or gray signal below the dashed line at -2.568 indicates concentrations of correlation signal that are very unlikely ($> 3\sigma$) to be generated by random noise (i.e. the correlation signal excess is statistically significant).

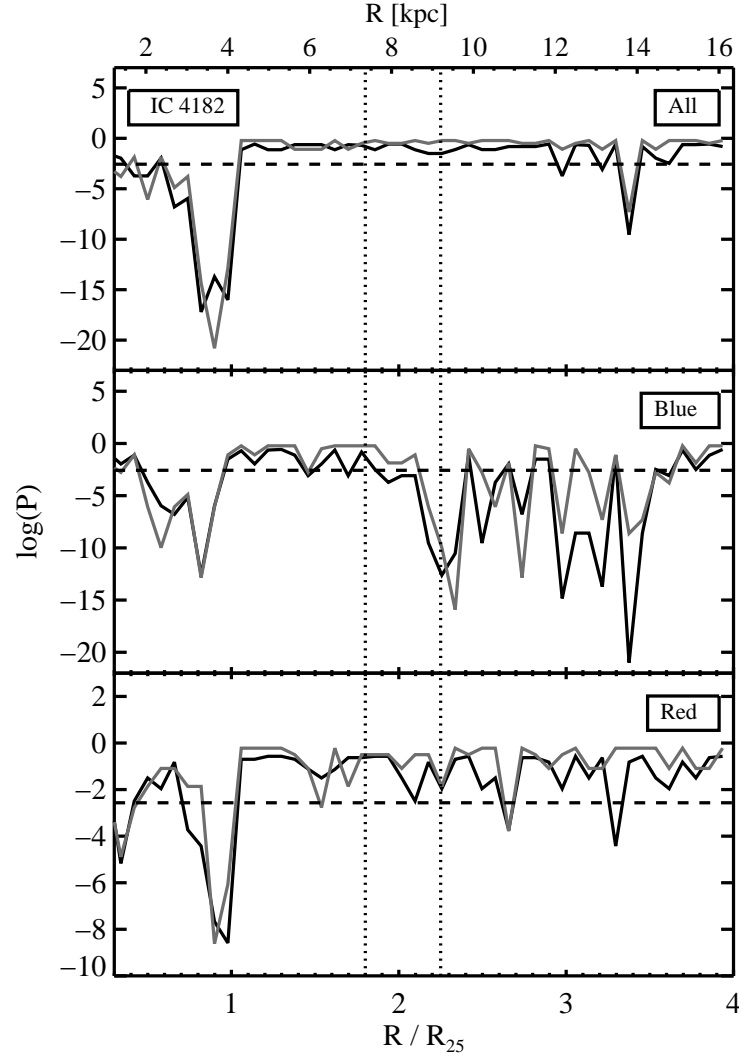


Figure 3.21 Probability (as a function of radius) that peaks in the three-point correlation map of IC 4182 (Figure 3.17) are caused by random excursions. The black and gray lines correspond to the black and gray signal in the correlation map. The dotted lines indicate the same H I extents as in the correlation map. Black or gray signal below the dashed line at -2.568 indicates concentrations of correlation signal in Figure 3.17 that are very unlikely ($> 3\sigma$) to be generated by random noise.

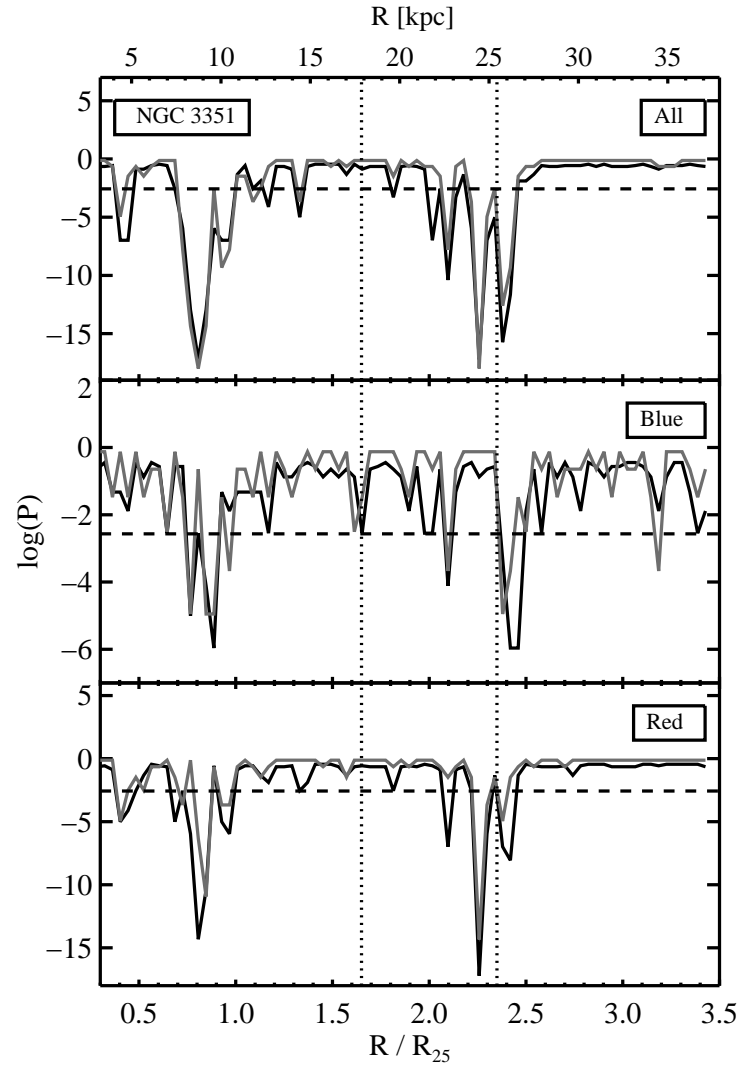


Figure 3.22 Same as Figure 3.21 but for NGC 3351.

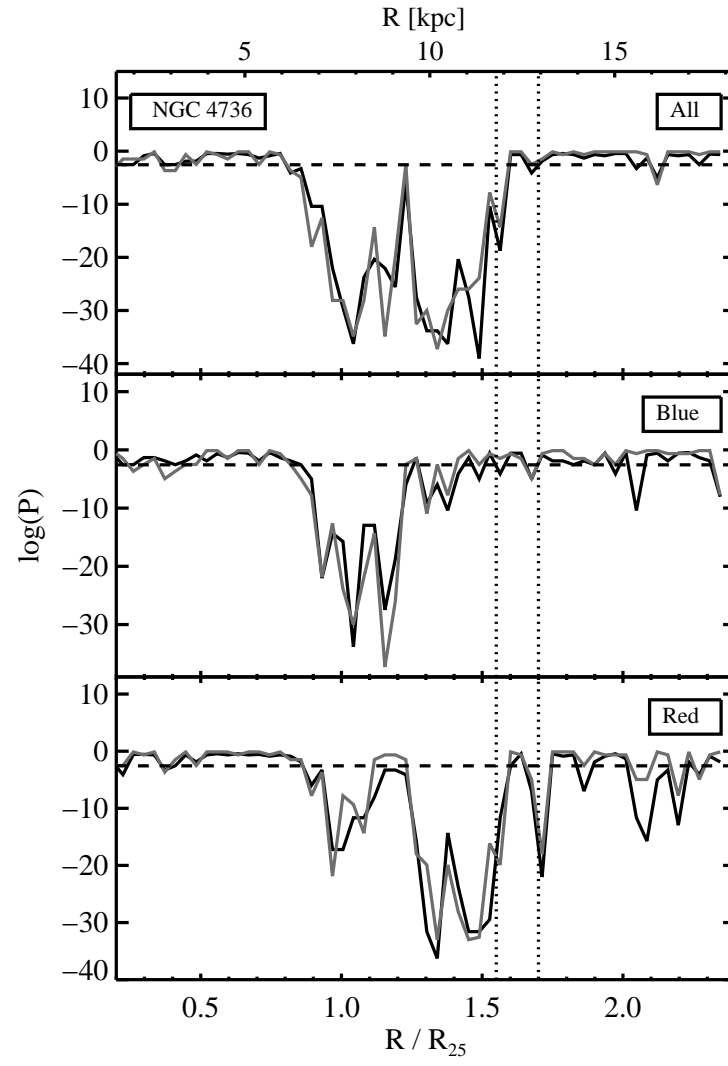


Figure 3.23 Same as Figure 3.21 but for NGC 4736.

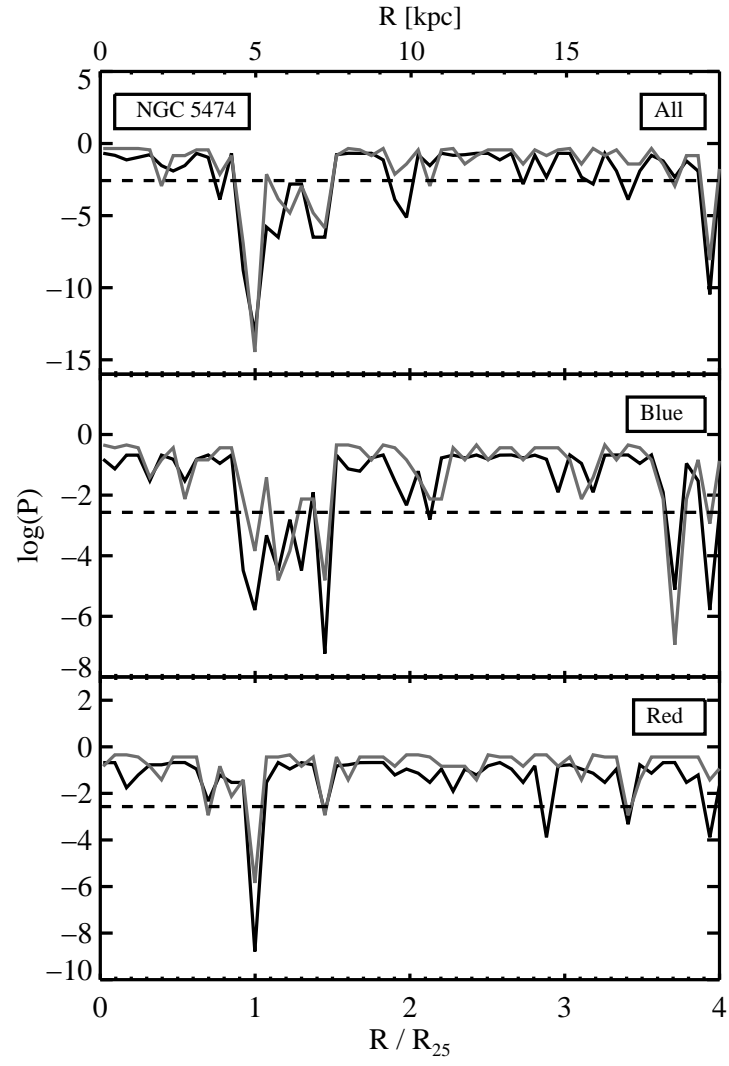


Figure 3.24 Same as Figure 3.21 but for NGC 5474.

Before addressing the results of our LBT correlation maps and the corresponding probability plots, we present a similar correlation analysis of GALEX knots around the galaxies, as well as a cross-correlation analysis of our LBT knots and the underlying H I disks. We then discuss the results of these three analyses (LBT, GALEX, and LBT-H I) together, on a galaxy-by-galaxy basis. Comparison with other data is important to give credence to our detections.

3.5.2 Self-clustering of GALEX Knots

We now apply our three-point correlation technique to analyze the source distribution of UV-bright knots around our galaxies, using data from publically-available GALEX catalogs. We hope to detect UV knot self-clustering (i.e. GALEX knot - GALEX knot clustering) resembling signal in the LBT knot self-clustering maps; matching radial locations of signal could lend support to any marginal detections, and comparing the range of r_{out} values between the LBT and GALEX samples may shed light on cluster group dispersal timescales. When possible, we combine catalogs from shallow ($t_{exp} < 1000$ seconds) and deep exposures to provide the most GALEX sources both near and far from the bright inner disk (regions around the galaxies were masked to avoid saturation during the deep GALEX exposures; the shallow exposures help fill in the source distribution closer to disk). We then cut the combined GALEX source lists to match the ‘blue’ sample of Zaritsky & Christlein (2007) with $FUV-NUV < 1$ and $NUV < 25$, corresponding to clusters younger than ~ 360 Myr. This cut removes sources with detections in only one GALEX band and retains only the reliable knots. We reduce contamination further by only retaining knots that match sources in our final (All-sample) LBT catalogs (to within $3''$, roughly half a GALEX resolution element). After matching to our LBT catalogs, the fraction of GALEX sources remaining is typically $> 90\%$. This explains why GALEX knot self-clustering maps

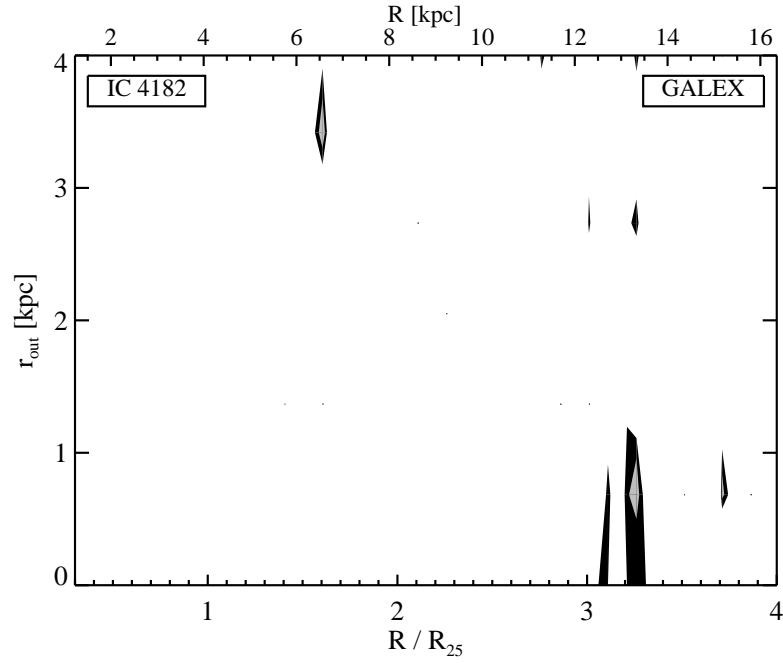


Figure 3.25 Restricted three-point correlation map similar to Figure 3.17 but here using 171 GALEX sources around IC 4182.

made from the LBT-matched catalogs and those made from the unmatched catalogs are not significantly different.

We present the UV knot self-clustering maps from our final GALEX source catalogs (LBT-matched) in Figures 3.25 - 3.28. Unfortunately the number of available GALEX sources is low; 171 were used around IC4182, 179 around NGC 3351, 398 around NGC 4736, and 174 around NGC 5474.

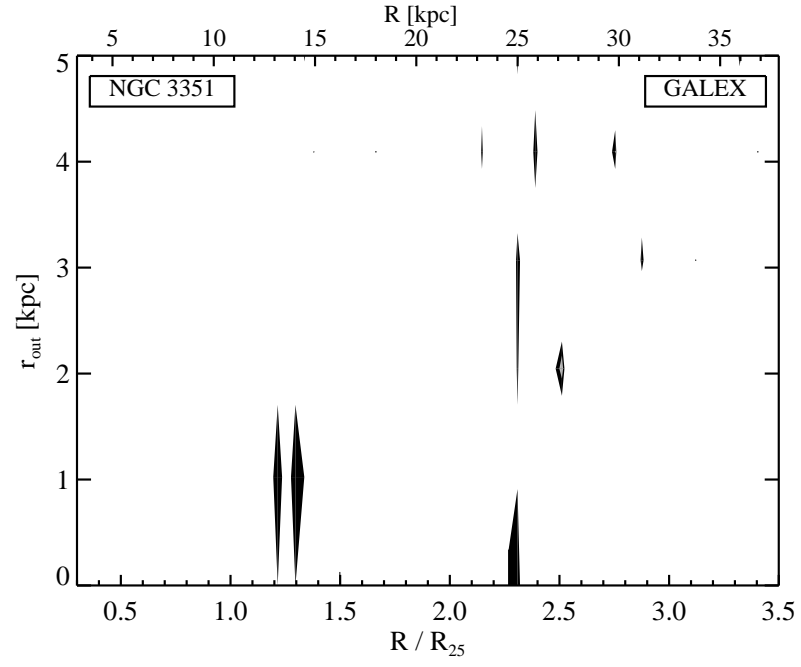


Figure 3.26 Same as Figure 3.25 but from 179 GALEX sources around NGC 3351.

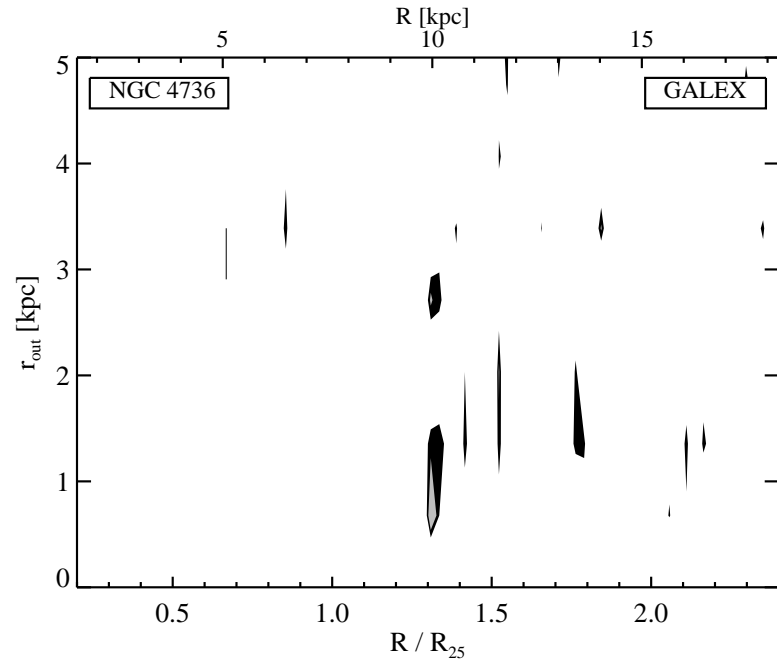


Figure 3.27 Same as Figure 3.25 but from 398 GALEX sources around NGC 4736.

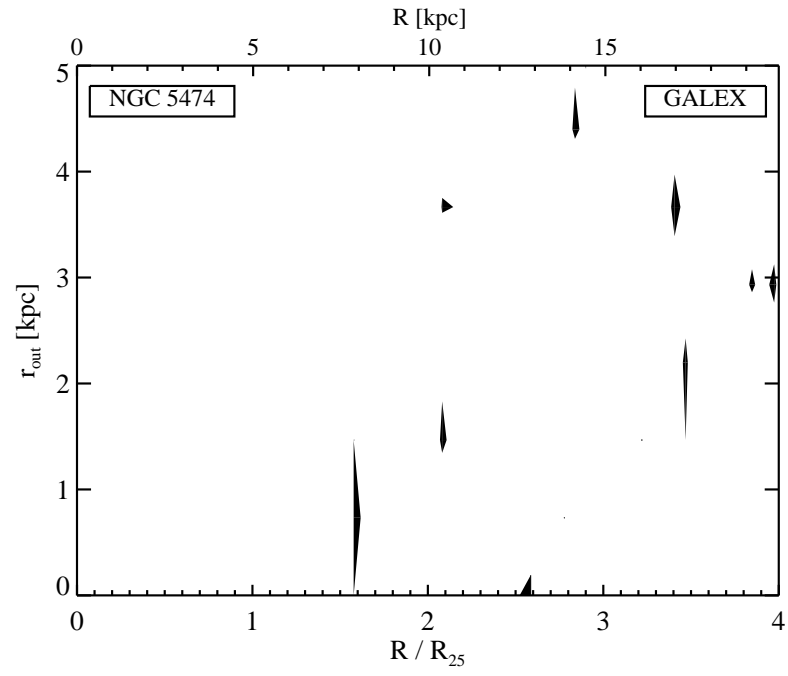


Figure 3.28 Same as Figure 3.25 but from 174 GALEX sources around NGC 5474.

It can be interesting to compare the number of LBT-matched GALEX sources around each galaxy with those remaining in the background-subtracted Hess diagrams from the LBT sample. Table 3.3 presents these numbers from two outer disk annuli for each low-inclination galaxy, between $1.0 - 1.5R_{25}$ and $1.5 - 2.0R_{25}$. Unfortunately the inner annulus is problematic, mainly because the GALEX catalogs near the disk are made from shallow exposures. In the $1.5 - 2.0R_{25}$ annulus, we find that GALEX knots make up between 10%-40% of LBT knots, or 27% on average. We can estimate what this fraction should be for uniform cluster formation by simply comparing the average ages of the two populations: 180 Myr from the GALEX sample (assuming uniform distribution between $0 - 360$ Myr) compared to 500 Myr from the LBT sample (assuming uniform distribution between $0 - 1$ Gyr) leads to an estimated fraction of 36%, very close to our detected average of 27%. A lower fraction implies a higher cluster formation rate in the past, while a higher fraction implies a lower cluster formation rate in the past. The scatter between 10% - 40% suggests that factor of two variations in the cluster formation rate over these timescales are likely, but that the rates do not change by orders of magnitude over the previous Gyr when integrated over ~ 200 Myr.

Table 3.3. Sources in LBT-matched GALEX catalogs

Name	annulus	N_{GALEX}	N_{Hess}	frac.
IC 4182	1.0 – 1.5	5	348	1
IC 4182	1.5 – 2.0	28	69	41
NGC 3351	1.0 – 1.5	12	548	2
NGC 3351	1.5 – 2.0	27	266	10
NGC 4736	1.0 – 1.5	56	2738	2
NGC 4736	1.5 – 2.0	172	704	24
NGC 5474	1.0 – 1.5	8	427	2
NGC 5474	1.5 – 2.0	16	52	31

Units: annulus in R_{25} and frac. as a percentage. Because the GALEX catalogs already had so few usable sources we did not mask the regions we did in our LBT mosaics because of bright stars; therefore, so that the fields are more comparable, N_{Hess} listed here are the values from our LBT catalogs before the bright star masks were applied.

3.5.3 Cross-correlation of LBT Knots and Neutral Gas Disks

We now compare the distribution of our LBT sources to the underlying neutral gas. We use this cross-correlation as another way to constrain the extents of the stellar disks; comparison to the H I structure may help us tease out more cluster signal at the extreme edges of the disk, as in Herbert-Fort et al. (2009), and help us trace how closely LBT knot concentrations are associated with concentrations in the H I.

Because we will perform a cross-correlation analysis we are restricted to our low-inclination sample (IC 4182, NGC 3351, NGC 4736, and NGC 5474), though unfortunately we do not have a suitable H I map of NGC 5474. The integrated H I (moment 0) maps of NGC 3351 and NGC 4736 come from The H I Nearby Galaxy Survey (THINGS; Walter et al. , 2008) and the H I map of IC 4182 comes from the Westerbork H I Survey of Spiral and Irregular Galaxies (WHISP; Swaters et al. , 2002).

We estimate the gas disk extents in the same manner as Herbert-Fort et al. (2009), by creating histograms that show the number of H I pixels per kpc^2 above a certain $N(\text{HI})$ threshold, as a function of R in $0.025R_{25}$ -wide elliptical annuli. The first threshold we consider is simply the noise level of the H I maps (see below), to determine the maximum extents of the gas disks. The neutral gas around IC 4182 extends to $\sim 2.25R_{25}$, to $\sim 2.4R_{25}$ around NGC 3351, and to $\sim 1.8R_{25}$ around NGC 4736. Figures 3.29 - 3.31 show the restricted three-point cross-correlation between the LBT knots and the H I pixels lying above the $N(\text{HI})$ threshold (listed in the legend at the bottom right of each panel). The top panels are from all sources with $-1.7 < U - V < 0.7$ and $19 < V < 27.5$, while the lower panels result from splitting the sample into blue and red components on either side of $U - V = -0.2$ (middle and bottom panel, respectively). Black and

gray show areas where signal is detected at $> 95\%$ and $> 99\%$ significance, respectively. The dotted lines bracket the radial extent of the H I pixels used. The figures show how LBT knots correlate with H I features, down to very low density gas; Herbert-Fort et al. (2009) showed that vertical bands of signal here can highlight radii where the knots are tracing a gaseous spiral arm.

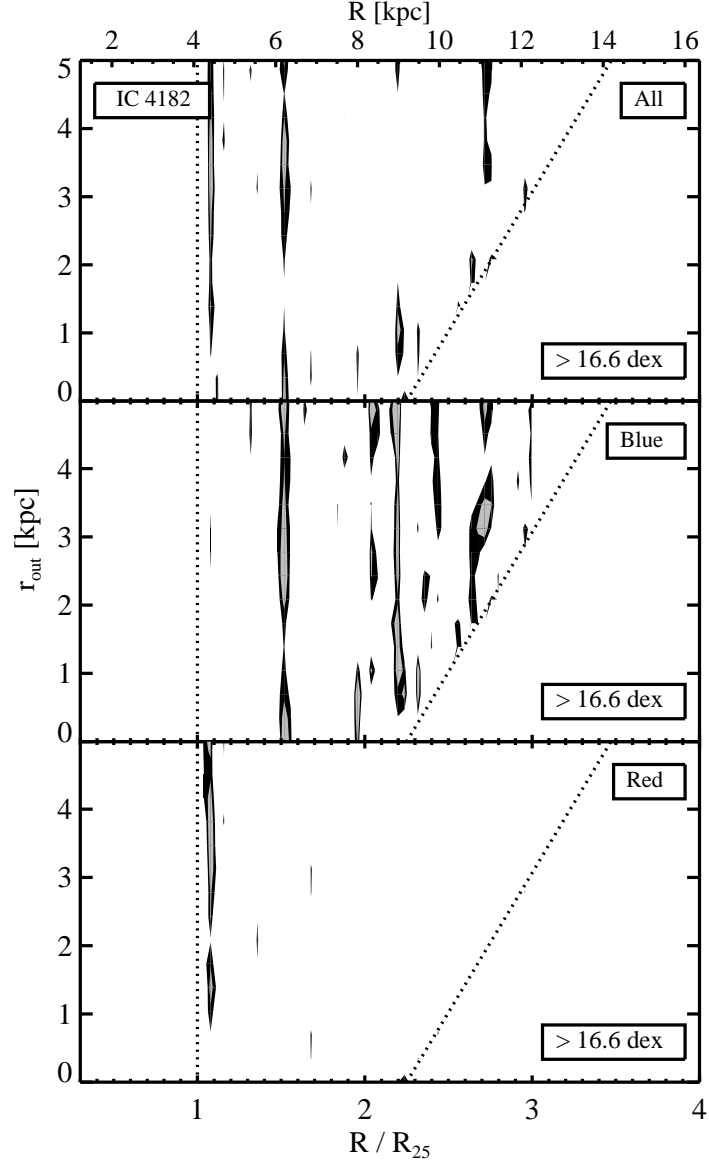


Figure 3.29 Restricted three-point cross-correlation maps of LBT-detected knots around IC 4182 and H I pixels with $N(\text{HI})$ above the noise level of the integrated H I map ($N(\text{HI}) > 4.0 \times 10^{16} \text{ cm}^{-2}$ here). The dotted lines bracket the radial extent of the H I pixels used; because no H I pixels exist beyond the dotted line on the right, we will not see signal at low r_{out} beyond this furthest H I radius (this explains the diagonal nature of signal at the largest R). Only knots between $1.0 - 3.0R_{25}$ were used.

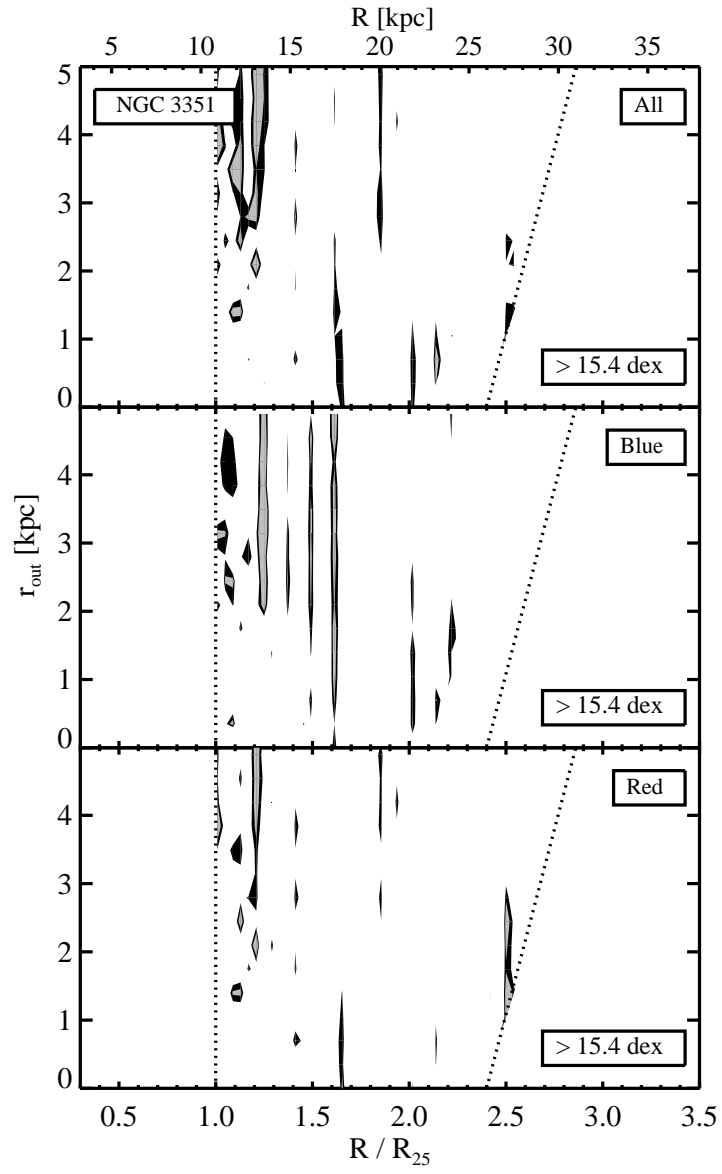


Figure 3.30 Same as Figure 3.29 but for NGC 3351. Only sources between $1.0 - 3.5R_{25}$ were used.

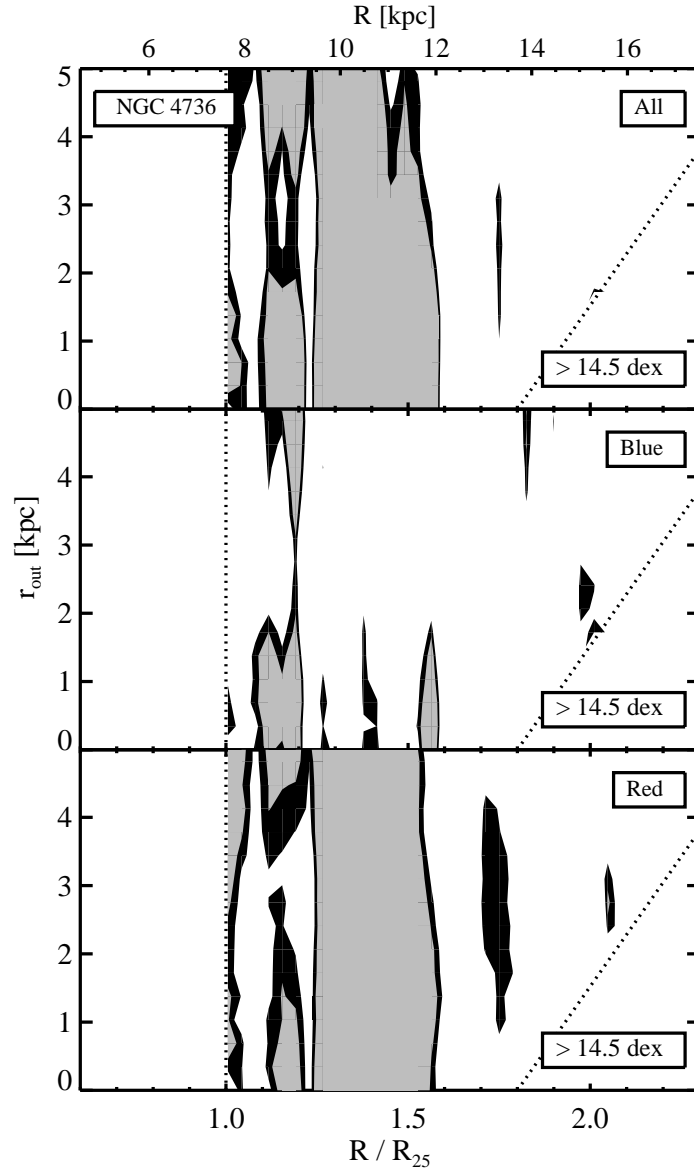


Figure 3.31 Same as Figure 3.29 but for NGC 4736. Only sources between $1.0 - 2.2R_{25}$ were used.

We take the cross-correlation a step further and try to accentuate the knot-gas correlation by focusing solely on our ‘Blue’ LBT knot sample, as this is the group most likely to still be found near the H I features from which the knots were born (out of molecular gas that survives in dense H I regions). The hope is that this group will show stronger, clearer signal with which to estimate the stellar disk extent via the knots.

Figures 3.32 - 3.34 show the cross-correlation for different H I pixel cuts; specifically $N(\text{HI}) < 1.0 \times 10^{20} \text{ cm}^{-2}$ (top), $N(\text{HI}) > 1.0 \times 10^{20} \text{ cm}^{-2}$ (middle), and $N(\text{HI}) > 2.0 \times 10^{20} \text{ cm}^{-2}$ (bottom). The threshold for the highest density gas, $N(\text{HI}) > 2.0 \times 10^{20} \text{ cm}^{-2}$, was chosen to match the damped Lyman- α (DLA) system threshold, which distinguishes between predominantly neutral and predominantly ionized gas (see Wolfe et al. , 2005, and references therein). The $N(\text{HI}) = 2 \times 10^{20} \text{ cm}^{-2}$ boundary represents the edge of the dominant reservoir of neutral gas available for star formation in the disk. The high/low density level, $N(\text{HI}) = 1.0 \times 10^{20} \text{ cm}^{-2}$, was determined by eye, by reducing the threshold until the H I contours closely resembled the distribution of the ‘Blue’ knots. The radial extent of the H I pixels used decreases as the column density threshold is increased, though as the density threshold is increased we are more likely selecting H I structures that could host cluster formation—unless the gas has been consumed to make the clusters.

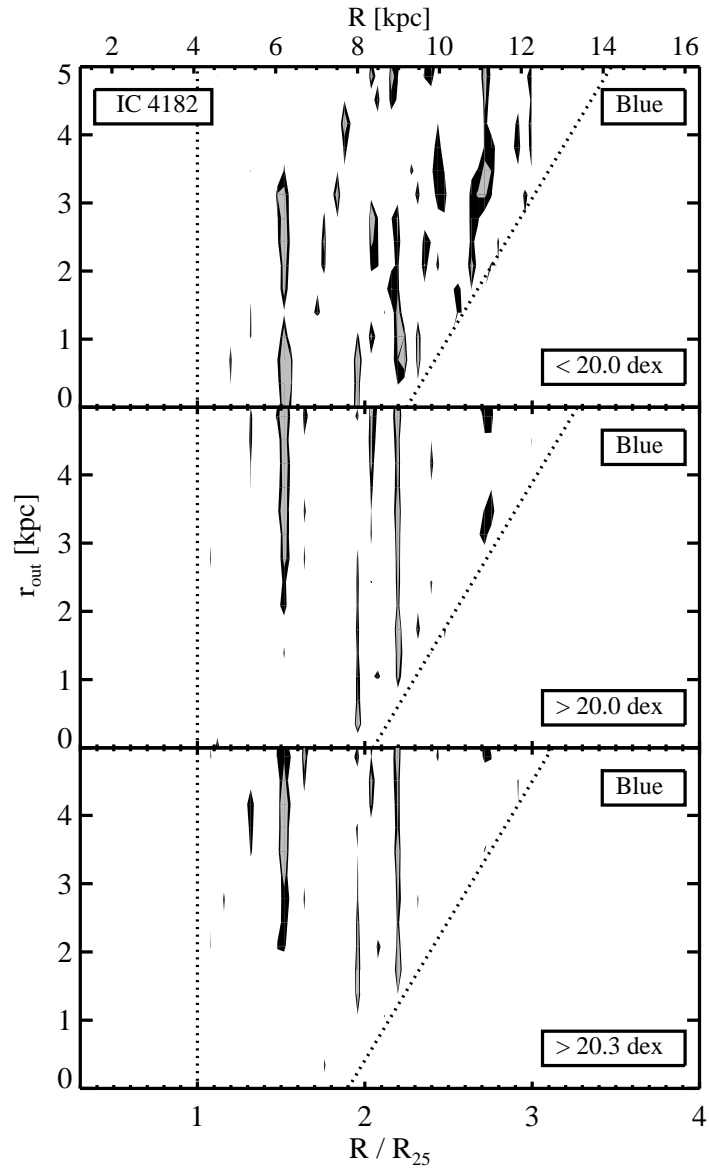


Figure 3.32 Same as Figure 3.29 but only for blue sources around IC 4182 and for different $N(\text{HI})$ pixel cuts.

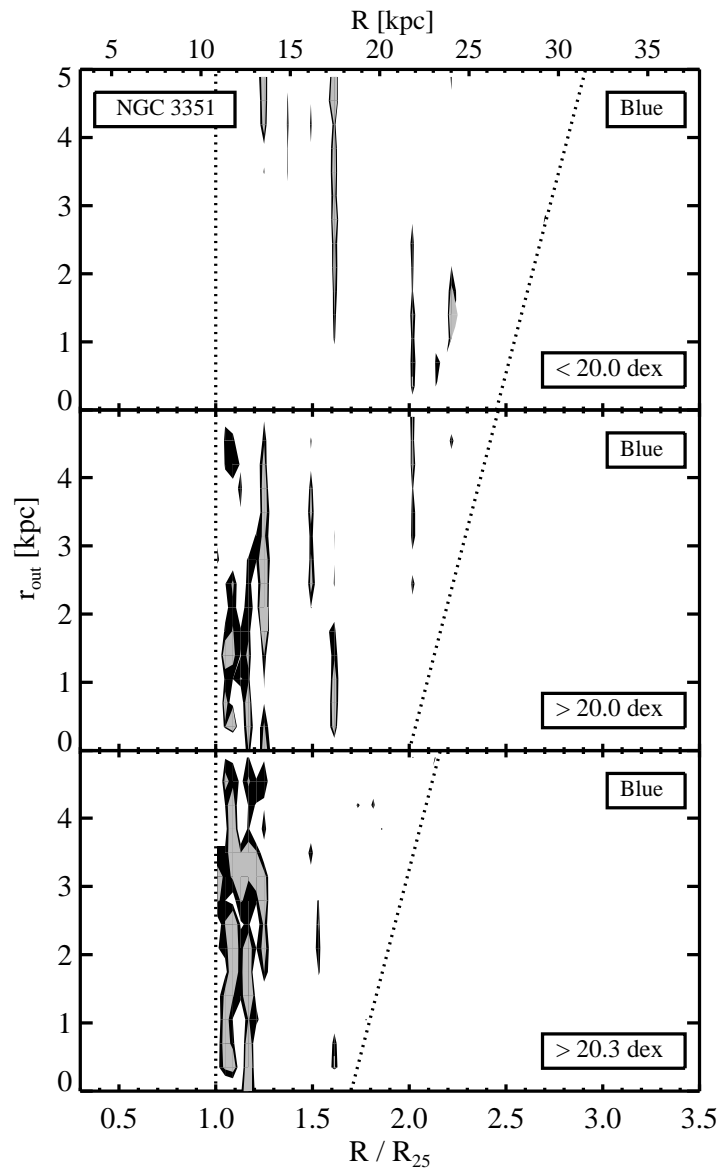


Figure 3.33 Same as Figure 3.32 but for NGC 3351.

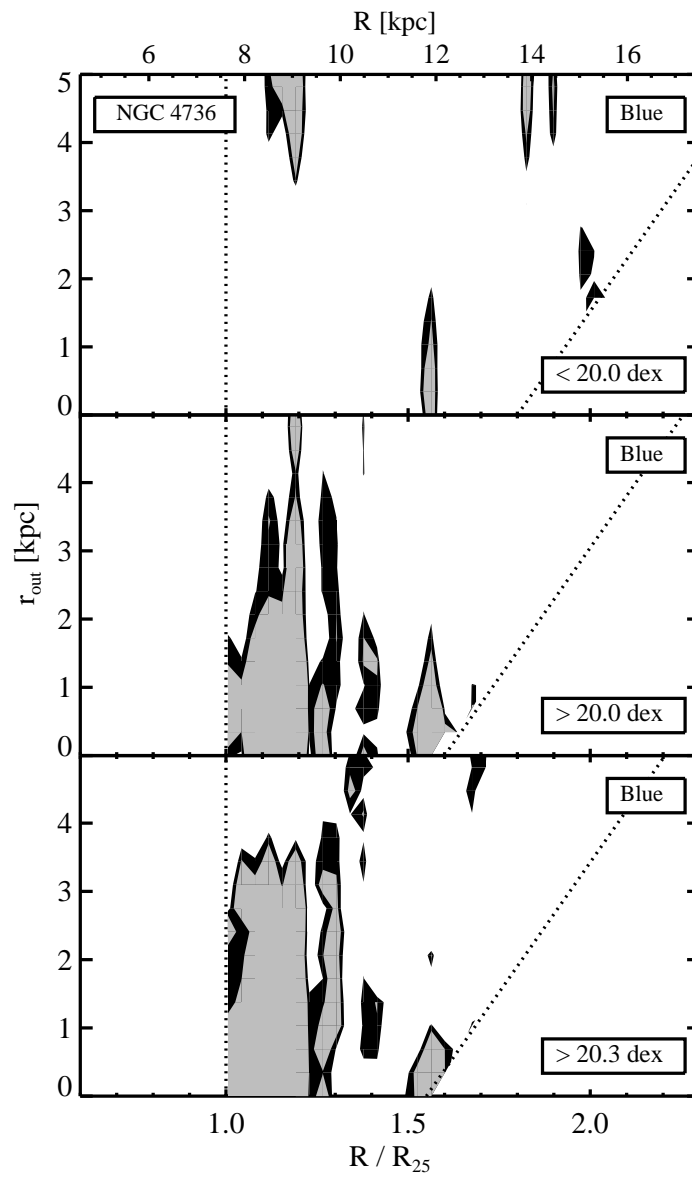


Figure 3.34 Same as Figure 3.32 but for NGC 4736.

3.5.4 Discussion of Correlation Results from All Datasets

A few general comments before we discuss the galaxies individually. In three of the four LBT correlation maps (Figures 3.17 - 3.20) there is apparently significant signal at very large radii, even beyond the H I (unfortunately, we do not have H I data of NGC 5474). Though offhand we are skeptical of correlation signal in these distant regions, this may be an exciting result, possibly pointing to a time when the gas was more extended. We examined the galaxy images and do not see any obvious groupings of LBT knots at radii beyond the H I extent. However, the knots can be very difficult to find when they are far from the disk and not clustered tightly with others. When comparing maps made using the masked and unmasked source distributions (masked to limit the bright star effect previously discussed), much of the signal beyond the H I extent appears to be artificial. We hesitate to push the masking further because of limitation in the number of sources near the mosaic edges. We have tried to increase masking near the brightest sources but we are unable to completely clean some of the maps. Nevertheless, although much of the most distant signal appears to be artificial, we will show why we believe a few of these features are real. We acknowledge the possibility that some clusters may reside beyond the edge of their gas disks, but to be convinced we must see both significant signal in the probability plots (Figures 3.21 - 3.24) and confirmation in either our mosaics or existing UV or H I data.

We now discuss the correlation plots for each galaxy.

3.5.4.1 IC 4182

We find that that the majority of signal disappears right around $\sim R_{25}$ in the LBT knot correlation and probability plots of IC 4182. The Red clump of signal out near $1.5R_{25}$ in the correlation map is likely a remnant of signal caused by a bright

star at that radius (this clump is not significant at the 3σ level, according to the probability plot). However, vertical bands of signal can be seen near $1.5R_{25}$ in the All and Blue panels of the LBT knot - H I cross-correlation plot (Figure 3.29), which Herbert-Fort et al. (2009) show to be a sign of knots being associated with spiral structure in the gas. There is no signal at $1.5R_{25}$ in the Red plot of the cross-correlation plot (Figure 3.29). We believe that there is a mix of Blue LBT knots truly associated with H I spiral structure and the bright star effect occurring at the same radius ($1.5R_{25}$). Interestingly, the Blue LBT knot - H I cross correlation at $1.5R_{25}$ is most closely related to the lower-density gas, $N(\text{HI}) < 20.0$ dex.

Further out in R , the Blue panel of the LBT knot probability plot (Figure 3.21) shows much more noisy, scattered signal beyond the edge of the H I than do the All or Red panels. The ‘noisy’ Blue signal in the LBT correlation map between $2 - 3R_{25}$ that is statistically significant in the probability plot, appears to coincide with the bands of Blue signal in the LBT knot - H I cross-correlation plots, suggesting that Blue clusters beyond the edge of the gas are nevertheless strongly associated with the outer disk gas structure. This suggests that the knots were born from gas that was once part of the disk but no longer exists. The GALEX correlation plot does not show any signal between $2 - 3R_{25}$, which could mean that the majority of the Blue clusters causing the correlation signal are towards the high end of their age range (~ 300 Myr), yet still < 1 Gyr old because there is not as much significant signal in the Red panel of the probability plot at these radii. Looking at the Blue LBT knot - H I cross-correlation closer, as function of the $N(\text{HI})$ cut (Figure 3.32), we see that the majority of the Blue signal between $2 - 3R_{25}$ comes from knots associated with the lower density gas, the ‘fluff’ towards the edges of the disk. There are however bands of signal near 2 and $2.2 R_{25}$ in the bottom panels of Figure 3.32, showing that some of the Blue knots closer in

are also associated with the larger, more significant H I arms, at the edge of the gas disk.

All panels in the LBT knot correlation probability plot show a significant excess around $3.3 R_{25}$, far outside the edge of the gas disk (the gas extends to $2.2 R_{25}$). This feature is especially interesting because it corresponds to strong signal at $3.3 R_{25}$ in the GALEX knot self-correlation map (Figure 3.25). There is an obvious clumping of GALEX sources at that radius. If these distant sources are in fact clusters, rather than an extremely-unlikely grouping of background objects that happen to pass our cuts, they are very interesting objects for further study.

3.5.4.2 NGC 3351

The LBT knot correlation map and corresponding probability plot for NGC 3351 (Figures 3.18 and 3.22) show believable signal out to $\sim 1.3 R_{25}$. The GALEX signal near 1.3 and $2.3 R_{25}$ around NGC 3351 may be real, since it matches the radius of signal in the LBT maps, though the latter is right at the edge of the gas disk. Vertical bands of signal are observed in the LBT knot - H I cross-correlation map (Figure 3.30) near $1.6 R_{25}$ in all three galaxies, as well as near $2.2 R_{25}$ in the Blue panel and $2.5 R_{25}$ in the Red panel, again suggesting that the features near $2.3 R_{25}$ in the LBT knot correlation map are real. Looking at the Blue LBT knot - H I cross-correlation map for different $N(\text{HI})$ cuts (Figure 3.33), it appears that the knots trace the denser gas out to $\sim 1.6 R_{25}$ (and clearly trace spiral structure out to $1.2 R_{25}$), however the furthest cross-correlation signal again comes from the low-density (top) panel near $2.2 R_{25}$ (signal is also seen here in the GALEX correlation map). This again suggests that star formation is occurring out near the edge of the gas disk, though it is likely occurring in a sparse, globally under-dense environment, and suggests recent cluster formation can occur somewhat away from *current* sites of higher density gas. The clouds may evolve quickly and therefore

tests of the star formation laws may appear to fail even if the law does not.

3.5.4.3 NGC 4736

The LBT knot correlation map and corresponding probability plot for NGC 4736 (Figures 3.19 and 3.23) show signal extending to at least the limit of the HI disk ($\sim 1.6R_{25}$). This galaxy has an obvious overdensity of knots in the bright ‘ring’ surrounding it. Trujillo et al. (2009) showed that this ring is actually a complex structure of wound spiral arms (perhaps caused by secular processes in the inner disk). Those authors also found that the outer disk of NGC 4736 is very actively forming stars. The symmetric nature of the outer disk arms or ring is represented by the strong vertical bands of signal between $1.3 - 1.5R_{25}$ in Figure 3.19. We are skeptical of excess signal beyond the H I extent of this galaxy because it is coincident with the original artificial signal (which faded when we applied additional bright star masking), though there is some evidence that signal near 1.8 and $2.0R_{25}$ is real.

The signal in the NGC 4736 GALEX correlation map we have most confidence is real is that near $1.3R_{25}$. This galaxy has the most GALEX sources available, giving us more confidence in the correlation map, and the signal at $1.3R_{25}$ corresponds to the booming signal we see in the LBT maps, which we believe is associated with the bright outer arms or ring around this galaxy. This signal is further supported by the bands of signal near $1.3R_{25}$ in the LBT knot - H I cross-correlation map (Figure 3.31). Note that Zaritsky & Christlein (2007) also found NGC 4736 to have a statistically significant UV outer disk excess between $1.25 < R_{25} < 2$.

The GALEX signal at $1.8R_{25}$ may also be real, in which case we again might have a mix of clusters and bright stars at the same radius. The Red panel in the LBT knot - H I cross-correlation map (Figure 3.31) also shows signal at $1.7R_{25}$,

lending support to this detection. Figure 3.31 also shows signal near $2.0R_{25}$, matching the spikes seen in the LBT knot correlation probability plots. The Blue LBT knot - H I cross-correlation map for different $N(\text{HI})$ cuts (Figure 3.34) shows that the signal near $2R_{25}$, if real, is primarily associated with lower density gas. Closer in to the disk, the cross-correlation is most significant with higher density gas.

3.5.4.4 NGC 5474

NGC 5474 is our cleanest LBT knot correlation map and shows believable signal to $\sim 1.4R_{25}$. Unfortunately we do not have H I data for NGC 5474. The GALEX knot correlation map of NGC 5474 shows signal near $1.5R_{25}$, right next to where we see signal in the LBT map, though the GALEX signal is very weak. A closer look at the GALEX images and source distribution strongly suggests that this feature is real, due to knots in the disk. Zaritsky & Christlein (2007) found NGC 5474 to have a significant UV excess in its outer disk, likely due to this grouping of knots.

3.6 Summary and Conclusions

We summarize our results as follows:

- We find an excess of outer disk sources in all six galaxies between $1.0 - 1.5R_{25}$. The knots detected resemble $\sim 10^3 M_{\odot}$ star clusters < 1 Gyr old.
- We construct background-subtracted Hess diagrams for different outer disk annuli and generally find the disk cluster components to be $\sim 29 \text{ mag arcsec}^{-2}$ or fainter in V .
- When combining our individual background-subtracted Hess diagrams into an average Hess diagram, we find that our sample shows an excess out to $2R_{25}$. Comparing to simulated Hess diagrams suggests an outer disk cluster formation

rate of one cluster every ~ 2.5 Myr, or $\sim 0.004 M_{\odot} \text{ pc}^{-2} \text{ Gyr}^{-1}$ (assuming $R_{25} = 5$ kpc and $10^3 M_{\odot}$ clusters).

- We construct restricted three-point correlation maps to measure the self-clustering of knots around our four low-inclination galaxies. In order to better to visualize correlation signal that is most likely associated with disk clusters, we create binomial probability plots showing the likelihood that concentrated correlation signal is real (i.e. not due to random fluctuations) as a function of radius. We caution that a lack of signal in this approach does not mean a lack of knots, just a lack of tightly-clustered knots. The furthest we detect clustered knots is $3.3 R_{25}$ in IC 4182, well beyond the edge of the gas disk.

- We present restricted three-point correlation maps of UV-bright outer disk GALEX sources and find a few cases of believable signal that support signal seen in other plots (e.g. that near $1.3 R_{25}$ in NGC 4736). Unfortunately the number of GALEX sources available was very small. Though more UV sources are required for a proper analysis of this sort, our GALEX maps still proved useful for comparisons to other maps.

- We do believe the GALEX correlation signal near $3.3 R_{25}$ in IC 4182 but we are unsure whether it originates from disk sources or a coincident grouping of background objects. If these are actually star clusters at the distance of the galaxy, they represent a very interesting class of clusters residing far outside of their gas disks. Perhaps they have drifted from their birthsites or the gas disk has changed since the clusters were born.

- The GALEX:LBT knot fractions (from our GALEX and Hess diagram analyses, respectively) range between 10% - 40% with an average of 27%. This is roughly what is expected from an outer disk forming stars uniformly over at least the past Gyr, when one considers the average age of both populations of

knots (180 Myr for GALEX and 500 Myr for LBT). The scatter in our observed fraction suggests that factor of two variations in the cluster formation rate over these timescales are likely, but that the rates do not change by orders of magnitude over the previous Gyr when integrated over ~ 200 Myr.

- We measured cross-correlation signal between our LBT-detected knots and the H I disk using a three-point correlation map approach. This helps trace clusters that are correlated with arms in the gas disk; we find examples of this near $1.5R_{25}$ in all three low-inclination galaxies for which we obtained H I maps. We also find evidence that knots beyond the gas may still be correlated with H I disk structures, lending support to the idea that ‘extra-disk’ clusters do exist. All three galaxies with H I data show evidence for clusters existing slightly beyond the current edge of the gas disk (a few kpc beyond). This implies either that 1) H I is not a perfect tracer of where cluster formation can happen, 2) the H I contours evolve rapidly (over a few kpc in a few hundred Myr), or 3) the clusters have drifted significantly from their birthsites. A drift of just 6 km s^{-1} could transport a cluster a few kpc in 500 Myr, so the latter scenario looks possible, though the others are not ruled out.

- Finally, we test whether we can accentuate the knot-gas correlation by only considering Blue LBT sources and a range of $N(\text{HI})$ thresholds for the gas. We find knots correlated with low-density gas ($N(\text{HI}) < 1.0 \times 10^{20} \text{ cm}^{-2}$) at the largest radii in most galaxies. Our results agree with simulations that show outer disk star formation happening in low-density regions, in small clumps that locally lie above the Kennicutt threshold for star formation (e.g. Bush et al. , 2008).

Overall, it appears that outer disk clusters are common in nearby galaxies. Our results suggest that they are born in groups in outer disks and can remain clustered for a Gyr or more. There may also exist clusters beyond the edge of H I

disks. Further study of these most distant knots could yield valuable information on galaxy growth and long-term evolution.

CHAPTER 4

THE SURFACE MASS DENSITY AND STRUCTURE OF THE OUTER DISK OF NGC 628

4.1 Chapter Abstract

We study the kinematics of GALEX-selected $H\alpha$ knots in the outer disk (beyond R_{25}) of NGC 628 (M74), a galaxy representative of large, undisturbed, extended UV (Type 1 XUV) disks. Our spectroscopic target sample of 235 of the bluest UV knots surrounding NGC 628 yielded 15 $H\alpha$ detections (6%), roughly the number expected given the different mean ages of the two populations. The measured vertical velocity dispersion of the $H\alpha$ knots between $1 - 1.8R_{25}$ (13.5 – 23.2 kpc) is $< 11 \text{ km s}^{-1}$. We assume that the $H\alpha$ knots trace an ‘intermediate’ vertical mass density distribution (between the isothermal $\text{sech}^2(z)$ and exponential distributions) with a constant scaleheight across the outer disk ($h_z = 700 \text{ pc}$) and estimate a total surface mass density of $7.5 M_{\odot} \text{ pc}^{-2}$. This surface mass density can be accounted for by the observed gas and stars in the outer disk (little or no dark matter in the disk is required). The vertical velocity dispersion of the outer disk $H\alpha$ knots nearly matches that measured from older planetary nebulae near the outskirts of the optical disk by Herrmann et al., suggesting a low level of scattering in the outer disk. A dynamically cold stellar component extending nearly twice as far as the traditional optical disk poses interesting constraints on the accretion history of the galaxy.

4.2 Chapter Introduction

The outskirts of a galaxy are expected to host signatures of disk formation and hierarchical accretion because of the long dynamical times at these radii. Toth

& Ostriker (1992) argued that the thinness and coldness of inner galactic disks (inside the optical radius, R_{25}) posed significant problems for hierarchical models of galaxy formation. Qualitatively, these concerns become more pronounced if one can establish that cold galactic disks extend to even larger radii.

Various studies have revisited the cold disk problem, generally finding that accretion events are less destructive than originally envisioned. Most recently, Kazantzidis et al. (2009) studied the dynamical response of thin galactic disks to bombardment by cold dark matter substructure out to large radii in fully self-consistent, dissipationless N -body simulations. They found that disks survive these bombardments, but that they produce considerable thickening and heating at all radii, substantial flaring, and an increase in the stellar surface density in the disk outskirts (the latter due to outward radial migration of old stars during the growth and redistribution of disk angular momentum). Observations of the dynamical state of outer stellar disks (Christlein & Zaritsky, 2008) demonstrate that outer disks generally continue to obey the flat rotation curves of inner disks, with no increase in the in-plane velocity dispersion. Here we present the face-on kinematics of one nearby galaxy, NGC 628 (M74), and compare to both neutral hydrogen and existing stellar measurements at smaller radii. NGC 628 is a prototypical Grand Design spiral galaxy (type SA(s)c, dynamical mass within the studied region $\sim 3.3 \times 10^{11} M_{\odot}$, assuming $v_{rot} = 200 \text{ km s}^{-1}$ out to $2.3R_{25}$; Thilker et al., 2007; Kamphuis & Briggs, 1992), and is by far the largest and most massive member of its small group (the brightest member after NGC 628, UGC1176, is ~ 4.5 mag fainter and over 125 kpc away). NGC 628 shows a standard exponential optical light profile to R_{25} , with only a very slight possible downbending in the profile to $\sim 1.3R_{25}$, the extent of the deep optical observations (Natali et al., 1992). Using ultraviolet (UV) imaging, Thilker et al. (2007) classified NGC

628 as a Type 1 extended UV (XUV) disk, due to the structured, UV-bright emission complexes seen in the outer disk. Because the stellar disk appears largely undisturbed (both in optical and UV imaging, and, as we will show, from the kinematics) and because NGC 628 dominates the dynamics of its local environment, we treat it as representative of large, isolated spiral galaxies in the nearby universe.

The outer disks of galaxies have received much recent attention, both observational (Thilker et al. , 2007; Gil de Paz et al. , 2007; Zaritsky & Christlein , 2007; Christlein & Zaritsky , 2008; Herbert-Fort et al. , 2009; Trujillo et al. , 2009; Herrmann et al. , 2009) and theoretical (Bush et al. , 2008; Roškar et al. , 2008a,b; Kazantzidis et al. , 2009). The surge in interest in outer disks has been fueled by recent ultraviolet (UV) observations of nearby disks with the GALEX satellite (Martin et al. , 2005; Thilker et al. , 2007). Previously, Ferguson et al. (1998) had used deep $H\alpha$ imaging to discover star formation in an extended component around three nearby galaxies, yet the ubiquity of this component in other disks remained largely unrecognized until the UV observations.

This neglect stemmed in part from the fact that $H\alpha$ traces a limited subpopulation of the outer disk, namely those regions with O and B stars. Even relatively young regions may lack OB stars because they are older than 10 Myr or because they simply did not form such massive stars (Ferguson et al. , 1998; Herbert-Fort et al. , 2009; Pflamm-Altenburg & Kroupa , 2008). As such, the ubiquity of outer disk star formation is somewhat concealed. These barriers are removed with UV observations and we now know that many nearby galaxies host young outer disk stellar populations ($> 30\%$; Thilker et al. , 2007; Zaritsky & Christlein , 2007). While galactic interactions can dramatically increase the level of outer disk star formation (see the well-known cases of M83, NGC 4625 and M94; Thilker et al.

, 2005; Gil de Paz et al. , 2005; Trujillo et al. , 2009), even isolated galaxies show low-levels of ongoing star formation in their outer parts (Ferguson et al. , 1998; Christlein & Zaritsky , 2008; Herbert-Fort et al. , 2009). However, the $H\alpha$ knots provide the bright emission lines that make it possible to measure the kinematics we present here.

While the gaseous outer disk of NGC 628 has been well-studied, for example by Kamphuis & Briggs (1992), the stellar component near the outskirts of the disk remains poorly characterized. Observers have acquired deep broadband imaging of the outer disk of NGC 628 (e.g. Natali et al. , 1992), however the diffuse light becomes difficult to reliably trace fainter than ~ 28 mag arcsec $^{-2}$ in V , or beyond $\sim 1.3R_{25}$. To sidestep the difficulty of obtaining detailed kinematics from low surface brightness emission, Herrmann et al. (2009) use planetary nebulae (PNe) across the face of NGC 628 to trace the underlying stellar distribution and to estimate the total mass density of the disk using the kinematic approach of van der Kruit (1988) (specifically, by measuring the vertical velocity dispersion of a tracer of the disk mass distribution to estimate the underlying surface mass density). In principle, the PNe provide an excellent approach to the problem, with large numbers of PNe available for analysis. Unfortunately for our purposes, the Herrmann et al. (2009) study of PNe in NGC 628 is mostly constrained to the inner disk (only two of their PNe are beyond R_{25} ; their study of M83 and especially M94 yield more PNe in those outer disks, however those are interacting systems for which the kinematics are complicated by recent events). The current work represents the first to analyze the disk kinematics out to $1.8R_{25}$ in NGC 628. Nevertheless, the results from Herrmann et al. (2009) at the largest radii ($\sim R_{25}$) provide an interesting comparison to the results found here, especially because the PNe trace a population of objects that is on average at least $100\times$ older than

the $H\alpha$ knots considered here.

We use multiobject spectroscopy to search for $H\alpha$ emission associated with blue GALEX sources in the outer disk of NGC 628. We measure the dispersion of the $H\alpha$ knot vertical velocity distribution, estimate the surface density of the outer disk, and determine if the baryonic material can account for the inferred mass. We then compare the results from the young $H\alpha$ knots to those from the PNe and consider the implications on disk evolution from the two measurements. Section 4.3 presents our sample selection, observations and data reductions. Section 4.4 presents our analysis, results and discussion, including our measurement of the vertical velocity dispersion of the $H\alpha$ knots and the surface mass density of the outer disk. Section 4.5 presents a summary and our conclusions.

4.3 Sample Selection, Observations, and Data Reduction

We selected our target sample from sources identified in GALEX imaging of NGC 628 by Zaritsky & Christlein (2007). We target ‘blue’ sources with $FUV - NUV < 1$ and $NUV < 25$, corresponding to the expected colors of star clusters with ages < 360 Myr. We observed two fields that cover the outer disk of NGC 628 with the Inamori Magellan Areal Camera and Spectrograph (IMACS; Dressler et al. , 2006) using the ‘short’ f/2 camera mode and the 600 line grating centered at 7695 \AA , providing a spectral resolution of $\sim 0.6 \text{ \AA pixel}^{-1}$, or $\sim 27 \text{ km s}^{-1} \text{ pixel}^{-1}$ near $H\alpha$, on August 2, 3, and 4, 2005 (UTD). The IMACS field of view in the short camera mode is $\sim 27'$ on a side, providing coverage out to $3R_{25}$ ($R_{25} = 5.2$ arcmin; Kamphuis & Briggs , 1992). The IMACS plate scale in our setup is $0.2 \text{ arcsec pixel}^{-1}$. We cut 162 and 151 slits in the masks of the northeastern and southwestern fields, respectively, giving priority to the brightest GALEX sources with the bluest $FUV - NUV$ colors (clusters with $H\alpha$ emission are expected to

have ages < 10 Myr, powered by massive stars that will make the clusters blue in the GALEX bands). The seeing remained below $1''$ during the observations. We observed the northern field for a total of 18000 seconds, or 5 hours, and the southern field for half that time. To be certain that no significant mask/sky alignment drifts occurred during the overall integrations, we observed neither field for more than 2700 seconds in a single exposure. We observed HeNeAr comparison arc lamps through each mask for wavelength calibration.

We reduce the data with the Carnegie Observatories System for MultiObject Spectroscopy (COSMOS; A. Oemler et al.) package and extract individual 2D rectified, wavelength-calibrated and sky-subtracted spectra in the wavelength range $5600 - 9000 \text{ \AA}$. Using standard IRAF routines¹, we median combine the individual sky-subtracted spectra corresponding to each knot, rejecting pixel values $> 3\sigma$ from the median of the pixel stack to eliminate cosmic rays.

4.4 Analysis, Results & Discussion

4.4.1 $H\alpha$ detections

We begin our spectral analysis by visually inspecting all of the sky-subtracted and combined spectra to search for detectable $H\alpha$ flux from the targeted UV-bright knots. For any cases with visually-detected $H\alpha$ emission, we average the rows showing signal and measure the radial velocity centroid from this final 1D spectrum. The procedure is designed such that we may exclude any rows that have minor overlaps with neighboring spectra or contain any remaining artifacts.

We estimate the line centroid measurement errors to be $\sim 8 \text{ km s}^{-1}$ from fits to the bright OH 6498.72 \AA sky line from numerous (pre sky-subtracted) spec-

¹IRAF is distributed by the National Optical Astronomy Observatories, which are operated by the Association of Universities for Research in Astronomy, Inc., under cooperative agreement with the National Science Foundation.

tra. This measurement error is a lower limit to the $H\alpha$ line measurement error because the sky line is typically brighter and cleaner than the $H\alpha$ detections in our sample. We apply a constant -28.4 km s^{-1} heliocentric velocity correction to the radial velocities of the $H\alpha$ knots; the difference in the heliocentric correction between consecutive nights is $\sim 0.1 \text{ km s}^{-1}$, or $\sim 1\%$ of the typical line centroid measurement error.

Of the 313 slits on the two IMACS masks, $\sim 25\%$ returned unusable spectra due to overlapping spectra or other artifacts in the data. We therefore only search for $H\alpha$ emission in the remaining 235 spectra. Fifteen of these spectra (or $\sim 6\%$) yield detectable $H\alpha$ emission. Figure 4.1 presents a few of our final 1D spectra illustrating the range of strength of the $H\alpha$ detections. Our 6% return is roughly what is expected given the difference in ages between the ‘blue’ GALEX-detected knots targeted here ($< 360 \text{ Myr}$) and $H\alpha$ knots ($\sim 10 \text{ Myr}$) – especially when considering that priority was given to the bluest and brightest GALEX knots (so most targeted GALEX knots are likely $< 200 \text{ Myr}$ old). We plot the locations of these fifteen knots in Figure 4.2 and list the relevant information in Table 4.1. The physical scale of the individual $H\alpha$ knots (calculated from the extent of $H\alpha$ emission along the slit) range from 25 to 92 pc, with a median value of 67 pc (adopting a distance of 8.6 Mpc to NGC 628, determined using the planetary nebula luminosity function; Herrmann et al. , 2008).

4.4.2 $H\alpha$ knot velocities in the disk frame and σ_z

Our present aim is to measure the vertical velocity dispersion of the knots in the outer disk of NGC 628 (σ_z , with z defined perpendicular to the disk plane). Given the low inclination of NGC 628 ($i \sim 6^\circ$; Kamphuis & Briggs , 1992), the observed line-of-sight velocities are almost entirely due to the actual vertical velocities. However, as Kamphuis & Briggs (1992) have shown, the outer gas disk

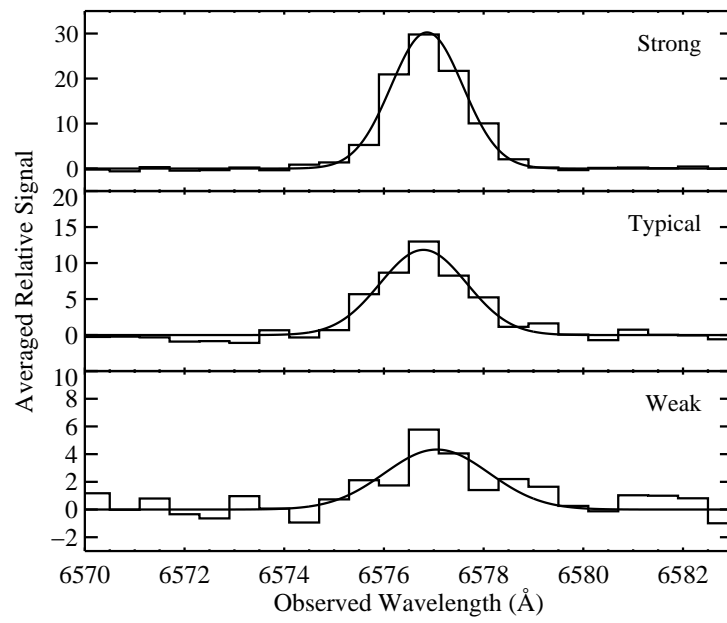


Figure 4.1 Three of our final 1D spectra, illustrating the range of strength of the $H\alpha$ detections. Note the different y -axis ranges. Qualitatively, our final sample is composed of two ‘Strong’, nine ‘Typical’, and four ‘Weak’ $H\alpha$ detections.

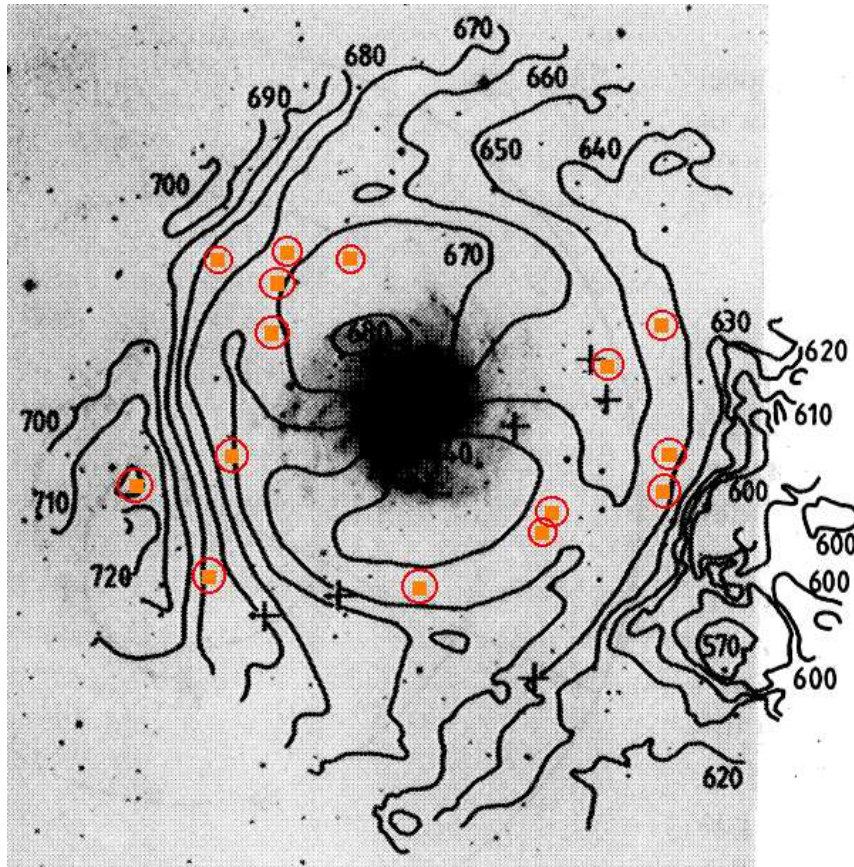


Figure 4.2 Figure 5 of Kamphuis & Briggs (1992) showing the velocity field of the H I-emitting gas disk surrounding NGC 628, with our 15 H α detections overplotted as encircled filled squares. The image is $\sim 30'$ on a side. The H α knots are found between ~ 1 and $1.8 R_{25}$ (13.5 - 23.2 kpc)

Table 4.1. $H\alpha$ detections

RA (J2000)	Dec (J2000)	R/R_{25}	v_{helio}	v_{TH}	Δv
01:36:04.47	+15:45:27.3	1.76	640	641	−1
01:36:05.40	+15:44:23.3	1.76	668	642	26
01:36:06.53	+15:49:37.0	1.72	652	647	5
01:36:14.07	+15:48:19.0	1.32	667	652	15
01:36:20.94	+15:43:33.5	1.17	644	643	1
01:36:22.12	+15:42:58.8	1.20	628	643	−15
01:36:38.71	+15:40:52.1	1.19	651	642	9
01:36:51.02	+15:52:03.6	1.06	680	684	−4
01:36:59.23	+15:52:13.6	1.29	657	670	−13
01:37:00.35	+15:51:19.1	1.20	659	675	−16
01:37:00.94	+15:49:49.7	1.04	658	674	−16
01:37:05.30	+15:44:45.3	1.18	639	649	−10
01:37:09.28	+15:41:14.0	1.70	704	679	25
01:37:10.06	+15:52:08.9	1.64	664	677	−13
01:37:17.86	+15:43:51.0	1.79	656	711	−55

*all velocities in km s^{-1} . v_{helio} refers to the heliocentric velocities of the $H\alpha$ knots, while v_{TH} refers to THINGS heliocentric H I-emitting gas velocities measured by Walter et al. (2008). $\Delta v = v_{helio} - v_{TH}$

of NGC 628 is chaotic and non-uniformly rotating. Whether this is also true for the outer stellar disk is unknown, and therefore whether we should use the previous orientation parameters obtained for the inner disk or some other ones is unclear. We therefore present results using various models for the disk orientation and kinematics, and accept the model with the lowest resulting velocity dispersion as the one most likely to be correct. Results of the following analysis will be discussed further in §4.

We use a maximum likelihood approach to estimate the Gaussian parameters best describing the *unbinned* relative velocity (Δv) distributions. Specifically, we search a grid of mean and dispersion values (from -50 to 50 km s^{-1} and 1 to 100 km s^{-1} , respectively) for the combination that yields the highest total probability (likelihood) of the Gaussian function, using the unbinned Δv values as the independent variable. Our velocity dispersion estimates will provide only a single value for the radial range spanned by the knots ($\sim 1 - 1.8R_{25}$). We have insufficient detections to measure the velocity dispersion as a function of radius. The following analysis will therefore consider the outer disk as a constant velocity dispersion, fixed-height component, and the values derived only represent the disk between $\sim 1 - 1.8R_{25}$. In support of this approach, note that the simulations of Kazantzidis et al. (2009) predict a roughly constant velocity dispersion in the outer disk.

We examine four models for the outer disk orientation and kinematics. First, we test a purely face-on disk by assuming a constant 656 km s^{-1} systemic velocity. This ‘model’ yields a velocity dispersion of $18 \pm 5 \text{ km s}^{-1}$. Second, we adopt the parameters of the inner neutral hydrogen gas disk of Kamphuis & Briggs (1992) (inclination $i = 6.5^\circ$, major axis position angle $PA = 25^\circ$ and a mean velocity of 656 km s^{-1}) and a rotation velocity of 170 km s^{-1} (Fathi et al. , 2007) and

find a velocity dispersion of $19 \pm 5 \text{ km s}^{-1}$. Third, we adopt the two-component model of Kamphuis & Briggs (1992) ($i = 13.5^\circ$ and $PA = 75^\circ$ beyond $1.2R_{25}$, using the same inner disk values as the previous case for the knots found at $R < 1.2R_{25}$) and find a velocity dispersion of $31 \pm 10 \text{ km s}^{-1}$. Finally, we adopt the neutral gas velocities from The H I Nearby Galaxy Survey (THINGS; Walter et al. , 2008) at the position of each knot and find a velocity dispersion of $19 \pm 6 \text{ km s}^{-1}$. Figure 4.2 shows the spatial distribution of the knots around the gas disk of NGC 628, and THINGS gas velocities at the positions of each knot are listed in Table 4.1. This ‘model’ tests for the possibility that the knots have low velocity dispersion around a complex velocity field defined by the H I-emitting gas. Given the result that the velocity dispersion is similar to the simple disk models, we conclude that there is no evidence for highly complex kinematics.

The velocity dispersion estimates generally cluster around 20 km s^{-1} and agree to within 1σ (although the one estimate at $31 \pm 10 \text{ km s}^{-1}$ is just consistent with the others). The general agreement, independent of the model used, suggests that the dominant source of uncertainty is currently the statistical one associated with the limited sample size. Because the fourth ‘model’ is taken directly from the H I data and produces a velocity dispersion as tight as do the other models, we adopt this model for the remainder of the paper.

Figure 4.3 shows the distribution of velocities relative to the Walter et al. (2008) gas disk values (the fourth model), binned by 15 km s^{-1} . We removed a slight, but significant, mean velocity offset (17 km s^{-1}) when evaluating the velocity dispersion; Table 4.1 and Figure 4.3 include this correction. We attribute this shift to a velocity zero point difference in the various datasets although we were unable to directly identify the cause (Figure 4.2 shows that the $H\alpha$ knots are well-distributed across the face of the disk; we therefore do not expect that the

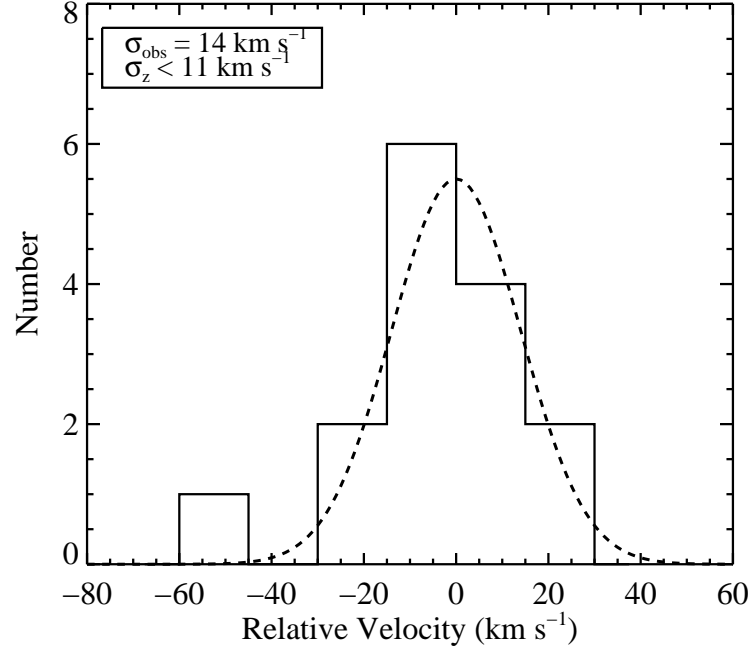


Figure 4.3 Distribution of H α knot vertical velocities, relative to THINGS (Walter et al. , 2008) neutral gas measurements. The outlier is the source detected on the high velocity cloud; we ignore this source in the analysis because its relation to the gas disk is uncertain.

offset is due to an undersampling of the relative velocity distribution). When we exclude the knot at 01:37:17.86, +15:43:51.0 with $\Delta v = v_{helio} - v_{TH} = -55 \text{ km s}^{-1}$, which lies on the high velocity cloud (HVC) described in Kamphuis & Briggs (1992), we arrive at our best (lowest and most likely) estimate of the observed H α knot velocity dispersion, $14 \pm 4 \text{ km s}^{-1}$. Excluding the same knot from the other models does not significantly change their values. The Gaussian representing this final *unbinned* Δv distribution is overplotted in Figure 4.3 (for presentation, the height of the Gaussian is determined by a fit to the binned Δv distribution; the dispersion is the only value used in our analysis, however).

We now consider the degree to which our observational errors inflate the velocity dispersion measurement ($\sigma_{obs} = 14 \text{ km s}^{-1}$). Subtracting our previous velocity error estimate (8 km s^{-1}) in quadrature from the measured velocity dispersion, we estimate that $\sigma_z < 11 \text{ km s}^{-1}$. We emphasize that σ_z is likely to be an upper limit to the vertical velocity dispersion because 1) the measurement uncertainty is larger than 8 km s^{-1} , 2) the uncertainty in the reference H I-emitting gas velocities was ignored, and 3) we may have missed the correct model for the underlying disk kinematics.

Our low velocity dispersion measurement suggests a relatively undisturbed stellar disk, which at first seems to contrast with the Kamphuis & Briggs (1992) observation of a chaotic outer gas disk. The Kamphuis & Briggs (1992) observation was strongly influenced by the HVCs and kinematic features at the largest radii, however—the bulk of the gas disk is in fact rather undisturbed (see Figure 4.2). Nevertheless, a difference between a relatively undisturbed stellar disk and a disturbed gas disk might be expected, considering the results of Thilker et al. (2007) and Moffett et al. (2009), who find that Type 1 XUV disks (of which NGC 628 is a member) cover a wide range of galaxy masses, colors and morphologies, and that these disks may in fact be associated with minor interactions or accretion. The disturbed structure observed in the gas may result from an interaction event (Kamphuis & Briggs, 1992) to which the stellar disk was less sensitive. Such an event may have then triggered the Type 1 XUV disk that is observed today.

4.4.3 Outer disk scale height h_z

Assuming that the $\text{H}\alpha$ knot density has the same vertical distribution as the underlying mass density distribution of the disk, for an adopted scaleheight h_z we constrain the surface mass density of the outer disk Σ using our measurement of

σ_z . We will return to discuss the validity of this assumption, although we do not have any alternative given our current data. The relevant equation (van der Kruit , 1988) is

$$\sigma_z^2 = KG\Sigma h_z, \quad (4.1)$$

where $K = 1.7051\pi$ for an ‘intermediate’ vertical mass density distribution (between the isothermal $\text{sech}^2(z)$ and exponential distributions) and G is the gravitational constant. The relation was constructed by solving the Boltzmann and Poisson equations for plane parallel layers. For a galaxy with a flat rotation curve, the plane parallel case provides a realistic model from which to estimate the surface mass density (van der Kruit , 1988). Because Christlein & Zaritsky (2008) found mostly flat rotation curves in a sample of 17 nearby outer disks, we expect the plane parallel framework to remain valid in the outer regions (we further assume a constant scale height over the radial range of the knots). Corrections to the relation from a dark halo term are negligibly small at low z (van der Kruit , 1988); however, in the outer disk the baryonic disk contribution to the mass budget presumably drops more rapidly with radius than does the dark matter contribution, and so the dark matter may in fact not be negligible in the outer disk. In the following section we show that the van der Kruit (1988) relation is indeed appropriate at these radii (we find that no dark matter in the disk is required to explain existing observations, even when assuming a rather large value for h_z).

Because NGC 628 is nearly face-on, we must estimate the scale height h_z of the tracer particles (the knots) indirectly. Herrmann et al. (2009) argue, based on stability arguments and the observed velocity dispersion of PNe, that the scale-height near the edge of the region they probe (~ 11 kpc) must be > 400 pc. The

vertical disk flaring suggested by the PNe analysis resembles the known flaring of gas disks in their outer regions, with neutral hydrogen gas scale heights near ~ 700 pc at the R/R_{25} distances considered here (Merrifield , 1992; Corbelli & Salpeter , 1993; Olling , 1996). Because the $H\alpha$ knots are young and because they lie at radii larger than those probed by the PNe, we adopt a scale height for the knots in line with that of the flaring gas, $h_z = 700$ pc at $1.3R_{25}$, the median radius of our $H\alpha$ detections. Recall however that we treat the outer disk as a fixed-height component. In reality, h_z may range between ~ 400 pc and ~ 1000 pc over the radii covered by our detections. Assuming a constant 700 pc over the entire outer disk therefore implies a large uncertainty in the final outer disk mass, which we assume to be $\sim 20\%$. This level of uncertainty will not significantly affect our conclusions, however. Finally, we note that our assumption that the $H\alpha$ knots trace the same mass distribution as the outer disk gas is different from what one would expect in the inner disk. In the inner disk, molecular clouds (and their $H\alpha$ knots) have a smaller vertical scaleheight than the mass, which is dominated by the stellar component. In the outer disk, however, where the dominant baryonic component is the gas (as we show below), our assumption is much more appropriate. Whether the $H\alpha$ knots trace the neutral gas is more uncertain, although where examined in detail the correspondence appears good (Thilker et al. , 2005; Herbert-Fort et al. , 2009). In view of this, a large scaleheight for the outer stellar disk should be expected. We caution however that if a significant amount of mass extends to heights larger than the 700 pc scaleheight assumed for the knots, we are not sensitive to it with the $H\alpha$ knot measurement.

4.4.4 Outer disk mass density

We now estimate the mass density of the outer disk in order to determine the relative contributions of stars and gas to the total outer disk mass. Using $\sigma_z = 11$

km s^{-1} and our adopted $h_z = 700 \text{ pc}$, we calculate that the outer disk surface mass density Σ is $7.5 M_\odot \text{ pc}^{-2}$. The total mass between $1 - 1.8R_{25}$ is then $\sim 8.4 \times 10^9 M_\odot$.

We now use results from deep optical imaging of the outer regions of NGC 628 ($\mu_V \sim 27 \text{ mag arcsec}^{-2}$ at $1.3 R_{25}$; Natali et al. , 1992) to estimate that the mass-to-light ratio Υ of the outer disk is ~ 18 . The outer disk mass is therefore not primarily in the form of normal stars. For comparison, Herrmann et al. (2009) found that the PNe velocity dispersions imply $\Upsilon = 1.4$ for the inner disk. Reconciling the outer and inner disk Υ values would require a factor of 10 changes in σ_z or Σ , neither of which is that poorly constrained. Therefore, as one might expect, we detect a significantly higher Υ in the outer regions. If we adopt $\Upsilon = 3$ as an upper limit for an old outer disk stellar population (Bell & de Jong , 2001), we find that the dark material in the outer disk must be at least five times more massive than the stellar component. In order to match the $\mu_V \sim 27 \text{ mag arcsec}^{-2}$ observation, an outer disk stellar population with $\Upsilon < 3$ would require $\Sigma_\star < 1.3 M_\odot \text{ pc}^{-2}$ and $M_\star < 1.4 \times 10^9 M_\odot$. This leaves $> 7 \times 10^9 M_\odot$ of dark material to be accounted for.

We now consider the neutral gas component of the outer disk and whether it can account for the optically non-luminous mass. Using the outer disk H I-emitting gas mass from Kamphuis & Briggs (1992) (over the relevant radial range), $\sim 6 \times 10^9 M_\odot$, we estimate the total outer disk baryonic mass (atomic gas + stars) to be between $\sim 6 \times 10^9 - 7.4 \times 10^9 M_\odot$. Comparing this total baryonic mass to the total mass required by the H α knot velocity dispersion ($\sim 8.4 \times 10^9 M_\odot$), we find that the baryonic matter (mainly the H I-emitting gas) can account for nearly all of the measured outer disk mass (note that we have ignored any molecular gas contribution). Our assumption that the dark matter contribution to

the disk is negligible at large radii appears justified, as does our claim that the gaseous component dominates the baryon budget.

4.4.5 Star formation history constraints

A separate intriguing question is whether star formation has occurred at the current rate for the entire lifetime of this galaxy. The result of such a stellar component could, in principle, violate the surface brightness or surface mass density measurements. Independent of the surface brightness measurement we can simply calculate whether the integrated star formation results in a mass density in conflict with the measurement. Using deep $H\alpha$ imaging of three nearby late-type spiral galaxies (one of which is the current focus; NGC 628, NGC 1058 and NGC 6946), Ferguson et al. (1998) found their outer disk star formation rate densities to be between $\sim 0.01 - 0.05 M_{\odot} \text{ pc}^{-2} \text{ Gyr}^{-1}$. For the following exercise, we adopt a SFR density of $0.03 M_{\odot} \text{ pc}^{-2} \text{ Gyr}^{-1}$ for the outer disk of NGC 628. For comparison to the Ferguson et al. (1998) SFR densities, Trujillo et al. (2009) used GALEX FUV imaging to measure the SFR density in the outer disk of M94 and found $\sim 0.4 M_{\odot} \text{ pc}^{-2} \text{ Gyr}^{-1}$. The star formation in the outer regions of M94 is unusually large however, producing an anti-truncated optical disk light profile (NGC 628 shows a standard exponential optical light profile to R_{25} , with only a very slight possible downbending in the profile to $\sim 1.3 R_{25}$, the extent of the deep optical observations; Natali et al. , 1992). For NGC 628, assuming uniformly-distributed constant star formation over a Hubble time leads to an expected stellar outer disk mass of $5 \times 10^8 M_{\odot}$ ($0.45 M_{\odot} \text{ pc}^{-2}$), well within our measured mass of $8.4 \times 10^9 M_{\odot}$ and within the stellar mass inferred from the measured surface brightness ($M_{\star} < 1.4 \times 10^9 M_{\odot}$ for a population with $\Upsilon < 3$). We conclude that the outer disk may have been forming stars for the entire lifetime of the galaxy at approximately the current star formation rate.

4.4.6 Similarities between the young and old components

We now compare the outer disk velocity dispersions of the young (< 10 Myr) and old (100 Myr – 10 Gyr) populations, traced by the $H\alpha$ knots and PNe (Herrmann et al. , 2009), respectively, and find little difference ($\sim 11 \text{ km s}^{-1}$ vs. $\sim 12 \text{ km s}^{-1}$; a small difference may be allowed if we treat the $H\alpha$ velocity dispersion as a true upper limit, however). Because the difference is unlikely to be much larger than the 1σ error of the measurement, we cannot say that there is a significant difference in the kinematic or structural properties between the young and old outer disk populations.

A powerful tracer of the evolution of stellar populations of different ages is the increase of velocity dispersion with age, or, alternatively, the varying asymmetric drift of various populations. The observed low σ_z of the $H\alpha$ knots immediately suggests that the degree of asymmetric drift will be small. If one considers that some fraction of the observed value must reflect the intrinsic dispersion of the gas, then the asymmetric drift will be even smaller. The other population that has been measured, PNe, also has a low velocity dispersion and the inferred asymmetric drift is also relatively small ($< 15 \text{ km s}^{-1}$; Herrmann et al. , 2009). With the current measurements we cannot conclude that there has been any increase in the velocity dispersions between the very young $H\alpha$ knots and the older PNe (we comment further on this issue in the following section). It is evident that such an investigation will require uncertainties in the velocity dispersions better than $\sim 1 \text{ km s}^{-1}$.

4.5 Summary and Conclusions

We have measured the kinematics of $H\alpha$ knots in the outer disk of NGC 628. We find the stellar disk (traced by the $H\alpha$ knots) to have a low velocity disper-

sion, suggesting an undisturbed extended stellar disk. NGC 628 differs from the better-known outer disks of M83 and M94, which were likely accentuated by recent disturbances from neighbors, but resembles (both in optical and kinematic profiles) the outer disks detected in other relatively undisturbed nearby edge-on disks by Christlein & Zaritsky (2008), supporting the idea that outer disk star formation can be a low-level and ongoing phenomenon in isolated galaxies.

We find σ_z of the $H\alpha$ knots to be $< 11 \text{ km s}^{-1}$ between $1 - 1.8R_{25}$ ($13.5 - 23.2$ kpc). We adopt a scaleheight similar to the known flaring gas profiles of outer disks ($h_z = 700 \text{ pc}$) and estimate a mass density $\Sigma = 7.5 \text{ M}_{\odot} \text{ pc}^{-2}$ that can be entirely explained by the observed gas and stars in the outer disk. If the $H\alpha$ -hosting disk is actually much thinner than the flaring gas disk, more dark matter in the outer regions would be allowed. Assuming that outer disk star formation has been going for a Hubble time does not violate either the surface brightness nor surface mass constraints. The high incidence of outer disks (c.f. Christlein & Zaritsky, 2008) suggests that the star formation is not a rare phenomenon – here we show that current limits cannot exclude long-lived outer disk star formation.

Finally, the velocity dispersion of PNe towards the outer disk of NGC 628 (Herrmann et al., 2009) is nearly the same as that of the $H\alpha$ knots (the discrepancy grows slightly when considering the dispersion of the $H\alpha$ knots as a strict upper limit, although any plausible difference remains small). This can result either if the PN population is rather young (so that scattering has not had a chance to enlarge the dispersion significantly), if there is very little scattering, or if scattering occurs primarily in a single (or few) discrete events that occurred prior to the creation of the bulk of the PNe. We do not expect the outer disk to be exclusive young (see above) and we do expect some level of scattering in outer disks (if not from the classical spiral arms and molecular clouds of inner disks, then

perhaps from satellites and dark halo substructure). The solution may be found in the Kazantzidis et al. (2009) simulations, which show that outer disk heating is dominated by the most massive infall event of halo substructure onto the disk, so that stellar populations of different ages do not necessarily have different velocity dispersions. A larger sample of outer disk kinematic measurements could be used to constrain the rate and impact of such infall events.

CHAPTER 5

A SEARCH FOR MOLECULAR EMISSION FROM OUTER DISK STAR-FORMING
COMPLEXES IN NGC 628

5.1 Chapter Introduction

Recent theoretical studies attempt to explain how star formation can be occurring in the low density environments of outer disks, which lie below the global Kennicutt threshold for star formation ($\Sigma_{gas} \sim 1 - 20 M_{\odot} \text{ pc}^{-2}$; Kennicutt, 1998). Based on simulations, it appears that while the bulk of outer disk gas does lie below the threshold, local overdensities can lead to a sprinkling of star formation in an otherwise unusual environment (Bush et al., 2008). Unfortunately, little is known about the relation between the molecular gas in these outer star forming complexes and their star formation rates.

While the star formation rate (SFR)-molecular gas relation in nearby galaxies has been examined on larger, galaxy-sized scales (e.g. Bussmann et al., 2008, and references therein), only recently has the shape of this relation been probed on smaller scales, < 1 kpc across (Kennicutt et al., 2007). While the small-scale SF law closely resembles the global law for galaxies, these 1 kpc scales nevertheless remain an order of magnitude or two larger than the apparent sizes of the most isolated, individual outer disk complexes, as seen in our deep, high-resolution optical imaging (Herbert-Fort et al., 2009).

More recently, Onodera et al. (2010) examined the Kennicutt-Schmidt law on giant molecular cloud (GMC) scales, ~ 80 pc across, using data from the 45-m single-dish Nobeyama Radio Observatory telescope, $\text{H}\alpha$ observations and Spitzer 24- μm data. Though these observations focus on the inner disk of M33, they produce results relevant for outer disk studies. Onodera et al. (2010) find

that while the surface density of gas and that of the SFR correlate well at ~ 1 kpc resolution, the correlation becomes looser with higher resolution and breaks down at GMC scales. The authors attribute a scatter of over four orders of magnitude in the SFR surface density (at ~ 80 pc resolution) to the variety of star-forming activity among GMCs, due to the various evolutionary stages of GMCs and to the drift of young clusters from their parent GMCs. The Kennicutt-Schmidt law appears to be accurate only when averaging over an area covering multiple clusters.

A search for outer disk molecular emission in NGC 4414 with the 30-m antenna on Pico Veleta (Spain) by Braine & Herpin (2004) reveals a clear decline in the CO(2-1)/CO(1-0) line ratio with radius (independent of beam size) which the authors interpret as a decrease in excitation temperature. Therefore even if substantial CO is present in an outer disk, the CO(2-1) line could be quite weak. Braine & Herpin (2004) describe the H I disk as a two-phase medium, with the warm diffuse phase dominating at large radii, in the outer disk. We should therefore not expect as much molecular cloud formation as exists in the inner disk, where more cool H₂ is available to form GMCs. The GMCs that do form in outer disks are also expected to be of lower mass than those in the inner disks, or generally $< 10^5 M_{\odot}$.

This chapter presents a small feasibility study aimed at detecting ¹²CO (J=2-1) molecular emission from massive star forming regions in the outer disk of the nearby galaxy NGC 628, using the sensitive Atacama Large Millimeter Array (ALMA) receiver on the Submillimeter Telescope (SMT). Though we do not expect clear detections, we will at worst be able to set limits for future ALMA efforts.

5.2 SMT Observations, Data Reduction & Analysis

We observed five UV-bright regions across the disk of NGC 628. These regions are shown in Figure 5.1; the 32.7'' SMT beam spans ~ 1.4 kpc (diameter) at the distance of 8.6 Mpc to NGC 628 (Herrmann et al. , 2008): region 1 is the nucleus of the galaxy and was observed on 1/27/09 and 1/29/09, for 10 minutes on-source each day, to check calibration fidelity; region 2 is at $\sim 0.6R_{25}$ and was observed for a total of 2.5 hours on-source on 1/27/09 and 2/4/09; region 4 (a 'region 3' was initially targeted but never observed) lies just beyond R_{25} along a UV-bright arm and was observed for 2.5 hours on-source on 2/3/09; region 5 is another UV-bright region near $\sim 1.2R_{25}$, observed for a total of 2 hours on-source on 1/28/09; region 6 is similar to region 5 but was observed for a total of 4.5 hours on-source on 1/29/09 and 2/2/09 (region 6 is our deepest observation; see below for more discussion of this region).

We used the dual-polarization ALMA 1.3mm JT SIS receiver and 1 GHz filterbanks for our observations with the SMT. We observed at $^{12}\text{CO}(2-1)$ 230.5 GHz in the upper sideband with a 5 GHz IF in 2-IF mode. The telescope operator provided the image rejection ratios in the vertical and horizontal polarizations when he tuned before observing each day. The rejections values are used to determine the reduced contribution from unwanted image signal of the desired frequency; the rejection values ranged between 10-12 dB and 15-17 dB in the horizontal and vertical polarizations, respectively, during the course of the observations. We observed Venus to point and focus, and obtained position-switch observations of Venus (1 min on source with 30 sec switches) to calculate the main beam efficiency and the ratio of signal in the vertical to horizontal polarizations, the latter to weight the two signals equally when combining them into the final spectra. During the course of our science observations, we position-switched to a clean

off-galaxy pointing, obtaining 5 minute scans with 1 calibration per scan, 20 sec between on- and off-source pointings. We used standard CLASS routines to reduce and combine the data.

Our observations of region 1 (the nucleus) from 1/27/09 provided a detection of Gaussian width 13 km s^{-1} and height 0.117 K on a baseline σ_{rms} of 0.008 K , while our observations from 1/29/09 provided a detection of Gaussian width 14 km s^{-1} and height 0.124 K , also on a baseline σ_{rms} of 0.008 K . The main beam efficiency (used when calculating the integrated H_2 mass) calculated for the region 1 observations was 0.86 . We measured a marginal $\sim 1\sigma$ detection from region 2 (near $0.6R_{25}$), with a Gaussian width of 21 km s^{-1} and height 0.005 K on a baseline σ_{rms} of 0.003 K . The main beam efficiency used for the region 2 calculations was 0.78 . Regions 4, 5, and 6 yielded no detections, though we attained baseline σ_{rms} depths of 0.003 K , 0.004 K and 0.002 K , respectively. For the calculation of total H_2 masses in the following section, we will estimate 2σ upper limits for imaginary 15 km s^{-1} -wide lines from these regions. The main beam efficiencies calculated for use in regions 4, 5 and 6 are 0.70 , 0.71 and 0.78 , respectively.

5.3 Results & Discussion

Our goal is to quantify the integrated H_2 masses of these star-forming knots, given our CO(2-1) observations. Starting with either an integrated line intensity measurement from a CO detection or with the final baseline σ_{rms} of a non-detection, we follow Mangum et al. (2008), Lavezzi et al. (1999) and Solomon et al. (1987) to calculate the integrated H_2 mass inside the beam, or an upper limit if no detection is available. Using the values provided in the previous section, we find the two observations of region 1 to provide final H_2 masses of $79 \times 10^6 M_\odot$ on 1/27/09 and $104 \times 10^6 M_\odot$ on 1/29/09. A crude estimate of the error on

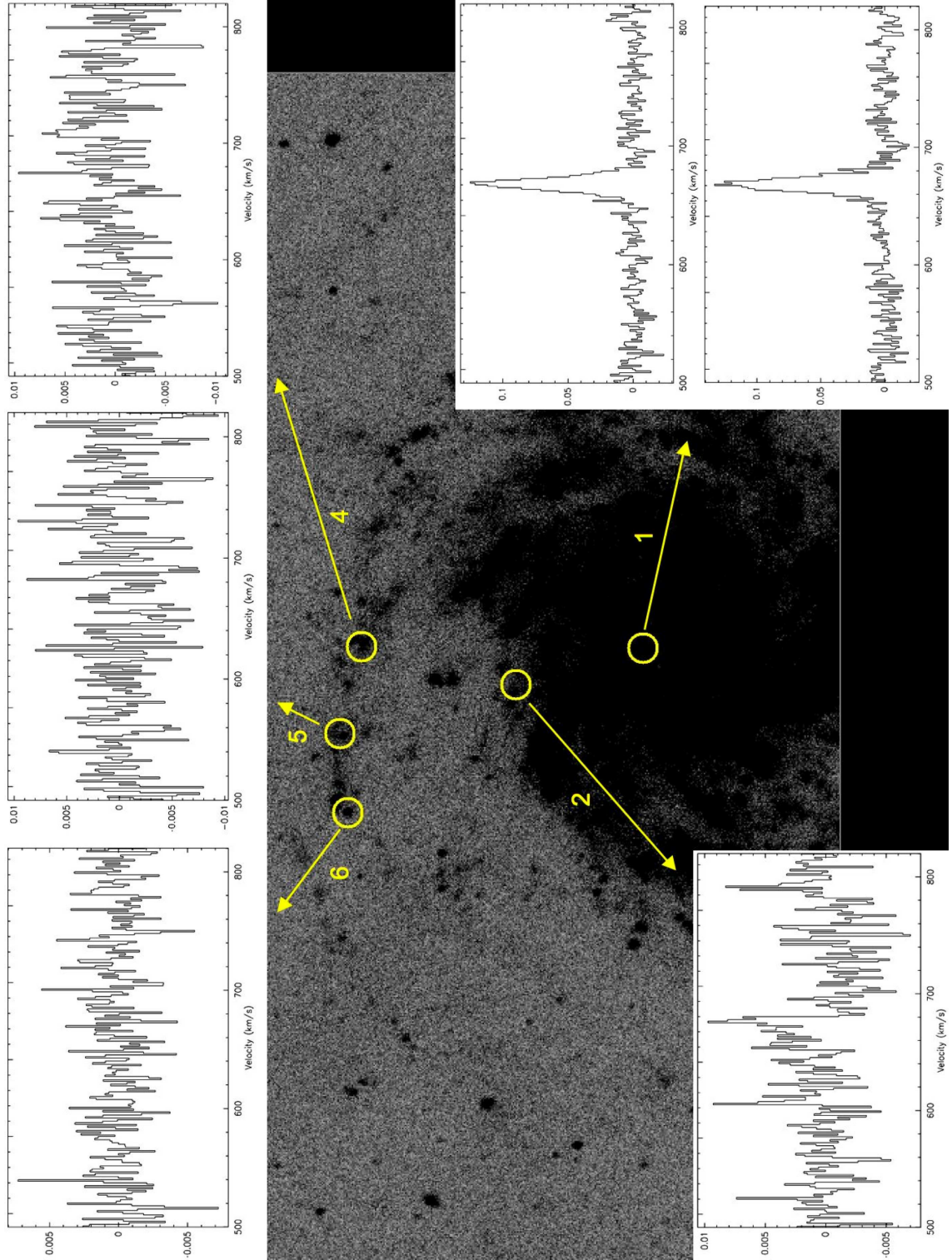


Figure 5.1 GALEX near-UV background image with our SMT pointings circled (showing the main beam FWHM of $32.7''$, or ~ 1.4 kpc). The final spectra from each region are shown in insets. There were no detections in the outer disk.

our final H_2 measurements is therefore between 10 – 20%. Region 2 provided a marginal $\sim 1\sigma$ detection of $6 \times 10^6 M_\odot$, though this should best be viewed as an upper limit given the poor Gaussian fit to the very weak emission. No detections were measured from regions 4, 5 or 6; however, 2σ upper limits on the mass of any possible H_2 in those regions (from imaginary emission lines, described at the end of the previous section) are 6×10^6 , 8×10^6 and $4 \times 10^6 M_\odot$, within the 1.4 kpc-wide beams.

Massive giant molecular clouds (GMCs) typically have H_2 masses of order $10^5 M_\odot$, and so our observations indicate that the outer disk regions contain less than about 60 GMCs each (< 40 in region 6). For comparison, there exist ~ 12 GMCs within 1 kpc of the Sun, with sizes up to tens of parsecs in diameter and with a mean intercloud separation of ~ 500 pc (Elmegreen, 1981). Assuming that the density of GMCs in the outer disk of NGC 628 matches that in the solar neighborhood of the Galaxy (as a very conservative estimate; the density should be lower in the outer disk), and accounting for our 1.4 kpc-wide beam (0.7 kpc radius), we might then expect to find up to $12 \times (0.7/1.0)^2 \sim 6$ GMCs in an outer disk pointing (we will focus on region 6), or $6 \times 10^5 M_\odot$ of H_2 , far below our upper limit of $4 \times 10^6 M_\odot$ (or ~ 40 GMCs). We use the ratio of the areas in the calculation because we are looking at a projected volume in the outer disk of NGC 628. Furthermore, a close look at the GALEX FUV image of region 6 shows that the emission there is highly concentrated at the center of the SMT beam, with the majority of FUV emission coming from a knot just 0.4 kpc wide. We do not know how the molecular gas is distributed around the FUV emission, but if we assume that it is all contained within the knot, we can expect less than half the mass of a typical GMC at this pointing, or $< 5 \times 10^4 M_\odot$ of H_2 . Note that while we are using the solar neighborhood GMC distribution, we recognize that

a ‘full’ GMC is not required for star formation to occur; smaller clouds can also produce massive stars. For our purposes however the solar neighborhood GMC distribution provides a reasonable benchmark. Using the solar neighborhood GMC distribution as a standard, it is therefore not surprising that we failed to detect molecular emission from the outer disk knots. Furthermore, Digel et al. (1994) studied molecular clouds beyond the optical radius of the Milky Way and found them to be in the range of $2 - 40 \times 10^3 M_\odot$; such clouds are far below our detection limit in the outer disk of NGC 628.

Of course, we are preferentially selecting star-forming regions where the GMC density may be much higher than it is in the solar neighborhood. Using our H_2 mass upper limit from region 6, we can constrain the maximum GMC density of this region compared to the solar neighborhood value of 12 kpc^{-2} . We find that a GMC density of up to $(40/0.7^2)/(12/1.0^2) \sim 7\times$ that in the solar neighborhood is allowed by the data. If we now assume the GMC density of star-forming regions in the outer disk is 84 kpc^{-2} rather than 12 kpc^{-2} ($7\times$ higher), and assume that all H_2 emission is coming from the smaller 0.4 kpc -wide region surrounding the concentrated FUV emission, we should expect $< 3.5 \times 10^5 M_\odot$ of H_2 at this pointing. This amount of H_2 is still below our detection limit.

Another way to estimate the expected H_2 mass at our outer disk pointings is to measure the far-UV (FUV) emission observed by GALEX within a 1.4 kpc -wide aperture, use the Kennicutt (1998) relation to estimate a star formation rate (SFR) and finally use the Kennicutt et al. (2007) relation between SFR and H_2 gas surface density to estimate a total H_2 mass within our SMT beam. A useful form of the Kennicutt (1998) relation, using an internal extinction-corrected FUV AB magnitude, is found in Trujillo et al. (2009): $\log(\text{SFR})(M_\odot \text{ yr}^{-1}) = 2\log d(\text{pc}) - 0.4\text{FUV} - 9.216$, where d is the distance to the region ($8.6 \times 10^6 \text{ pc}$ here). We mea-

sure the FUV AB magnitude within a 1.4 kpc-wide aperture centered on position 6 (01:36:54.9, +15:52:57.9; our lowest H₂ mass upper limit) to be 19.51 AB mag. Using the internal extinction slope (along galactic radius) and normalization for NGC 628 from Muñoz-Mateos et al. (2007), -0.064 AB mag and 1.704 AB mag, respectively, evaluated at $1.2R_{25}$ (16.2 kpc) and corrected by the relative areas of our SMT beam to the $6''$ circular (galactocentric) annuli used by Muñoz-Mateos et al. (2007) (evaluated at $1.2R_{25}$), we find an internal extinction correction of 0.04 AB mag within the small SMT beam area. Finally, we use the relation between SFR surface density and H₂ surface mass density on small (~ 1 kpc) scales from Kennicutt et al. (2007), $\log \Sigma_{SFR}(M_{\odot} \text{ yr}^{-1} \text{ kpc}^{-2}) = 1.37 \log \Sigma_{H_2}(M_{\odot} \text{ pc}^{-2}) - 3.78$, and estimate the final H₂ mass within the SMT beam to be $\sim 3 \times 10^6 M_{\odot}$. This value is just below our estimated upper limit for region 6, $4 \times 10^6 M_{\odot}$, so again, it is not surprising that we were unable to detect molecular emission from this outer disk knot – though this estimate does suggest that integrating a bit longer might have provided a marginal detection.

The other outer disk regions have integrated FUV fluxes below that of region 6 (region 2 near $0.6R_{25}$ has about the same FUV flux). Because region 6 is our deepest pointing, if we did not detect H₂ there we should not expect to have detected it in either of the other outer disk regions. As for region 2, recall that we found a very marginal 1σ detection of $6 \times 10^6 M_{\odot}$ there. From the integrated FUV flux at region 2 we should expect $\sim 3 \times 10^6 M_{\odot}$, which, given the marginal nature of the detection, seems about right. The explanation for why we did not detect anything in region 6, even though we integrated longer and the expected H₂ mass (estimated from the FUV flux) is about the same as in region 2, may be found in Braine et al. (2007). These authors searched for molecular emission at both ¹²CO(1-0) and ¹²CO(2-1) near large H II regions in the inner and outer disk

of NGC 6946 using the IRAM 30 m telescope. Although we find a few of the Braine et al. (2007) detections unconvincing, these authors claim evidence for an abrupt decrease in the molecular fraction at the edge of the optical disk, similar to that seen previously in the azimuthally-averaged star formation rate. If this is true and is also the case in NGC 628, it may explain our lack of detection in the outer disk. We caution however that this argument is based on disk-averaged quantities; it is likely that the molecular fraction does not drop as rapidly in the star-forming regions we observed.

The lack of a detection in the outer disk regions, given the significant investment of time, suggests that the clouds are likely to be more compact than in the inner disk, assuming some mean density of molecular gas is necessary for star formation. Typical cloud complexes analyzed in the inner disk of M51 by Kennicutt et al. (2007) have total hydrogen surface densities of $10 - 1000 M_{\odot} \text{ pc}^{-2}$. If we assume that the H_2 column density is 10% of the H I (Braine & Herpin, 2004), using our H_2 mass upper limit from region 6, $4 \times 10^6 M_{\odot}$, we estimate that the total hydrogen surface density in region 6 is $< 30 M_{\odot} \text{ pc}^{-2}$. This is at the low end of the range found in the inner disk of M51. It appears that outer disk molecular clouds may be both smaller and more widely separated than their inner disk counterparts.

Rather than assuming a $\text{H}_2 / \text{H I}$ ratio, we can calculate the H I mass of region 6 directly from the THINGS (Walter et al., 2008) moment 0 map of NGC 628. We find region 6 (within the 1.4 kpc-wide beam) to contain $\sim 3 \times 10^9 M_{\odot}$ of H I, implying a $\text{H}_2 / \text{H I}$ ratio of $< 10^{-3}$ (i.e. $< 0.1\%$). If we assume a ratio of 1:10 as suggested by Braine & Herpin (2004) and apply that to our calculated H I mass, we should then expect to find $\sim 3 \times 10^8 M_{\odot}$ of H_2 in region 6. Clearly, there exists less H_2 in this distant region than a typical inner disk $\text{H}_2 / \text{H I}$ ratio

would suggest. If we instead use the outer disk ratio calculated from Braine et al. (2007), ~ 0.01 , we should expect to find $\sim 3 \times 10^7 M_{\odot}$ of H_2 in region 6.

Unfortunately there exist a number of explanations for why we did not detect molecular emission from region 6. Perhaps the outer disk H_2 / H I ratio is even lower in NGC 628 than in NGC 6946 (Braine et al. , 2007). Maybe the CO(2-1) line is extremely weak, as Braine & Herpin (2004) suggest, even though there exists substantial CO at this position. Or, perhaps the molecular gas has been mostly consumed (or destroyed) by the recent, intense star formation. Without accompanying CO(1-0) observations it difficult to distinguish between these possibilities.

Therefore, while our $^{12}\text{CO}(2-1)$ observations did not yield detections of molecular emission in the outer disk of NGC 628 – though they might with additional time – they still make the case for followup observations with an interferometer (our original goal), where we could exploit the smaller beam sizes to further constrain Σ_{H_2} of the knots and probe the SFR-molecular gas relation on GMC-size scales and test the Onodera et al. (2010) results. Unfortunately, estimates of the required exposure time with CARMA, the interferometer most likely to be used for this science, show that attaining the depths presented here at higher spatial resolutions would currently require unreasonable amounts of time requested (more than a week of dedicated time, per pointing). We have therefore put the search for molecular emission from outer disk star-forming complexes on hold, to await the technological advances of the ALMA era.

5.4 Conclusions

In summary, we find no outer disk detections of molecular emission in NGC 628, though this is consistent with estimates based on a range of models. A factor of two deeper observations (relative to that of region 6, our deepest pointing) could

begin to detect emission from some objects. Finally, when using existing H I measurements we find that the H_2 / H I ratio is $\sim 100\times$ lower in the outer disk than in the inner disk. Additionally, we are unable to rule out the inner disk H_2 star formation law as remaining valid in nearby outer disks.

CHAPTER 6

CONCLUSIONS AND WAYS FORWARD

This dissertation describes a range of observational projects that help characterize the outer disks of nearby galaxies. We have used broadband optical observations from the LBT to examine outer disk cluster populations, and spectroscopic observations from Magellan to trace the kinematics of outer disk $H\alpha$ knots. We have also searched for molecular emission from outer disk star-forming complexes with the sensitive ALMA receiver on the SMT.

Our observations show that outer disks are populated by star clusters born in groups that remain clustered for a Gyr or more, out to distances of $2R_{25}$, in a kinematically cold component (in non-interacting galaxies). The individual clusters evaporate over a Gyr or more to create a uniform, low-surface brightness stellar component. The clusters we observe in outer disks have masses $\sim 10^2 - 10^4 M_\odot$, smaller than their inner disk counterparts by 1 – 2 orders of magnitude. They appear to form in very localized overdensities in the outer disk gas and are correlated with the spiral structure of the gas to large radii. The H_2 / H I ratio is $\sim 100\times$ lower in the outer disk than in the inner disk, which likely explains the trend towards smaller clusters at larger radii. Molecular emission from outer disk clusters is extremely faint and test the limits of current sensitivity. We expect that ALMA will begin to observe the outer disk molecular cores from which the clusters are born. Our observations provide a crude outer disk cluster formation rate of one cluster every ~ 2.5 Myr, or $\sim 0.004 M_\odot \text{ pc}^{-2} \text{ Gyr}^{-1}$. Outer disk star formation for a Hubble time is not excluded by our observations. Both blue and red groups of clusters reside in nearby outer disks, suggesting that many are born in situ and spend their lives in the outer disk. Our statistical analysis of the cluster-

ing of knots in outer disks shows that even galaxies without an obvious outer disk component in typical galaxy images may still host cluster populations at large radii. We also find evidence that some clusters may reside outside of their host gas disks. These objects are particularly interesting for follow-up study, as they either formed in the disk and were later transported beyond the edge somehow, or the gas distribution at the edge has changed dramatically in a short amount of time. Either case would be interesting to examine and could shed light on galaxy growth and long-term evolution.

The future of the field looks bright. Although this component went overlooked for so long, star-forming outer disks appear to be common and long-lasting features of most nearby galaxies. Possible ways forward come in a variety of projects. We could compile deeper catalogs of GALEX knots for a more reliable self-clustering analysis of the UV component of outer disks. We should also examine the GALEX knot - LBT knot cross-correlation, as well as the the GALEX knot - H I cross-correlation, as both of these could yield valuable clues about the spatial and temporal evolution of outer disk cluster groups. In terms of followup imaging, we could obtain longer wavelength baselines to push out the age limit of our samples, as well as deeper images to help us find more knots, in order to create more detailed and accurate background-subtracted Hess diagrams and correlation plots. These plots would help us trace the evolution of the cluster groups in a way that would compliment the improved correlation analyses. Such observations would also help lower the uncertainties in the cluster masses and ages determined from our Starburst99 modeling. In terms of followup spectroscopy, it would be very useful to have a sample of outer disk kinematic measurements similar to those presented here, but from both H α knots and planetary nebulae. A sizable sample (~ 50 disks) could be used to constrain the rate and impact of

halo substructure infall events on outer disks and shed light on a critical mechanism that may regulate outer disk growth. These are only a handful of projects (related to this thesis) that could push the study of outer disks forward. Projects like these, and many others, should keep astronomers busy for years to come.

REFERENCES

- Adelman-McCarthy, J. et al. 2007, *ApJS*, 172, 634
- Alberts, S. et al. 2011, arXiv, 1102.2893A
- Bailin, J., Power, C., Norberg, P., Zaritsky, D., Gibson, B.K. 2008, *MNRAS*, 390, 1133
- Bakos, J., Trujillo, I., Pohlen, M. 2008, *ApJL*, 683,103
- Begeman, K.G. 1987, Kapteyn Institute, PhDT, 199
- Bell, E.F. & de Jong, R.S. 2001, *ApJ*, 550, 212
- Bertin, E., 2006, in *Astronomical Data Analysis Software and Systems XV*, ASP Conf. Series 351, 112
- Bertin, E., & Arnouts, S. 1996, *A&AS*, 117, 393
- Bessell, M.S., Freeman, K.C., Wood, P.R. 1986, *ApJ*, 310, 710
- Bland-Hawthorn, J., Vlajić, M., Freeman, K.C., Draine, B.T. 2005, *ApJ*, 629, 239
- Blanton, M.R. et al. 2003, *ApJ*, 592, 819
- Braine, J. & Herpin, F. 2004, *Nature*, 432, 369
- Braine, J., Ferguson, A.M.N., Bertoldi, F., Wilson, C.D, 2007, *ApJL*, 669, 73
- Bush, S.J., Cox, T.J., Hernquist, L., Thilker, D., Younger, J.D. 2008, *ApJL*, 683, 13
- Bussmann, R.S. et al. 2008, *ApJ*, 681, 73L
- Buta, R. 1988, *ApJS*, 66, 233

- Cerviño, M., & Luridiana, V. 2004, *A&A*, 413, 145
- Chandar, Rupali; Fall, S. Michael; Whitmore, Bradley C. 2006, *ApJL*, 650, 111
- Christlein, D., Zaritsky, D. 2008, *ApJ*, 680, 1053
- Corbelli, E., Salpeter, E.E. 1993, *ApJ*, 419, 104
- Daigle, O., Carignan, C., Amram, P., Hernandez, O., Chemin, L., Balkowski, C., Kennicutt, R. 2006, *MNRAS*, 367, 469
- Dalcanton, J.J. et al. 2009, *ApJS*, 183, 67
- Davidge, T.J., Puzia, T.H., McConnachie, A.W. 2011, *ApJL*, 728, 23
- de Jong, R.S. et al. 2007, *IAUS*, 241, 503
- de Jong, R.S. et al. 2007, *ApJL*, 667, 49
- de Vaucouleurs, G., de Vaucouleurs, A., & Corwin, H.G. 1976, *Second Reference Catalogue of Bright Galaxies* (Austin : Univ. of Texas Press)
- Digel, S., de Geus, E., Thaddeus, P. 1994, *ApJ*, 422, 92
- Dressler, A., Hare, T., Bigelow, B.C., Osip, D.J. 2006, *SPIE*, 6269, 13
- Elmegreen, B. G. 1981, *ApJ*, 243, 512
- Fagiolini, M., Raimondo, G., Degl'Innocenti, S. 2007, *A&A*, 462, 107
- Fathi, K., Beckman, J.E., Zurita, A., Relaño, M., Knapen, J. H., Daigle, O., Hernandez, O., Carignan, C. 2007, *A&A*, 466, 905
- Ferguson, A.M.N., Wyse, R.F.G., Gallagher, J.S., Hunter, D.A. 1998, *ApJ*, 506, 19
- Fukugita, M., Shimasaku, K., Ichikawa, T. 1995, *PASP*, 107, 945

- Gehrels, N. 1986, *ApJ*, 303,336
- Giallongo, E., et al. 2008, *A&A*, 482, 349
- Gil de Paz, A. et al. 2005, *ApJL*, 627, 29
- Gil de Paz, A. et al. 2007, *ApJS*, 173, 185
- Godwin, J.G., Bucknell, M.J., Dixon, K.L., Green, M.R., Peach, J.V., Wallis, R.E.
1977, *Obs*, 97, 238
- Gogarten, S.M. et al. 2009, *ApJ*, 691, 115
- Graham, J.A. et al. 1997, *ApJ*, 477, 535
- Herbert-Fort, S. et al. 2009, *ApJ*, 700, 1977
- Herrmann, K.A., Ciardullo, R., Feldmeier, J.J., Vinciguerra, M. 2008, *ApJ*, 683, 630
- Herrmann, K.A., Ciardullo, R. 2009, *ApJ*, 705, 1686
- Hill, J. M., Green, R. F., & Slagle, J. H. 2006, *Proc. SPIE*, 6267, 62670Y
- Irwin, M.J., Ferguson, A.M.N., Ibata, R.A., Lewis, G.F., Tanvir, N.R. 2005, *ApJL*,
628, 105
- Jester, S. et al. 2005, *AJ*, 130, 873
- Kamphuis, J. & Briggs, F. 1992, *A&A*, 253, 335
- Karachentsev, I.D., Karachentseva, V.E., Huchtmeier, W.K., Makarov, D.I. 2004,
AJ, 127, 2031
- Karachentsev, I.D. 2005, *AJ*, 129, 178

- Kazantzidis, S., Zentner, A.R., Kravtsov, A.V., Bullock, J.S., Debattista, V.P. 2009, ApJ, 700, 1896
- Kennicutt, R.C. 1989, ApJ, 344, 685
- Kennicutt, R.C. 1998, ApJ, 498, 541
- Kennicutt, R.C. et al. 2007, ApJ, 671, 333
- Larson, R.B., Tinsley, B.M. 1978, ApJ, 219, 46
- Landolt, A. U. 1992, AJ, 104, 340
- Lavezzi, T.E., Dickey, J.M., Casoli, F., Kazès, I. 1999, AJ, 117, 1995
- Leitherer, C. et al. 1999, ApJS, 123, 3
- Leonard, D.C. et al. 2002, AJ, 124, 2490
- Makarova, L. 1999, A&AS, 139, 491
- Mangum, J.G., Darling, J., Menten, K.M., Henkel, C. 2008, ApJ, 673, 832
- Martin, C.L., Kennicutt, R.C., Jr. 2001, ApJ, 555, 301
- Martin, D.C. et al. 2005, ApJ, 619, 1L
- Merrifield, M.R. 1992, AJ, 103, 1552
- Moffett, A.J., Kannappan, S.J., Laine, S., Wei, L.H., Baker, A.J., Impey, C.D. 2009, arXiv0908.4232
- Monet, D.G. et al. 2003, AJ, 125, 984
- Moustakas, J. et al. 2009, in preparation

- Muñoz-Mateos, J.C., Gil de Paz, A., Boissier, S., Zamorano, J., Jarrett, T., Gallego, J., Madore, B.F. 2007, *ApJ*, 658, 1006
- Natali, G., Pedichini, F., Righini, M. 1992, *A&A*, 256, 79
- Nilson, P. "Uppsala general catalogue of galaxies" 1973, *ugcg.book*, N
- Olling, R.P. 1996, *AJ*, 112, 457
- Onodera, S. et al. 2010, *ApJL*, 722, 127
- Parker, R.J., Goodwin, S.P. 2007, *MNRAS*, 380, 1271
- Pflamm-Altenburg, J., Kroupa, P. 2008, *Nature*, 455, 641
- Pohlen, M., Dettmar, R.-J., Lütticke, R., Aronica, G. 2002, *A&A*, 392, 807
- Pompei, E., & Natali, G. 1997, *A&AS*, 124, 129
- Ragazzoni, R. et al. 2006, *Proc. SPIE*, 6267, 626710
- Rieke, G.H., Lebofsky, M.J. 1985, *ApJ*, 288, 618
- Roškar, R., Debattista, V.P., Stinson, G.S., Quinn, T.R., Kaufmann, T., Wadsley, J. 2008, *ApJL*, 675, 65
- Roškar, R., Debattista, V.P., Quinn, T.R., Stinson, G.S., Wadsley, J. 2008, *ApJL*, 684, 79
- Rownd, B.K., Dickey, J.M., Helou, G. 1994, *AJ*, 108, 1638
- Rubin, V.C., Peterson, C.J., Ford, W.K., Jr. 1975, *ApJ*, 199, 39
- Solomon, P.M., Rivolo, A.R., Barrett, J., Yahil, A. 1987, *ApJ*, 319, 730
- Swartz, D.A., Yukita, M., Tennant, A.F., Soria, R., Ghosh, K.K. 2006, *ApJ*, 647, 1030

- Swaters, R.A., van Albada, T.S., van der Hulst, J.M., Sancisi, R. 2002, *A&A*, 390, 829
- Thilker, D.A. et al. 2005, *ApJL*, 619, 79
- Thilker, D.A. et al. 2007, *ApJS*, 173, 538
- Tonry, J.L., Dressler, A., Blakeslee, J.P., Ajhar, E.A., Fletcher, A.B., Luppino, G.A., Metzger, M.R., Moore, C.B. 2001 *ApJ*, 546, 681
- Toomre, A. 1964, *ApJ*, 139, 1217
- Toth, G., Ostriker, J.P. 1992, *ApJ*, 389, 5
- Trujillo, I., Martinez-Valpuesta, I., Martínez-Delgado, D., Peñarrubia, J., Gabany, R.J., Pohlen, M. 2009, *ApJ*, 704, 618
- Tully, B. 1988, *Nearby Galaxies Catalog* (Cambridge: Cambridge University Press)
- van der Kruit, P.C., Allen, R.J. 1976, *ARA&A*, 14, 417
- van der Kruit, P.C. 1988, *A&A*, 192, 117
- Vazquez, G., & Leitherer, C. 2005, *ApJ*, 621, 695
- Walter, F., Brinks, E., de Blok, W.J.G., Bigiel, F., Kennicutt, R.C., Thornley, M.D., Leroy, A. 2008, *AJ*, 136, 2563
- Weiner, B.J., Williams, T.B., van Gorkom, J.H., Sellwood, J.A. 2001, *ApJ*, 546, 916
- Werk, J.K. et al. 2010, *AJ*, 139, 279
- Williams, B.F. et al. 2009, *AJ*, 137, 419

Wolfe, A. M., Gawiser, E., Prochaska, J. X. 2005, ARA&A, 43, 861

Wright, E.L. 2006, PASP, 118, 1711

Zaritsky, D., Christlein, D. 2007, AJ, 134, 135